

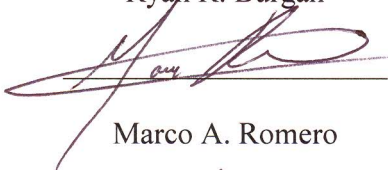
High Lift Micro Aerial Vehicle Design and Construction

A Major Qualifying Project Report
Submitted to the Faculty of the
WORCESTER POLYTECHNIC INSTITUTE
in Partial Fulfillment of the Requirements for the
Degree of Bachelor of Science
in Aerospace Engineering

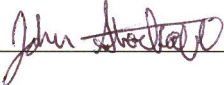
by

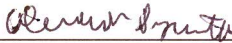


George C. Bucsan


Ryan R. Burgan

Marco A. Romero


John M. Stackable


Alexander R. Szumita

May 1, 2014

Approved by:


Professor David J. Olinger, Advisor
Aerospace Engineering Program
Mechanical Engineering Department, WPI


Professor Anthony B. Linn, Co-Advisor
Aerospace Engineering Program
Mechanical Engineering Department, WPI

Abstract

The objective of this project was to design, analyze and build an aircraft meeting the requirements of the 2014 SAE Aero Design Competition, Micro Class. Competition scoring rules favor an aircraft carrying maximum payload but fitting disassembled into an 8"x18"x24" box. Aircraft must be assembled in 3 minutes by two persons. An S1223 airfoil was chosen for max lift at low Reynolds numbers. Wing was 6 equal length panels, totaling 10.6' span. This required a spar of Balsa, Basswood and carbon fiber using sandwich beam construction. Lateral control was accomplished with spoilers and a rudder, longitudinal control with elevators. Structural, aerodynamic, propulsion and stability analyses were performed using numerical and experimental methods and CFD. Aircraft parts were designed for automated manufacture using laser cutting and 3D printing. Empty weight is estimated at 3.5 lbs with a useful load of 8 lbs flying at 8 m/s.

“Certain materials are included under the fair use exemption of the U.S. Copyright Law and have been prepared according to the fair use guidelines and are restricted from further use.”

Acknowledgements

We would like to thank the following individuals and groups for their help and support throughout the entirety of this project.

Project Advisors Professors David Olinger and Anthony Linn

Sponsor Mrs. Marie Planchard and Dassault Systemes Solidworks Corp.

CFD Specialist Dr. Raffaele Potami

Pilot Professor John Hall

General Advice Dr. Adriana Hera, Prof. David C. Planchard, and Siamak Ghorbani Faal

WPI Facilities Staff Paul Wilson and Roger Griffin

Table of Authorship

Section	Author¹
<i>Introduction</i>	RB, AS
1.1	RB
1.2	JS
<i>Initial Design Process</i>	GB, AS
2.1	RB, AS
2.2	AS
2.3	GB, RB
2.4	JS
2.5	GB
<i>Analysis</i>	
3.1	AS
3.2	GB
3.3	GB
3.4	MR
3.5	GB, AS
<i>Preliminary Testing</i>	
4.1	AS
4.2, 4.4	GB, AS
4.3	JS, AS
<i>Fabrication</i>	
5.1, 5.2	RB, GB
5.3	GB
<i>Flight Testing</i>	AS, GB
<i>Recommendations</i>	GB
<i>Conclusion</i>	AS
<i>Appendix A</i>	GB
<i>Appendix B</i>	MR
<i>Appendix C</i>	MR
<i>Appendix D</i>	GB

¹ GB – George Bucsan, RB – Ryan Burgan, MR – Marco Romero, JS – John Stackable, AS – Alexander Szumita

Table of Contents

Abstract.....	2
Acknowledgements.....	3
1.0 Introduction.....	13
1.1 Past Competition Entries.....	15
1.1.1 The 2012 WPI Competition Aircraft.....	15
1.1.2 The 2013 WPI Competition Aircraft.....	16
1.2 Micro Aircraft Applications.....	16
2.0 Initial Design Process.....	18
2.1 Alternative Aircraft Configurations.....	19
2.2 Initial Aircraft Sizing.....	22
2.3 Airfoil Selection.....	24
2.4 Flight Velocities.....	25
2.5 Structural Design.....	26
2.5.1 Wing Structure.....	26
2.5.2 Fuselage Structure.....	33
2.5.3 Tail Boom Structure.....	37
2.5.4 Tail Assembly Structure.....	38
3.0 Analysis.....	45
3.1 Aerodynamic Analysis.....	45

3.1.1 XFLR5 Comparison.....	49
3.2 Propulsion Analysis	50
3.3 Structural Analysis.....	55
3.4 Stability Analysis	63
3.4.1 Modeling the longitudinal steady state aerodynamic forces and moments	64
3.4.2 Modeling the aircrafts lateral steady state aerodynamic forces and moments.....	71
3.4.3 Aircraft Static Stability	80
3.4.4 Aircraft Dynamic Stability.....	81
3.5 Trim Analysis.....	84
4.0 Preliminary Testing.....	86
4.1 Wind Tunnel Testing	86
4.2 Structural Testing.....	88
4.3 Foam Model Glide Testing.....	91
4.4 Thrust Testing	92
5.0 Fabrication	94
5.1 Wing Fabrication	94
5.2 Fuselage Fabrication	98
5.3 Tail Fabrication.....	100
6.0 Flight Testing	102
6.1 Flight Test 1	102

6.2 Flight Test 2	103
7.0 Recommendations for Future Work.....	106
8.0 Conclusion	108
References.....	109
Appendix A – Propulsion Analysis Script.....	110
Main script	110
Secondary Script.....	113
Appendix B – Stability Analysis Formulae	117
Appendix C – Stability Analysis Script.....	123
Appendix D – Flight Test Snapshots	139

Table of Figures

Figure 1: 2013 SAE Micro Class Scoring Estimates	14
Figure 2: 2014 SAE Micro Class Scoring Estimates	14
Figure 3: 2012 WPI Competition Aircraft	15
Figure 4: 2013 WPI Competition Aircraft	16
Figure 5: Final Aircraft Structure/Design	18
Figure 6: Flying Plank Aircraft	19
Figure 7: Wing Area Maximization	20
Figure 8: Score Comparison for the Three Aircraft Configurations	21
Figure 9: Basic Wing Design	22
Figure 10: Basic Fuselage Design	23
Figure 11: Launch Weight and Velocity Curves	25
Figure 12: Sandwich Beam Concept	26
Figure 13: Wing C Structure (Front View)	27
Figure 14: Typical Trailing Edge Rib	28
Figure 15: Adjacent Wing Sections' Connections (Section View)	28
Figure 16: Trailing Edge Ribs with Spring Clip (Section View)	29
Figure 17: Typical wing structure	29
Figure 18: Wings - Fuselage Connections (Section View)	30
Figure 19: Spoiler Actuation System	31
Figure 20: Outer Wing Section Structure	31
Figure 21: Extended Spoiler	32
Figure 22: Fuselage - Wings Joiner Assembly	33

Figure 23: Wing Key Mechanism.....	34
Figure 24: Electrical System Supports.....	34
Figure 25: Payload Assembly.....	36
Figure 26: Fuselage Structure.....	36
Figure 27: Tail Boom Connections (Exploded View).....	37
Figure 28: Aramid Bracing Attachment Points.....	38
Figure 29: Tail Boom Bracing.....	38
Figure 30: Stabilator/Elevator Structure.....	40
Figure 31: Initial Tail Structure (Exploded View).....	41
Figure 32: Tail Trim Device.....	41
Figure 33: Tail Trim Device Geometry.....	42
Figure 34: Final Tail Structure.....	43
Figure 35: Vertical Stabilizer Structure.....	44
Figure 36: Airfoil Lift Coefficient.....	46
Figure 37: Linearized Drag Curve for the Calculation of K_p	48
Figure 38: Comparison of Drag Coefficient Values from Calculations and XFLR5.....	49
Figure 39: Comparison of Lift Coefficient Values from Calculations and XFLR5.....	49
Figure 40: Comparison of Moment Coefficient Values from Calculations and XFLR5.....	50
Figure 41: Engineering Sandwich Beam Notations.....	57
Figure 42: Spar Cap Tension/Compression Stress Diagram.....	58
Figure 43: Spar Web Compression Stress Diagram.....	59
Figure 44: Torsional Parameter k_1 Interpolation.....	60
Figure 45: Torsional Parameter k_2 Interpolation.....	60

Figure 46: Spar Web Twist Shear Stress Diagram	61
Figure 47: Conservation of Linear and Angular Momentum (Napolitano, 10)[8]	64
Figure 48: Aircraft Body and Stability Axis (Napolitano, 80)[8].....	64
Figure 49: Stabilator and Elevator Longitudinal Control Surfaces (Napolitano, 80)[8]	65
Figure 50: Geometric Coefficients for Downwash (Napolitano, 51)[8].....	67
Figure 51: Wing-Tail distances in the longitudinal & vertical directions (Napolitano, 50)[8]	67
Figure 52: Geometric Coefficients for Downwash (Napolitano, 51)[8].....	68
Figure 53: Typical Range for elevator surface effectiveness (Napolitano, 52)[8]	68
Figure 54: Location of the Wing Aerodynamic Center (Napolitano, 53)[8]	70
Figure 55: Steady State Lateral Directional Forces and Moments (Napolitano, 136)[8]	72
Figure 56: Effectiveness of the Rudder as a Function of $C_{Rudder}/C_{Vertical Tail}$ (Napolitano, 149)[8].....	74
Figure 57: ANSYS C-Mesh Domain	78
Figure 58: Modified Airfoil Coordinates for Spoiler Deflection.....	79
Figure 59: Euler Roll Angle Response	83
Figure 60: Euler Pitch Angle Response	83
Figure 61: Pitch Angular Rate Response	83
Figure 62: Roll Angular Rate Response	83
Figure 63: Yaw Angular Rate Response.....	83
Figure 64: Lateral Angle of Attack Response.....	83
Figure 65: Wind Tunnel Wing Test Setup	87
Figure 66: Experimental Lift Coefficient Compared to Theoretical Data	87
Figure 67: Experimental Drag Coefficient Compared to Theoretical Data	87

Figure 68: Fuselage with Central Spar Piece	89
Figure 69: Central Spar Piece Test Setup	89
Figure 70: Joiner Block Test Setup.....	90
Figure 71: Inner Wing Structural Test Setup	90
Figure 72: Foam Test Glider.....	91
Figure 73: Thrust Testing Setup	93
Figure 74: Balsa Rib Set	94
Figure 75: B-Section Spar Webs Ready for Assembly.....	95
Figure 76: Wing Assembly Jig Concept.....	96
Figure 77: Wing Structure Assembly Process	97
Figure 78: Landing Skid Foam Assembly Process	99
Figure 79: Landing Skid Vacuum Lamination	99
Figure 80: Horizontal Stabilizer Assembly Process	101
Figure 81: Flight Test 2 Aircraft Setup.....	103
Figure 82: Flight Test 2 Path (Satellite View)	104
Figure 83: GPS Flight Test Velocity Data.....	105

List of Tables

Table 1: Final Aircraft Parameters.....	19
Table 2: Sample Tail Trim Device Settings.....	42
Table 3: Aerodynamic Coefficients	45
Table 4: Sample Motor Data Compilation.....	51
Table 5: Battery Data Compilation.....	51

Table 6: Sample Propeller Performance Data File (fragment)	52
Table 7: Interim Propulsion Analysis Results Sample	54
Table 8: Density Interpolated Balsa Strength Coefficients.....	56
Table 9: Spar Torsional Parameters Estimation.....	59
Table 10: Wing Structure Factors of Safety	62
Table 11: Static Stability Criteria	80
Table 12: Static Stability Results.....	81
Table 13: Stabilator Trim Table.....	85
Table 14: Thrust Test Data	93
Table 15: Elevator Trim Table.....	103

1.0 Introduction

The purpose of this project was to design and construct a remote controlled aircraft for the Micro Class of the 2014 Society of Automotive Engineers (SAE) Aero Design Competition East Division. The competition provided an opportunity for our team to apply knowledge of basic engineering design principles, aerodynamics, structural mechanics, and aircraft stability while competing against students from around the world. The aircraft was limited by a set of requirements specified by the rules of the competition [1]. The rules require exclusive use of electric motors, a hand launch or an elastic launch system, fitting the entire aircraft (including any launch system) within a 24" by 18" by 8" foam lined box and the use of a payload bay with a minimum size of 2" by 2" by 5". The aircraft must also be assembled in three minutes by two people. The required flight of the micro aircraft consists of a single circuit around a 300 foot field. The aircraft structure must remain intact during the flight and landing. Only the propeller may break on impact.

The competition scoring required the aircraft to carry the heaviest payload possible while maintaining the lowest empty weight. In previous years, maintaining a lower empty weight to payload ratio was more beneficial than carrying a larger payload with regards to scoring in the competition. The scoring equation also limited the maximum empty weight of the aircraft to two pounds, as plotted in Figure 1. In the 2014 competition, carrying a larger payload results in a much higher score. An empty weight over two pounds still results in a negative component in the scoring equation but this negative contribution is much smaller than the contribution of the payload to the score. In each round, the aircraft has one chance to complete a flight around the 300 foot field and if completed, the flight score for that round was given by:

$$R_n = (2 - EW)PF_n + (P_n \sum_1^n P_n) \quad (1)$$

where EW is the empty weight of the aircraft in pounds, P_n is the payload weight, and PF_n is defined as $\frac{P_n}{P_n+EW}$. The possible scores for a single round are shown in Figure 2. The difference between the current and previous years' scoring equations significantly affected the design of our aircraft.

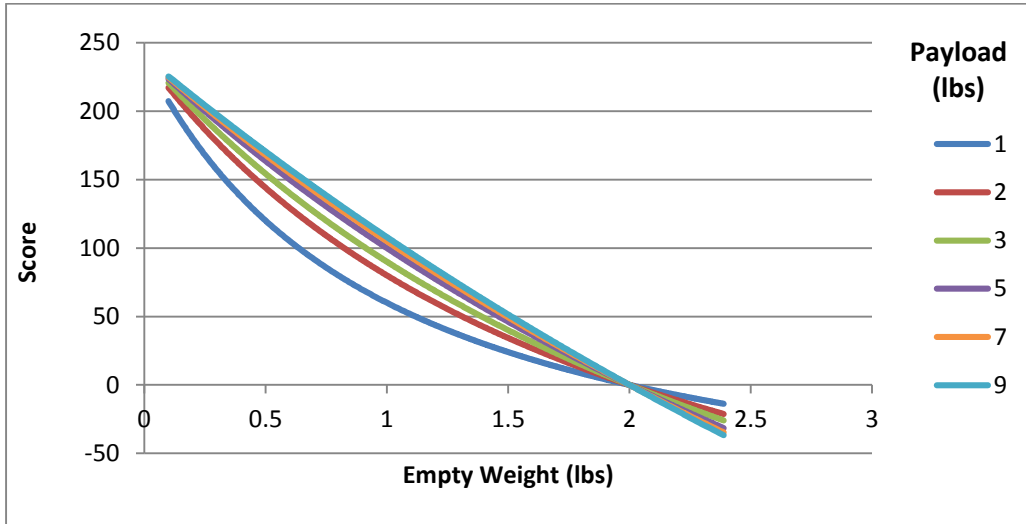


Figure 1: 2013 SAE Micro Class Scoring Estimates

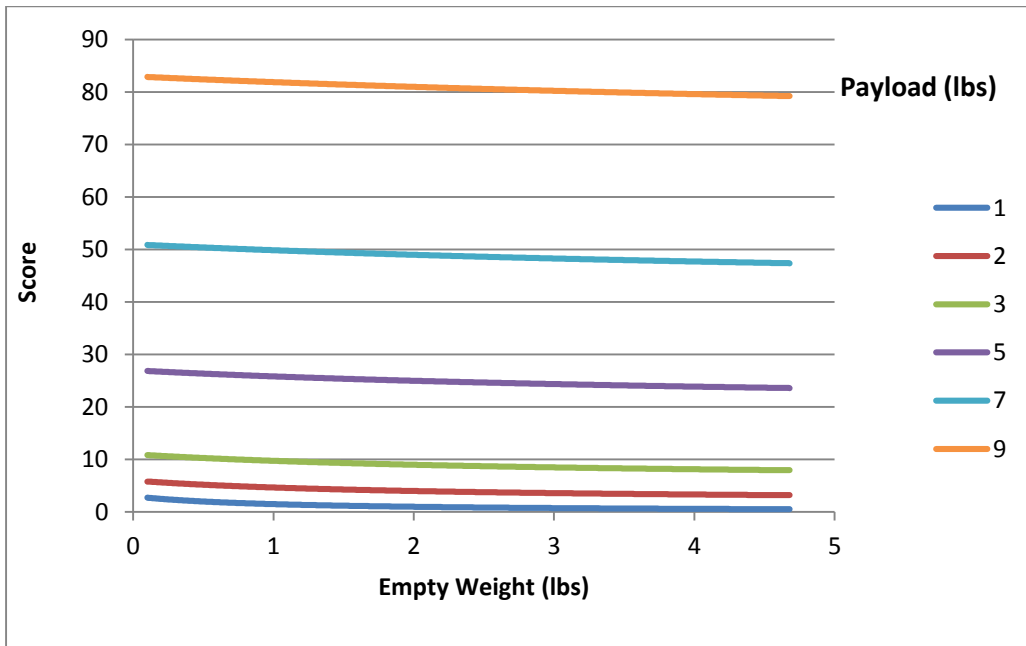


Figure 2: 2014 SAE Micro Class Scoring Estimates

1.1 Past Competition Entries

Before going into detail about any of the past planes, it should again be noted that the scoring rules for these planes were much different than the current scoring rules. The 2012 and 2013 rules focused more on a ratio of the empty weight of the plane to the payload weight, while the 2014 rules are more focused on the total payload that can be carried.

1.1.1 The 2012 WPI Competition Aircraft

This aircraft used a conventional design with a full tail shown in Figure 3 [2]. Each wing was a single piece that could detach from the fuselage for easier storage. The S1223 airfoil was used. It had a positive dihedral on the outer section of the wing. Unfortunately, the plane was not able to lift the desired payload due to not selecting an appropriate motor. The final plane weighed 450 grams and could carry 1285 grams.

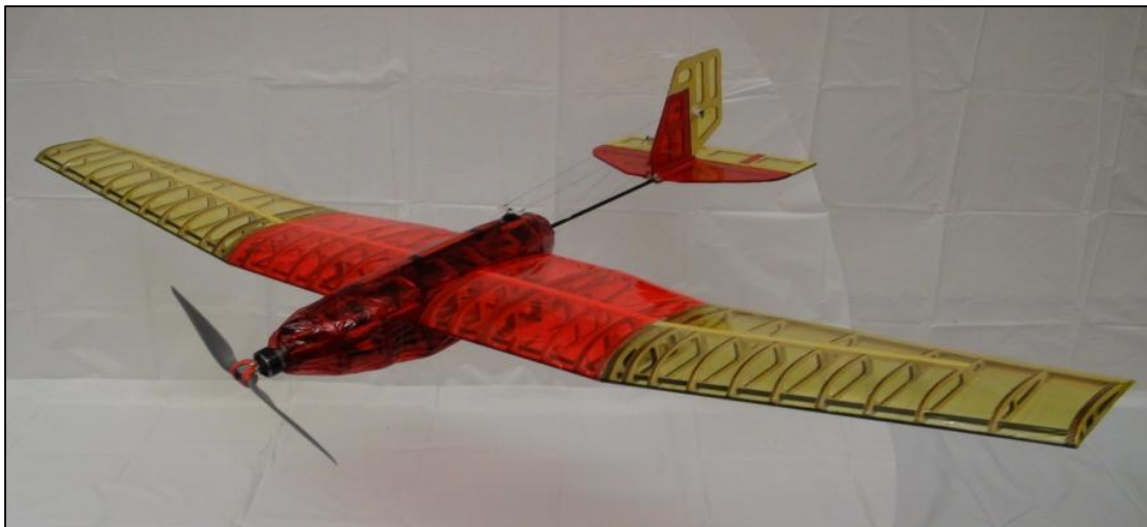


Figure 3: 2012 WPI Competition Aircraft

Apart from some carbon fiber rods in the wings and tail, the aircraft was built from Balsa wood. The entire structure was covered in Mylar. Everything was able to be laser cut which led to easy manufacturing and building.

1.1.2 The 2013 WPI Competition Aircraft

This aircraft used a flying wing design shown in Figure 4 [3]. This plane was one solid unit, except for the wing tips that could detach in order to fit it in the box. Its wings were swept and had twist, which contributed to the stability of the aircraft. It weighed 177 grams and could carry a maximum payload of 480 grams.



Figure 4: 2013 WPI Competition Aircraft

The structures of this aircraft were also all made out of Balsa wood. Because of the taper of the wing, the plane needed to be sanded down to the exact leading edge. The inner structures were laser cut to a thousandth of an inch precision. The entire structure was covered in Mylar.

1.2 Micro Aircraft Applications

Many applications exist for micro aircraft in both the military and civilian field. The military already has made extensive use of unmanned micro aircraft vehicles (MAVs) for both surveillance and weapons systems, such as the Raven RQ-11A. The Raven is a small, 4.5 pound, hand launched surveillance drone currently used by the military [4]. The civilian market is an untapped resource waiting for the development of these useful micro aircraft. Civilian micro

aircraft can carry out many tasks that may prove difficult with larger, conventional aircraft varying from the delivery of supplies to remote areas or even rapidly delivering packages to customers as Amazon has announced is their plan for the coming years [5]. Other applications include search and rescue or even surveillance for police departments. A small, cheap, and easy to manufacture aircraft with a versatile and easily modifiable configuration along with a relatively high payload capability or range could prove invaluable when searching for a lost person at a ski resort or in a national park [6]. A quickly launched aircraft could help track down fugitives in areas that a large, piloted aircraft would be too expensive and too slow to use. The possibilities are endless and micro aircraft stand to revolutionize the field of aerospace engineering.

2.0 Initial Design Process

The final aircraft design is shown in Figure 5. Each wing consists of three detachable sections held together with removable carbon fiber tubes in the spar. A carbon fiber tube, separated into four pieces, runs the entire length of the aircraft and is used as the tail boom and main fuselage structure. The vertical stabilizer acts as the rudder and the horizontal stabilizer consists of two separate pieces with an elevator running along the entire span. Spoilers on the top of the outer wing sections are used for roll control. Propulsion is given by a 250 Watts motor, a 3 cell 1100mAh battery and a 10" propeller.

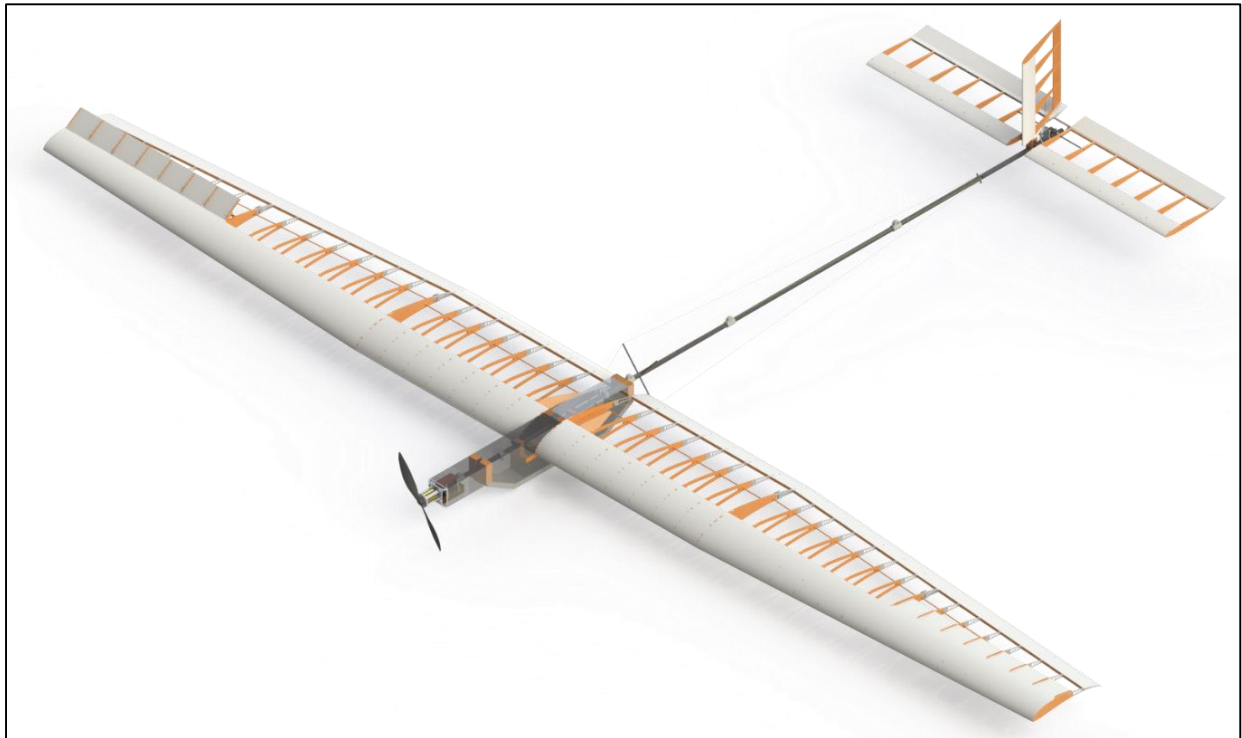


Figure 5: Final Aircraft Structure/Design

Several key aircraft parameters are summarized in Table 1.

Table 1: Final Aircraft Parameters

	Metric units	English Units
Wing Span	3.2 m	10.5 ft
Wing Area	1.0572 m ²	11.38 ft ²
Wing Aspect Ratio	9.69	9.69
Empty Weight	1.59 kg	3.5 lbs
Maximum Design Payload Weight	3.63 kg	8 lbs
Predicted Single Round Flight Score	63	63

2.1 Alternative Aircraft Configurations

Based on the competition rules and scoring, an initial aircraft configuration was determined. The three configurations considered were a flying wing similar to the 2013 WPI design, a flying plank similar to the aircraft shown in Figure 6, and a conventional aircraft similar to the 2012 WPI design. With the goal of carrying the largest payload, the basic design of each configuration was optimized for maximum lift. An airfoil was selected for each aircraft based on the stability needs of each type and the maximum wing area that could fit in the 24” by 18” by 8” carrying case was determined for each configuration.

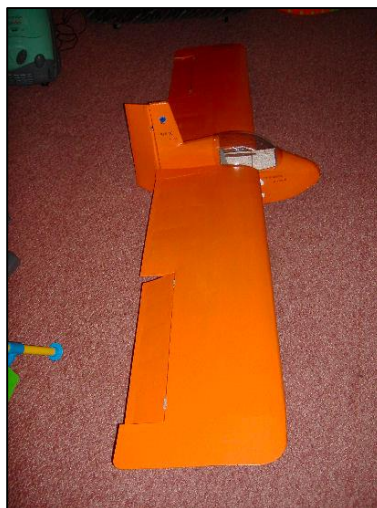


Figure 6: Flying Plank Aircraft

The conventional aircraft airfoil was selected based on the need for high lift at a low Reynolds number. Since the aircraft has a tail to balance any moment generated by the wing, a cambered airfoil could be used. The S1223 was chosen for the initial conventional configuration because it had the highest lift coefficient at low Reynolds numbers, smooth stall characteristics, and because it worked well on the 2012 WPI aircraft. The camber of the airfoil, combined with a 60% taper on two thirds of each wing allows six wing sections to be stacked within the 8 inch height of the carrying case, as shown in Figure 7. Each section could be 21 inches long (15 inch wing root chord) while still allowing space for the fuselage, tail, payload, and electronic components in the case, resulting in a 11.38 square foot wing area.

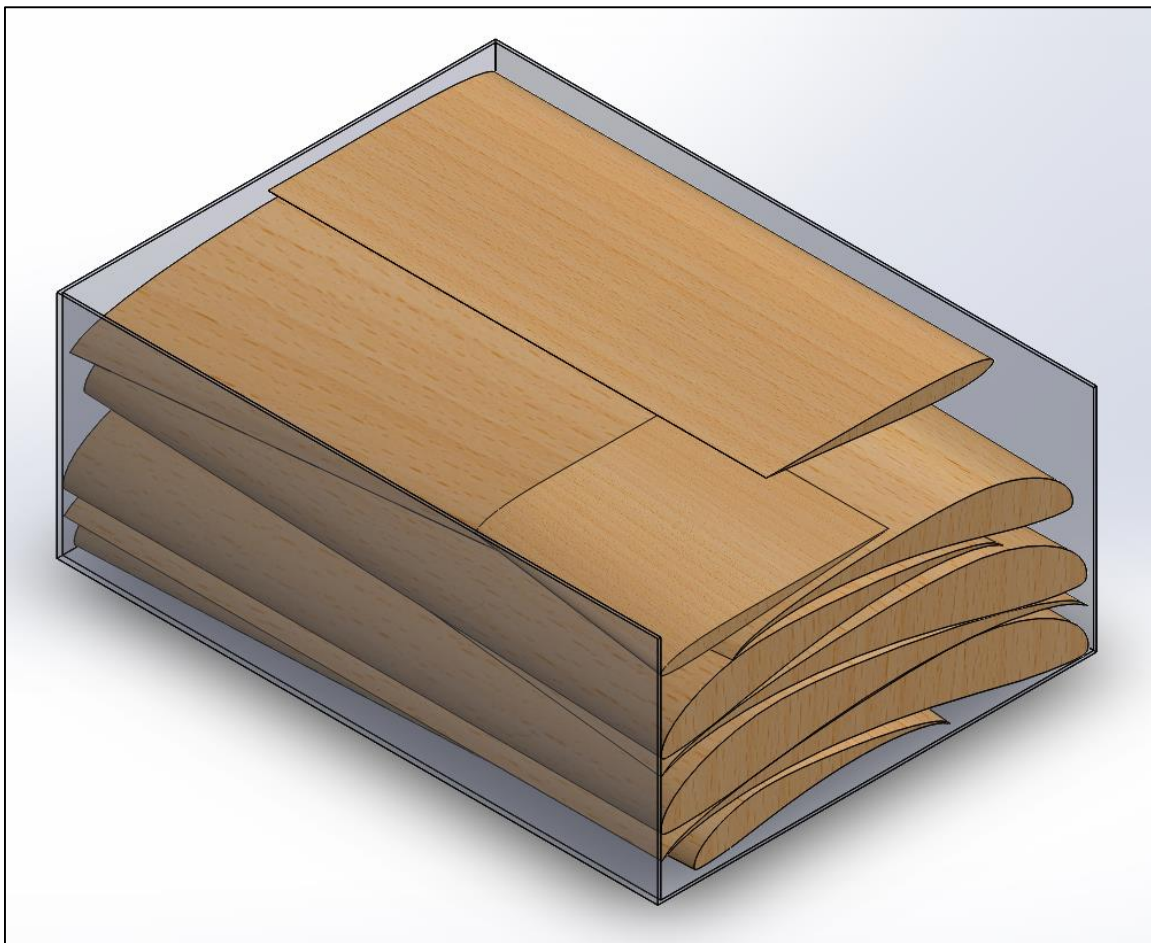


Figure 7: Wing Area Maximization

The flying plank required a reflexed airfoil with a positive moment coefficient to stabilize the aircraft. However, this results in a loss of lift. The FX-66-H-80 was chosen but a flying plank would likely need an airfoil with a higher pitching moment and smaller lift coefficient. With the reduced thickness of this airfoil compared to the S1223, eight straight wing sections that are 24 inches long could fit in the box for an area of 20 square feet.

For the flying wing, the MH60 airfoil was selected since it has a moment coefficient close to zero and a reasonably high lift coefficient. Due to the necessary sweep of the wings, only 4 wing sections would fit in the case resulting in a wing area of 5 square feet.

The possible score for each configuration at varying launch speeds is shown in Figure 8. The total weight of each aircraft was determined by the lift generated based on Equation 2.

$$L = \frac{1}{2} C_L \rho v^2 S \quad (2)$$

The empty weight was also estimated based on the wing and tail area. For these preliminary calculations, we assumed that the battery, servos, fuselage, and motor would weigh approximately the same amount for all three aircraft. Therefore, their weight was neglected since it does not affect the relative score of each configuration. As shown, the conventional aircraft had the potential to receive the highest score and was therefore chosen for the aircraft.

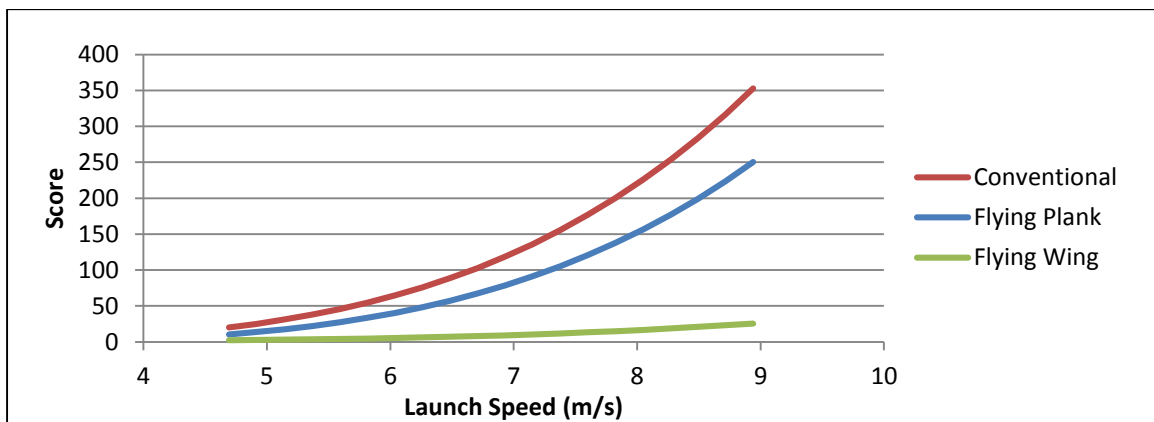


Figure 8: Score Comparison for the Three Aircraft Configurations

2.2 Initial Aircraft Sizing

The size of each component was determined based on some basic calculations. The previously described conventional wing design included a taper ratio of 0.6 in the two outer sections of each wing, resulting in a chord of 9 inches at the wing tips. This taper ratio was chosen based on typical values provided by Raymer [7] for an approximately elliptical lift distribution, as well as box fitting. To simplify the fabrication of the wing spar, the quarter chord was aligned along the entire wingspan as shown in Figure 9 (spoiler not shown).

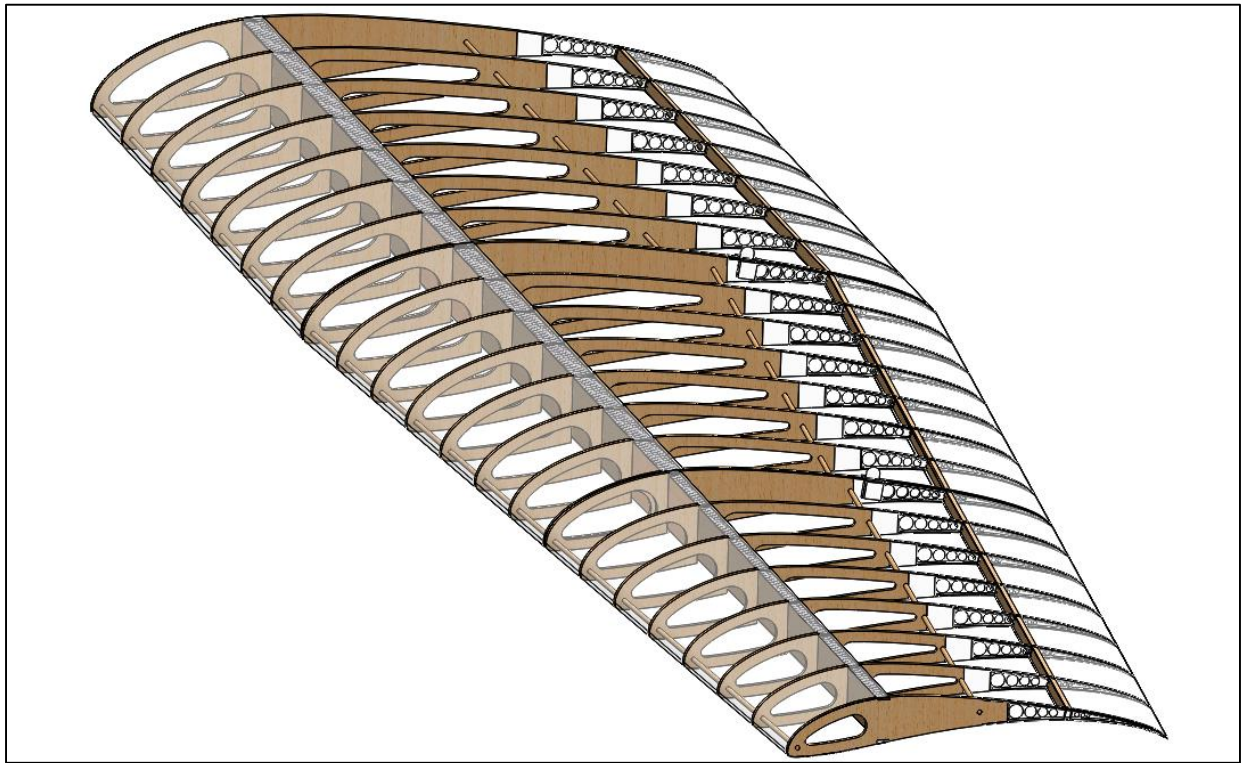


Figure 9: Basic Wing Design

The fuselage, as shown in Figure 10, was sized based on the payload requirement and the space left in the storage box. According to the competition rules, the payload bay was required to be at least 2" by 2" by 5", resulting in a payload weight of 5.7 pounds for a steel payload. To allow for the expected higher weight, the payload bay length was extended to 7 inches. The fuselage had

to fit inside the box along with the wing sections and the foam, thus its width was set to a maximum of 2.4". Similarly, the length of both the fuselage and the tail boom sections was set to a maximum of 23".

The size of the tail boom, horizontal stabilizer, and vertical stabilizer were based on the tail volume coefficients used by Raymer [7] and the aspect ratio of the stabilizers.

$$VC_{ht} = \frac{l_{HT} S_{HT}}{c_W S_W} \quad (3)$$

$$VC_{vt} = \frac{l_{VT} S_{VT}}{b_W S_W} \quad (4)$$

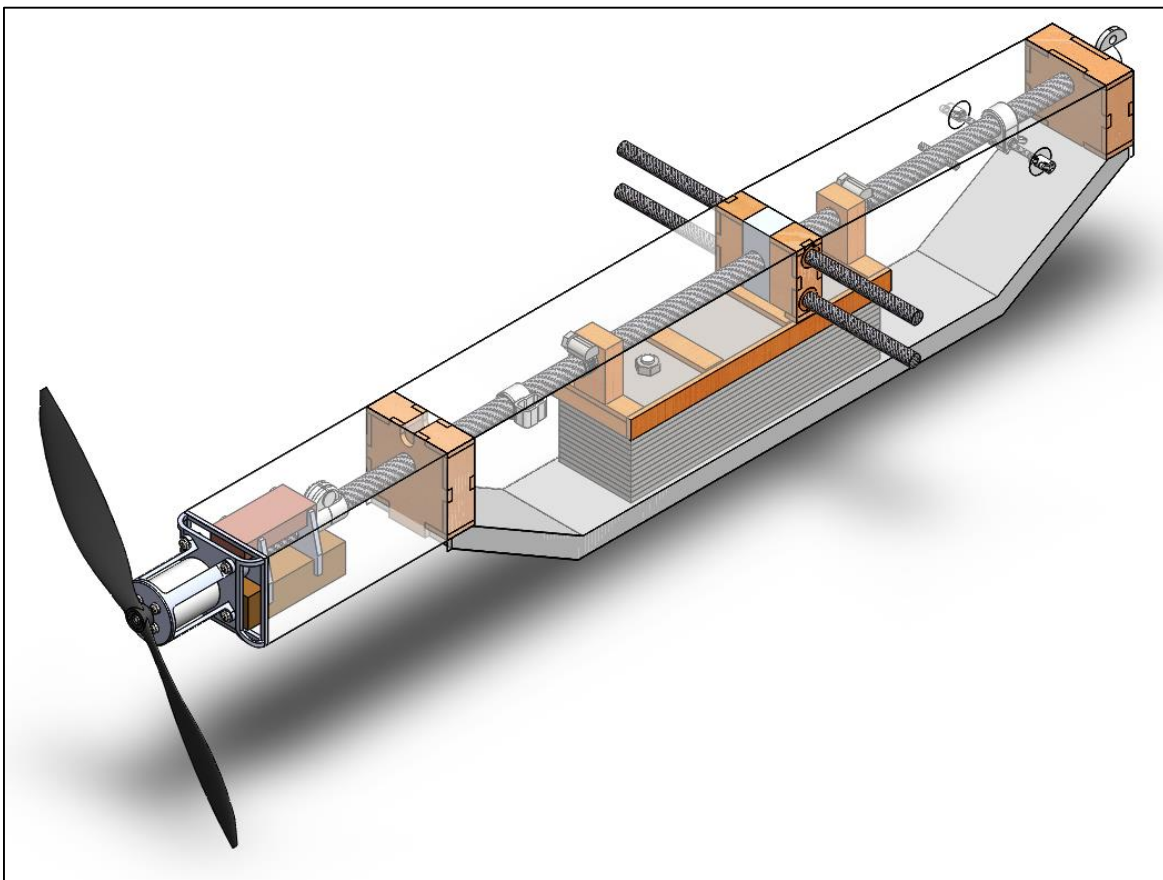


Figure 10: Basic Fuselage Design

Typical values for the horizontal and vertical tail coefficients for full sized aircraft were given as 0.5 and 0.02 for a sailplane and 0.7 and 0.04 for a general aviation, single engine aircraft, the two types assumed to be the closest to our aircraft. Typical values for the aspect ratios were given as 4 for the horizontal tail and 1.4 for the vertical tail. These values could not be exactly met due to the large tail size necessary. The tail boom length (l_{HT} , l_{VT}) was set to 4 feet and the horizontal and vertical tail areas were set to 2 ft.² and 0.5 ft.². This resulted in values of 0.82 and 0.023 for the horizontal and vertical tail volume coefficients and 4.375 and 1.27 for the aspect ratios. These values and equations were used for a first estimate of the tail size and later verified and refined with the stability analysis. As for the wings, the length restriction on the stabilizer elements' spans was set to 21”.

2.3 Airfoil Selection

With the overall configuration of the aircraft determined, the airfoil selection process was revisited and conducted in more detail. To start this process, a range for camber and thickness was determined. An airfoil with high camber and thickness generates more lift but also a high pitching moment and drag coefficient. This led to a range of 6-10%. A thickness range of 8-14% was estimated to ensure the wings can be strong enough to survive a rough landing but not too heavy or with too much drag. Minimum values were also set for the maximum lift coefficient and the maximum lift-to-drag ratio.

The filtered list was ordered by the maximum lift ratio and the top twenty were evaluated. The lift coefficient and lift-to-drag ratio at the designed Reynolds number were important factors. Stall behavior was also considered since the aircraft has to be hand launched and the take-off angle of attack cannot be accurately controlled. The potential to stack the airfoils and the manufacturability were included in the qualitative analysis. The decision was to keep the very

popular high lift low Reynolds airfoil, the Selig S1223, for the wings. A similar analysis with more emphasis on low drag and very good stall behavior was made for the horizontal and vertical stabilizers and resulted in choosing the S8025 and the S9033.

The angles of attack for cruise and launch were initially set to 4° and 8° in order to use a small drag coefficient at cruise velocities and a reasonably safe angle of attack during launch.

2.4 Flight Velocities

Considering the wing and tail configurations fixed, the launch speed is the parameter that gives the maximum payload. This was determined experimentally by throwing incrementally heavier dumbbells and measuring the velocity with a radar gun. The velocity-weight curves for the aircraft and the person that launches it can be seen in Figure 11. The intersection shows a launch velocity of 7.22 m/s for a total weight of 11.8 lbs.

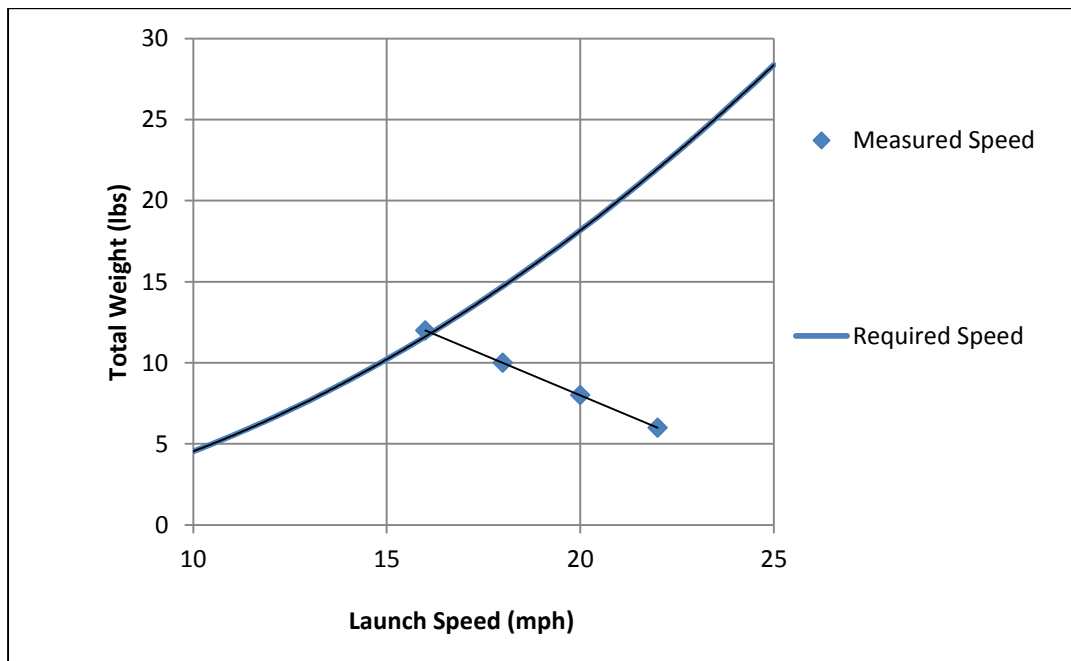


Figure 11: Launch Weight and Velocity Curves

2.5 Structural Design

2.5.1 Wing Structure

The large span of the wings required a light weight spar that could withstand high bending moments with a relatively low deflection. The sandwich beam design, commonly used in competition RC aircraft, was found to be the most appropriate in terms of strength, weight and manufacturability.

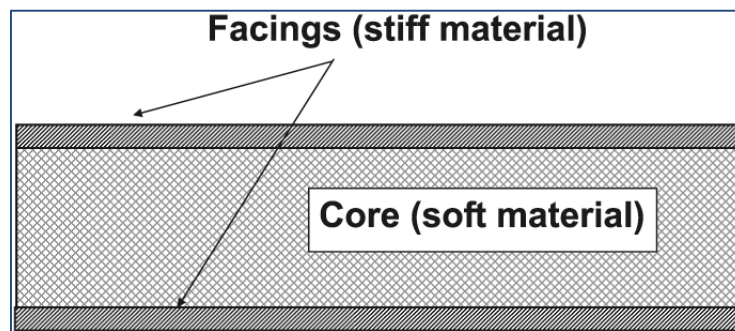


Figure 12: Sandwich Beam Concept

A sandwich beam (Figure 12) consists of two thin skins or faces loaded in tension and compression and a low density core loaded in shear and compression meant to keep the distance between the skins almost constant. For the skins, the chosen material was pultruded carbon fiber strips due to the high fiber volume and commercial availability. For the core, contest grade Balsa wood with a vertical grain orientation (end-grain) was the ideal material due to the availability and manufacturability. Epoxy resin was used to bond the faces to the core. To prevent de-lamination and failure, Aramid tow was wrapped around the entire sandwich structure and locked in place with epoxy and a thin Balsa wood strip. In order to improve the strength, the height was maximized, thus the spar follows the thickness of the airfoil at quarter-chord. Due to the taper of the two outer wing sections and the shear force/bending moment distribution, the thickness of the carbon fiber skins gradually decreased for the two inner wing sections and the width of the spar

decreased for the outer most section. The skeleton of a wing along with a front view of an Aramid-bound spar can be seen in Figure 13.



Figure 13: Wing C Structure (Front View)

In order to maintain a clean and precise airfoil, the ribs were designed to be laser-cut from Balsa wood. Since this material would not be appropriately strong for the very thin and relatively long trailing edge, rapid prototyped ABS plastic trailing edge ribs were designed. The structure of the trailing edge ribs consisted of an I-beam with box-type sockets to connect with the wood rib sections. A minimum value of 0.5" was chosen for the thinnest point of the wood trailing edges. Birch wood dowels and Balsa wood pieces were used to prevent the collapse of the ribs on a span-wise direction, to support the Mylar film cover and to stiffen the entire structure. Balsa wood triangles with 45° (horizontal) grain were used to stiffen the end ribs of each section. A typical 3D-printed trailing edge can be seen in Figure 14.



Figure 14: Typical Trailing Edge Rib

The high moment coefficient of the airfoil resulted in a considerable twisting moment across the structure. Since the tall thin sandwich beam is not ideal for torsional loads, a D-box approach was used. The leading edge was covered in a 0.005” thick PET film (drafting film) that attaches to the spar to provide the necessary stiffness while maintaining the airfoil shape. The same material was used to cover the thinnest (< 0.25”) sections of the trailing edge due to the high stiffness in comparison to the typical Mylar used in this type of aircraft.

In order to connect every adjacent wing sections, two pultruded carbon fiber rods were used. The spacing between the rods is maximized to improve bending strength and the thickness of the rods decreases from the root of the wing to the tip. Since failure tests showed that Balsa wood is not strong enough for this joiner type, the end sections of the spar shear web (core) were manufactured from Basswood, as it is emphasized by different colors in Figure 15.

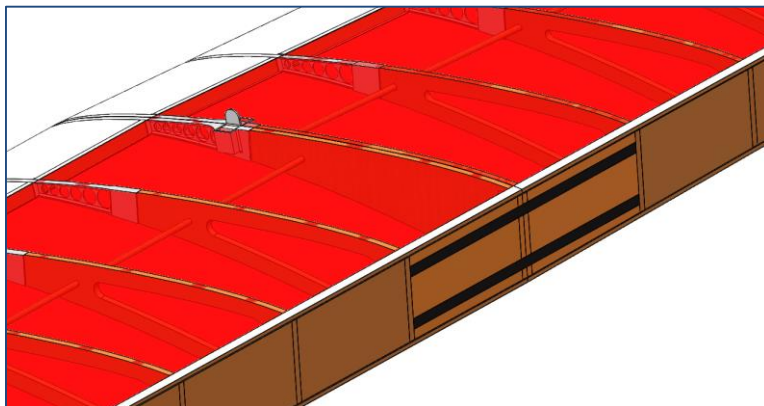


Figure 15: Adjacent Wing Sections' Connections (Section View)

To ensure that the wing sections do not slide on a span-wise direction, sockets for rapid prototyped spring clips were included in the outer trailing edge ribs design (Figure 16).

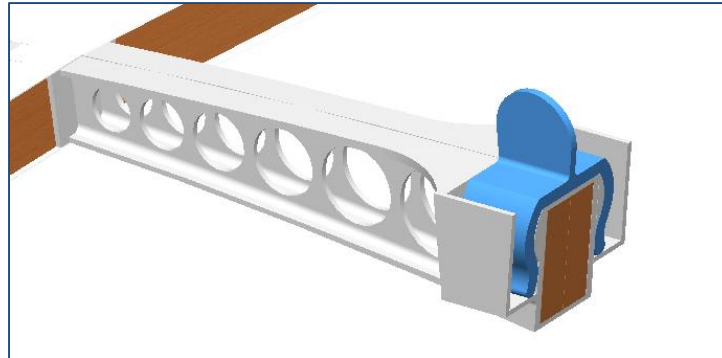


Figure 16: Trailing Edge Ribs with Spring Clip (Section View)

Because tests showed that the outer most ribs would be crushed between the Basswood elements holding the Carbon fiber rods, the end ribs of every wing section have been split into three sections, the middle one consisting of Basswood. The resulting structure of a typical wing section (without a spoiler or Aramid binding) can be observed in the Figure 17.

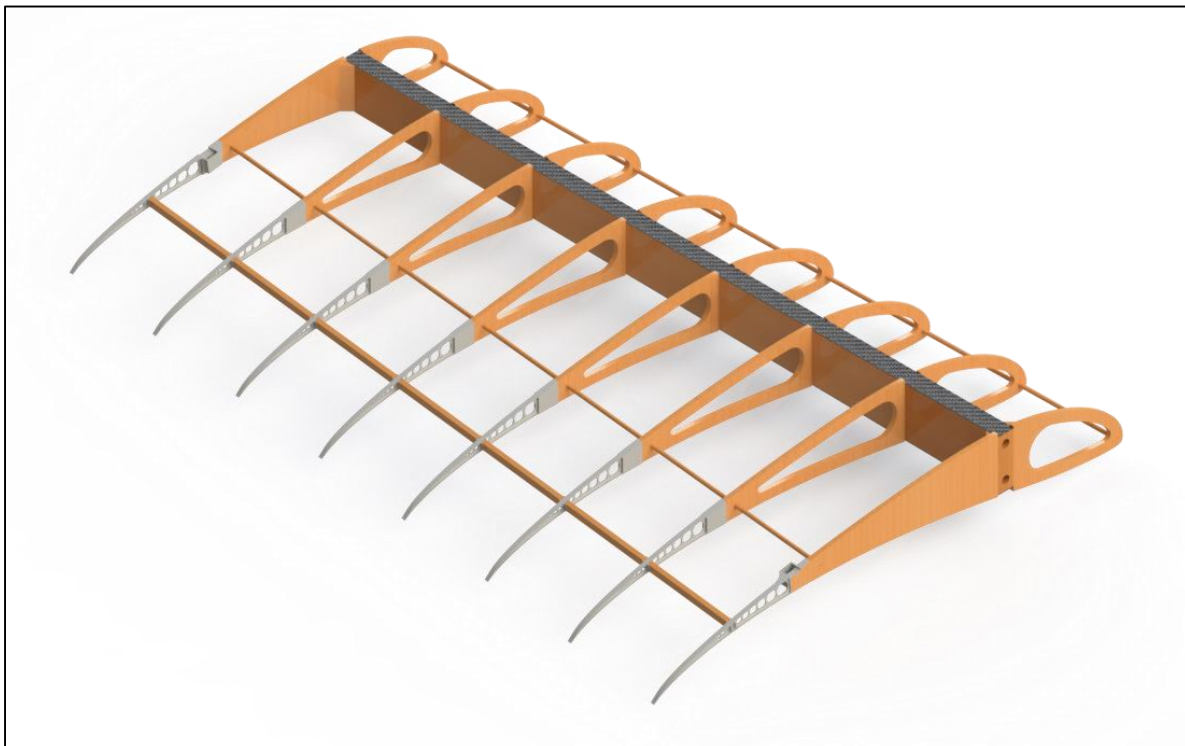


Figure 17: Typical wing structure

The connection between the wings and the fuselage was based on two solid pultruded carbon fiber rods that spanned from the Basswood joiner of the left wing, through the fuselage central joiner, into the Basswood joiner of the right wing. In order to align the two wings perfectly and to hold them in place on a span-wise axis, a key lock mechanism based on a carbon fiber rod with 3D-printed components was designed. During assembly, the key (rod) will be inserted and twisted in place into the fuselage; the position of the end elements would be parallel to the wing chords. The wings would then slide all the way in and the key device would be twisted to firmly secure them in place. Figure 18 shows the two carbon fiber rods and how the key device locks onto one wing.

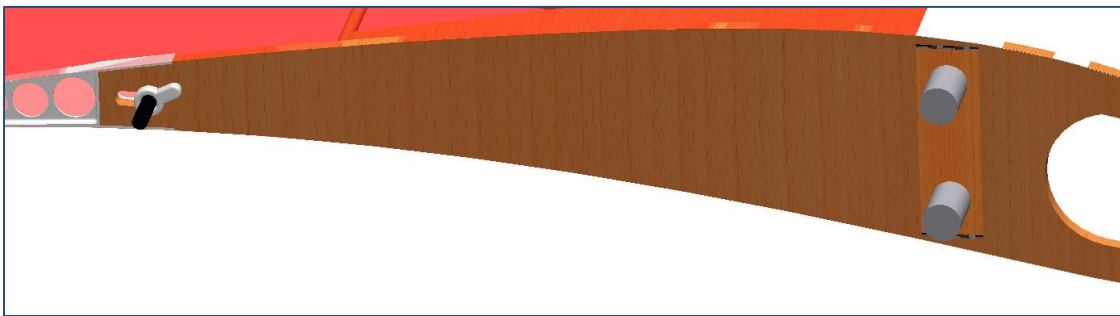


Figure 18: Wings - Fuselage Connections (Section View)

For the outer wing sections, spoilers were added to the design. Perfectly aligned semi-rectangular sections were designed to be cut from the Balsa wood ribs. They were then assembled with the aid of two span-wise carbon fiber rods, one of which also acted as a hinge. Two small 3D-printed components acted as middle hinge points while holes laser cut into the end ribs acted as the end hinge points. Covering the spoiler top surface in a rectangular sheet of 0.005” PET film that overlaps with the Mylar in the rear stiffened the structure and streamlined the spoiler. Two laser cut acrylic elements were used to create a four bar linkage (along with the servo arm) that actuates the spoiler (Figure 19). To connect these elements, thin steel wire from paperclips was

used. The structure of a wing section equipped with a first-design spoiler (not extended) can be seen in Figure Y.

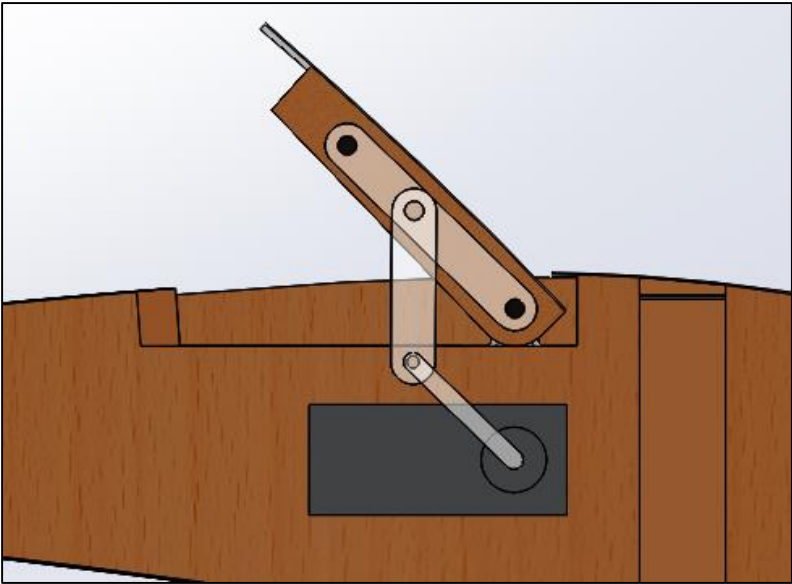


Figure 19: Spoiler Actuation System

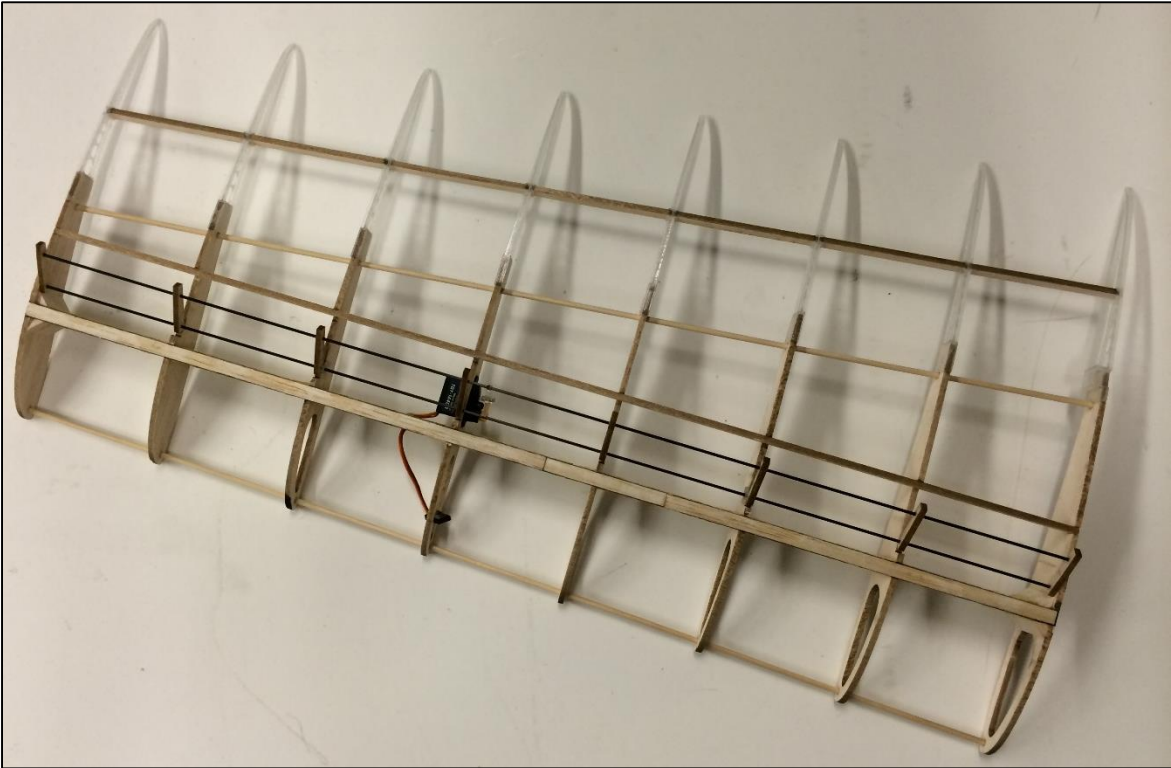


Figure 20: Outer Wing Section Structure

Following the first flight test, the spoilers were extended. Since the internal structure did not allow for alterations, and because just extending the PET film would not provide enough stiffness to the added part of the spoiler, a different solution had to be found. The PET film was extended and reinforced on the outside with vertical, thin (1/32") Basswood profiles, approximately an eighth of an inch tall. The fairing between the PET and basswood was made with thick CA glue in order to lock the reinforcement in place and further stiffen the structure. Careful tests had to be made to determine if the added thickness of the outer wing sections would negatively affect space in the box. Figure 21 shows the extended spoilers.

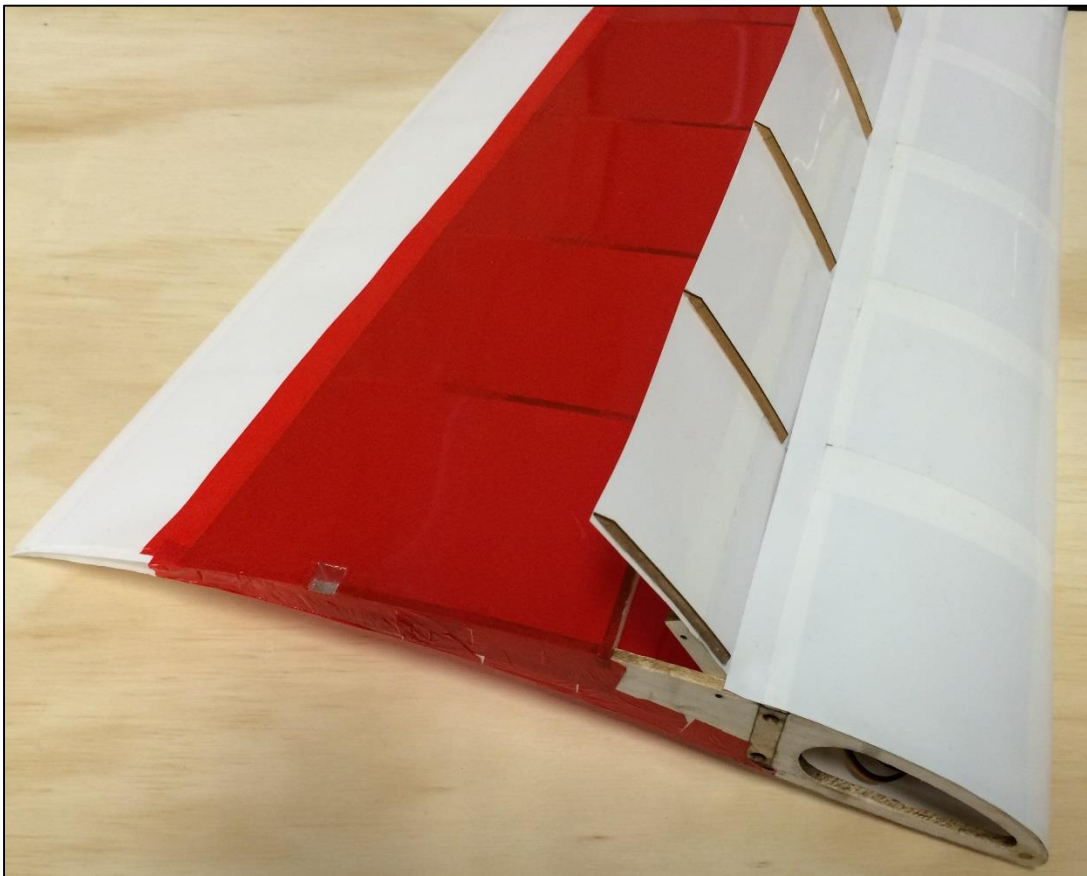


Figure 21: Extended Spoiler

2.5.2 Fuselage Structure

The fuselage was designed around a central, woven Carbon fiber tube that extends to comprise the tail boom. One machined Basswood element was first used to connect the rods joining the wings to the central tube. Following a flight test in which the Basswood absorbed the impact by splitting along the grain, the fuselage central joiner was milled from solid Aluminum. Since not the entire distance between the two wing end-ribs (inside the fuselage) has to be filled with a solid material, the fuselage central joiner was made just big enough to safely connect the two wing rods to the fuselage central tube. The rest of the space was filled by two half-boxes assembled from laser-cut Basswood with carefully chosen grain orientation. These wooden half-boxes fit the requirements since they only need to withstand compression forces on a span-wise axis. The assembly, in its partly-Aluminum version, can be seen in Figure 22.

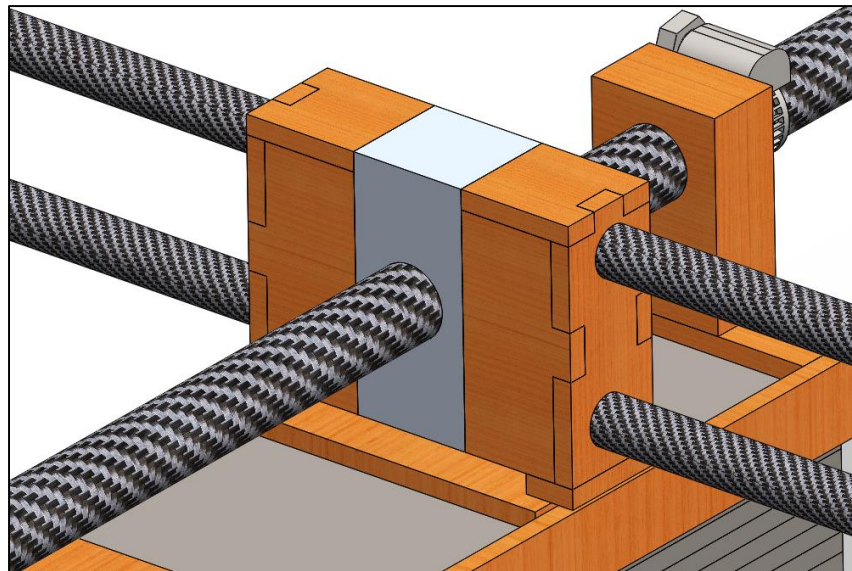


Figure 22: Fuselage - Wings Joiner Assembly

To ensure that the wings do not slide out, a rapid prototyped plastic key-type mechanism is used. The device could not be fixed in place since it has to extend through the end ribs of the wings and thus be wider than the fuselage itself. To avoid this box fitting problem, the key was

designed to slide into the socket permanently fixed to the fuselage during assembly. The key mechanism can be seen in Figure 23.

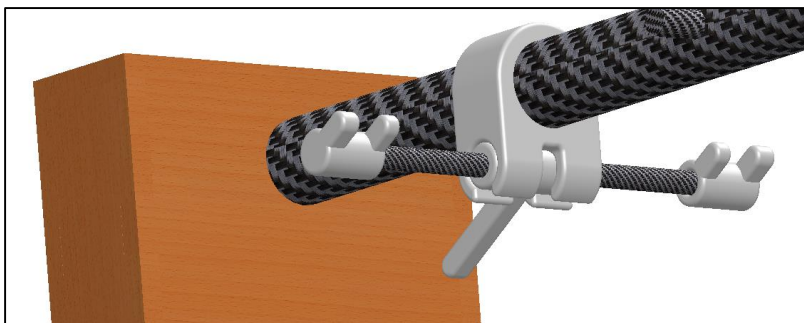


Figure 23: Wing Key Mechanism

Rapid prototyped ABS brackets were first used to fix the battery, motor controller, shunt plug, and wing “key” hub to the central tube. Following a flight test, the simple electronic brackets were replaced with similar parts laser cut from Delrin plastic, such that they can handle landing shocks easier. A cage type 3D printed Nylon plastic bracket is used to attach the out-runner type motor in front of the central tube through a “firewall”. Initially, both the cage and firewall were printed in ABS plastic; flight tests showed that a more energy absorbent material, such as Nylon, is needed. Figure 24 shows the electronic supports.

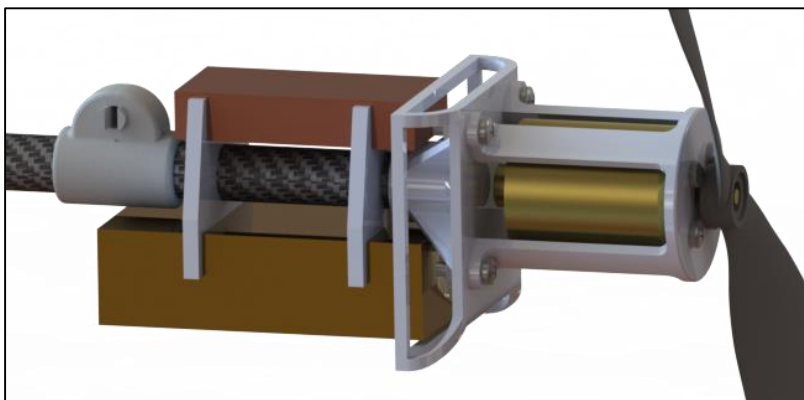


Figure 24: Electrical System Supports

Since the weight of the payload is a few times larger than that of the empty aircraft, any change in the amount of payload carried can affect the location of the center of gravity and thus

the stability. To avoid this problem, a cradle was designed to slide along the central tube to adjust the payload location. The payload plate assembly is held in place in the horizontal plane by the cradle, which is locked longitudinally by pipe clamps fastened to the central rod. In the vertical axis, the payload is suspended from the central tube by fabric hook and loop fastener strips (Velcro).

For landings, a removable skid made of Polymethacrylimide (PMI) rigid closed cell foam (Rohacell), vacuum laminated with epoxy resin and a very thin fiberglass cloth is designed to impact the ground. The skid can transfer the loads to the central tube through two Balsa wood boxes with carefully chosen grain orientation and through the payload assembly, if present. The dimensions of the skid were calculated such that the payload assembly can slide enough in both directions to offer the proper stability parameters.

Because the skid is able to transfer landing impact forces through the payload assembly if the assembly is 2 inches tall, the payload plates and the bolts holding them together had to be carefully designed. Using holes that can fit the outer diameter of the nuts through some of the payload plates and countersunk, flat head machine screws, the assembly is perfectly flushed at the bottom (side that touches the skid) and can be 2 inches tall with as few as two payload plates. The payload assembly can be seen in Figure 25; all other plates besides the end ones are shown as transparent for clarity.

A simple, removable 0.005" PET film is used to cover the contents of the fuselage. The advantage of the design is that there is no need for a heavy wood structure to fully enclose and hold the payload. On the first section of the fuselage (electronics section), the covering film – rectangular in section - is designed to just slide in, from the side of the motor towards the tail. On the second section of the fuselage (payload & joiner section), the film is glued to the left side of

the landing skid and just folds over the top of the fuselage joiner/boxes. Clearance holes are stamped out for the wing joiner rods, locking key and shunt plug. The entire fuselage structure can be seen in Figure 26.

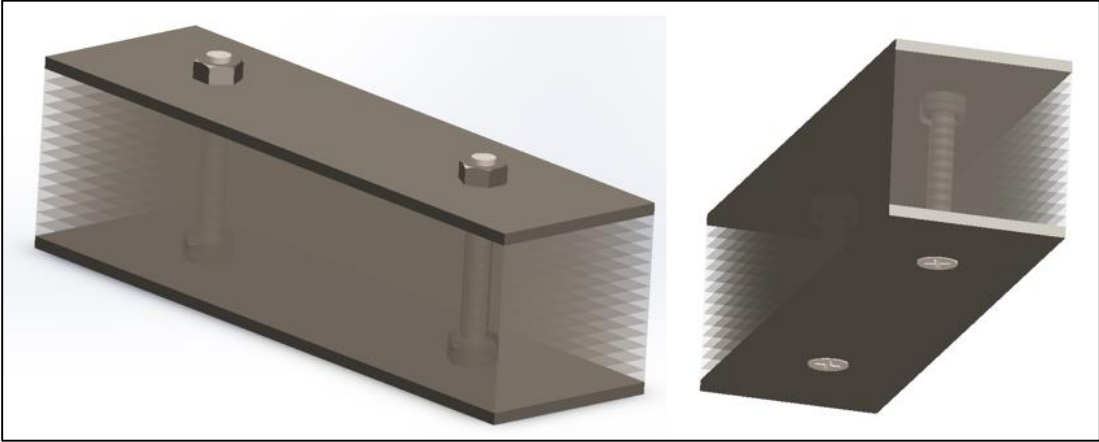


Figure 25: Payload Assembly

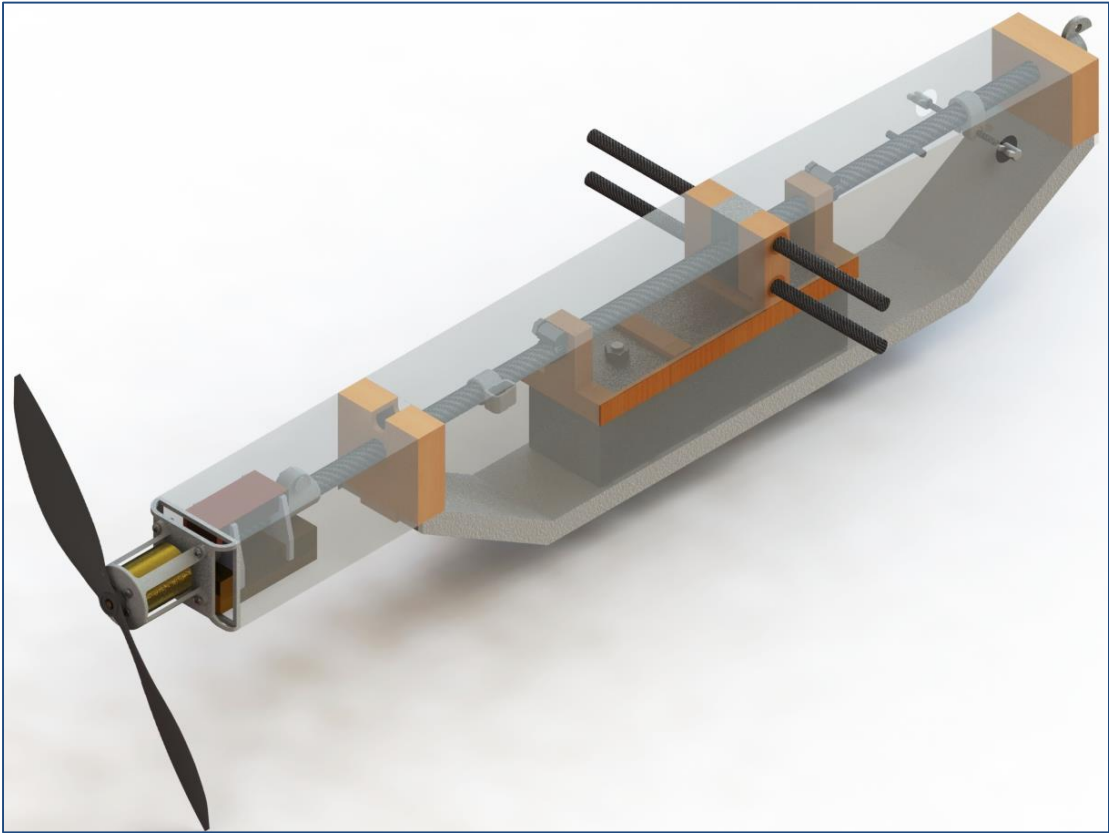


Figure 26: Fuselage Structure

2.5.3 Tail Boom Structure

In order for the tail boom to be as stiff as possible but still fit in the box, it was designed to break into sections and assemble with very tight tolerances. For this purpose, matching pairs of carbon fiber tubes and ferrules were used. To ensure that the elements do not slide out or twist, locking devices based on spring clips were rapid prototyped, as can be seen in Figure 27.

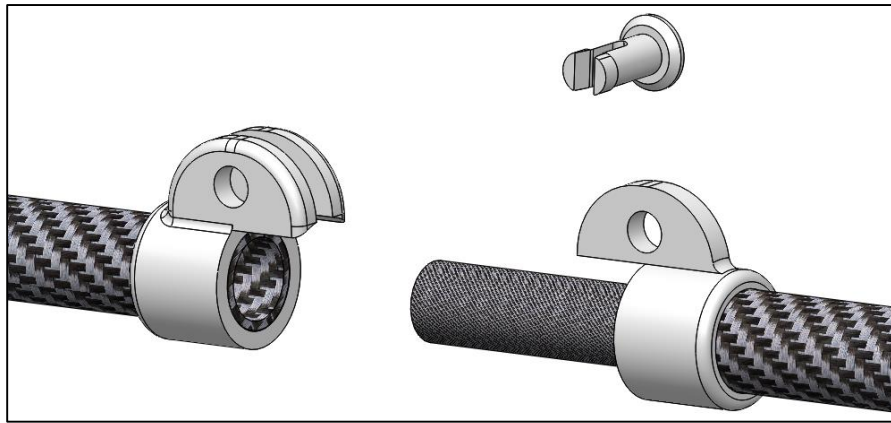


Figure 27: Tail Boom Connections (Exploded View)

Since the relatively thin carbon fiber tube alone proved not to be stiff enough in dynamic bending, a bracing scheme was devised. Two pultruded carbon fiber rods were used as spacers in the very front of the tail boom; the material was deemed ideal due to the predominantly compression loads. Four Aramid (Kevlar) threads were used to brace the tail boom in two almost orthogonal planes. The wires were designed to be bonded to the rear section of the tail boom and to attach to the forward section through the use of loops. Notches were designed to be cut at both ends of the spacers; these ensure that the wires do not slide out. For ease of assembly, washers were glued to the spacers to ensure that they do not slide into the tail boom tube more than needed, thus keeping symmetry and equal wire tensions (Figure 28).

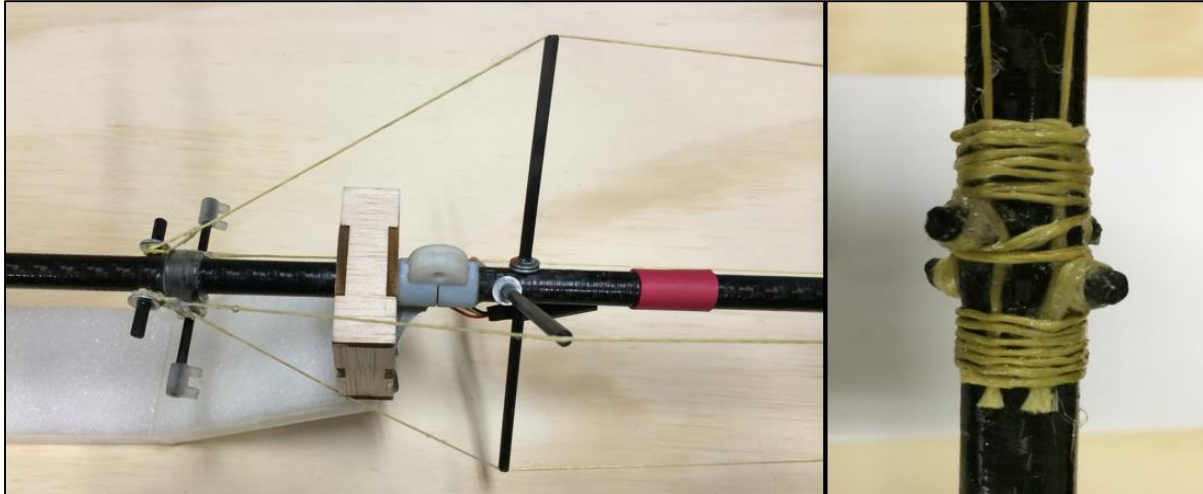


Figure 28: Aramid Bracing Attachment Points

Even though calculations on the possible stiffening effect of the bracing can be and were made, due to the unknown wire tension they were not used in the design process. During assembly, the wires were tensioned as much as possible and to similar values. A side view of the final bracing design can be seen in Figure 29.

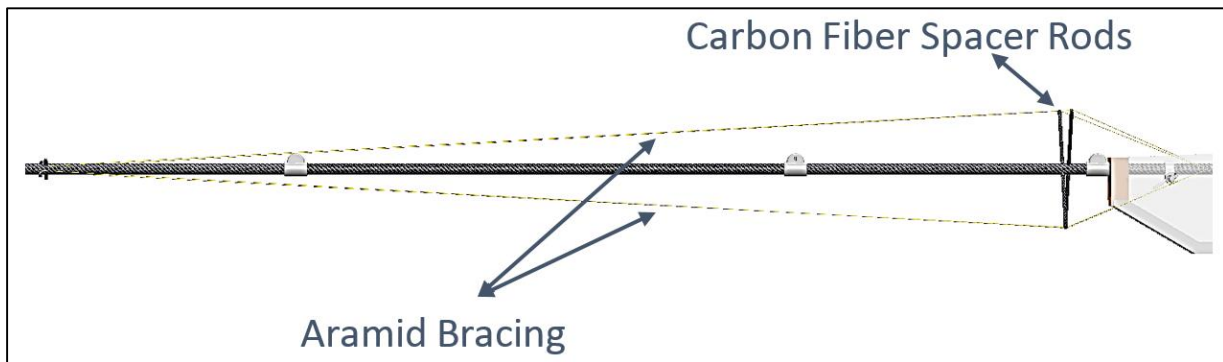


Figure 29: Tail Boom Bracing

2.5.4 Tail Assembly Structure

The horizontal tail structure was based on the wing structure with the addition of the elevator. The front spar was thinned down to 1/8 inches and a rear spar was added for extra torsional stiffness. The leading edge D-box was also kept for, in this case, much needed torsional stiffness. The aft part of half the ribs – up to the rear spar – are glued to 3D printed elements

designed to connect to the rear spar and to provide hinge points for the elevator. The elevator is comprised of I-beam sectioned, rapid prototyped trailing edges hinged on a carbon fiber rod. The airfoil section just preceding the elevator (one inch long, chord-wise) is covered in a 0.005" PET film and overlaps onto the elevator, to provide a smooth surface for the incoming flow. The elevator ribs are themselves covered in the same PET film for stiffness.

Two quarter-chord-aligned carbon fiber rods are used to connect the two halves of the horizontal stabilizer to the tail boom. The spar web section that holds the two carbon fiber rods was too thin to allow for drilling. Thus, a solid Basswood element as thick as the Balsa spar webs was laser cut and placed between the two rods. The Basswood spar-web element and the carbon fiber joiner rods were covered in epoxy resin and sealed in place by two thin, 1/32" Basswood sheets (one on each side). The top and bottom of the structure also covered in resin and then sealed in place by the 1/8" wide carbon fiber spar caps. This can be observed in the figure below, with the note that the front thin Basswood sheet is set as transparent for clarity. Also, a third carbon fiber rod, spanning just over two ribs, was used around the half-chord point to ensure that the angle of incidence of both stabilator halves is precise. The structure of the horizontal stabilizer and elevator assembly can be seen in Figure 30.

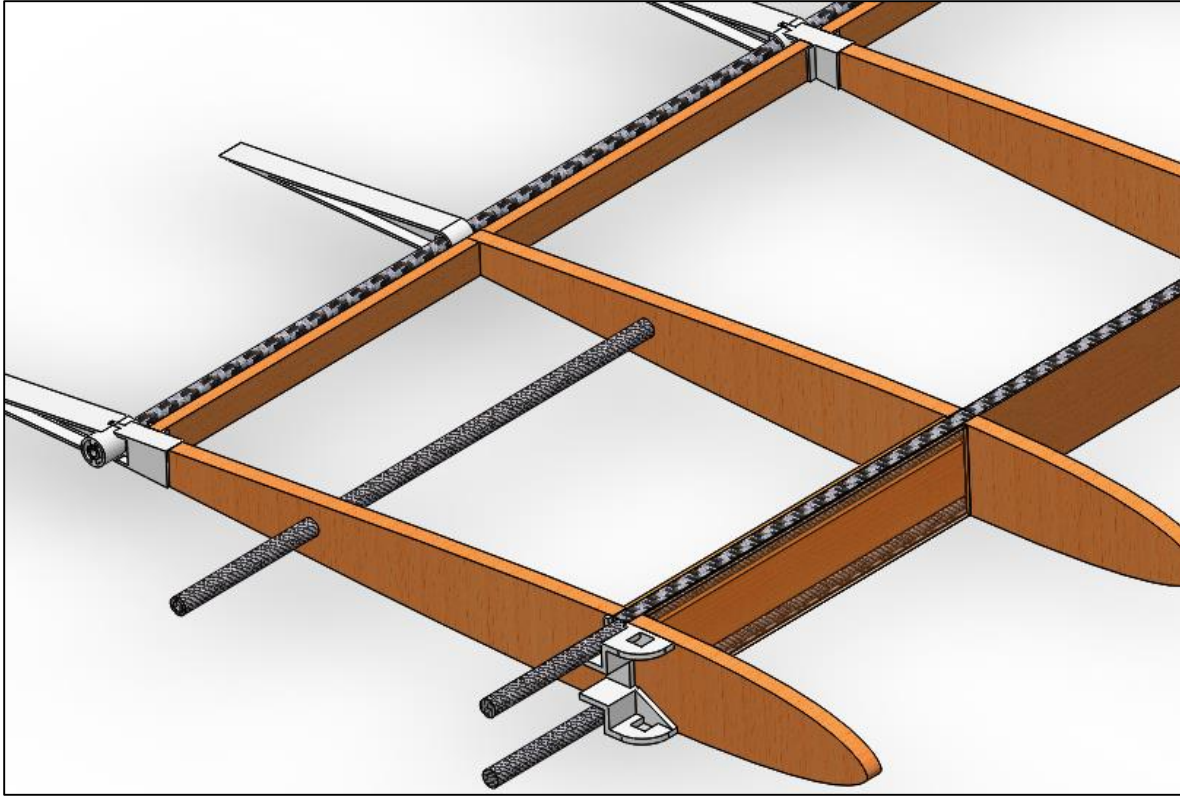


Figure 30: Stabilator/Elevator Structure

The actuation of the elevator is achieved through a torque rod so there is no control horn that, in a side-view, goes outside the contour of the airfoil. The decision to use such device was driven by the fact that all wings/tail airfoils were designed to tightly fit within a box without any protrusion. Rotary drive systems could have been an option, but they would have added significant weight and created the need for a servo on every side of the elevator as opposed to the final design single elevator servo.

In the pre-flight-test-2 design, the movable payload and variable CG location required a trim device for the stabilator. This was achieved through a four-bar type mechanism in which one of the bars can lengthen. Thus, the tail support structure was connected to the boom through two rapid prototyped brackets, one sliding and one fixed. A pipe clamp was used to lock the sliding

bracket in place once the needed distance is set. An exploded view of this initial tail sub-assemblies can be seen in Figure 31; a fully assembled version – Figure 32.

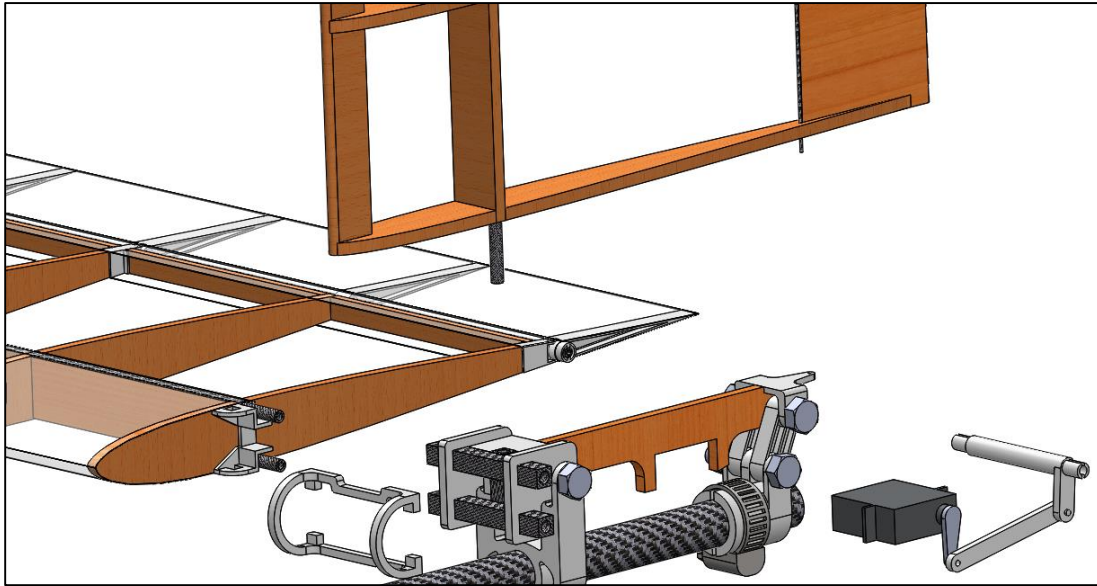


Figure 31: Initial Tail Structure (Exploded View)

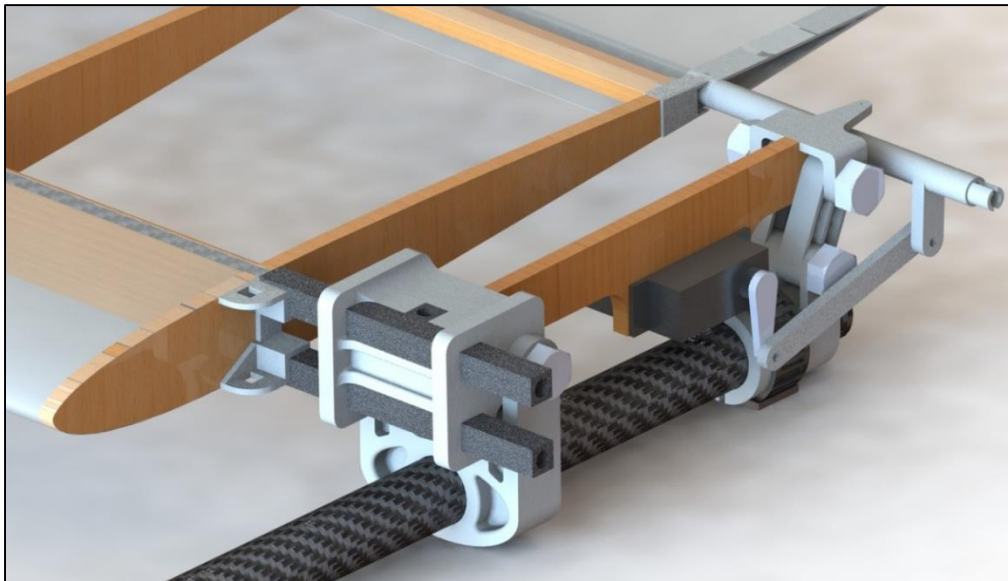


Figure 32: Tail Trim Device

Geometrical calculations correlate the distance between the brackets with the trim angle of the stabilator, based on the geometry in Figure 33. Sample correlation results can be observed in

Table 2. The device has been tuned geometrically in order to ensure a good compromise between a high enough range of available settings and a decent resolution.

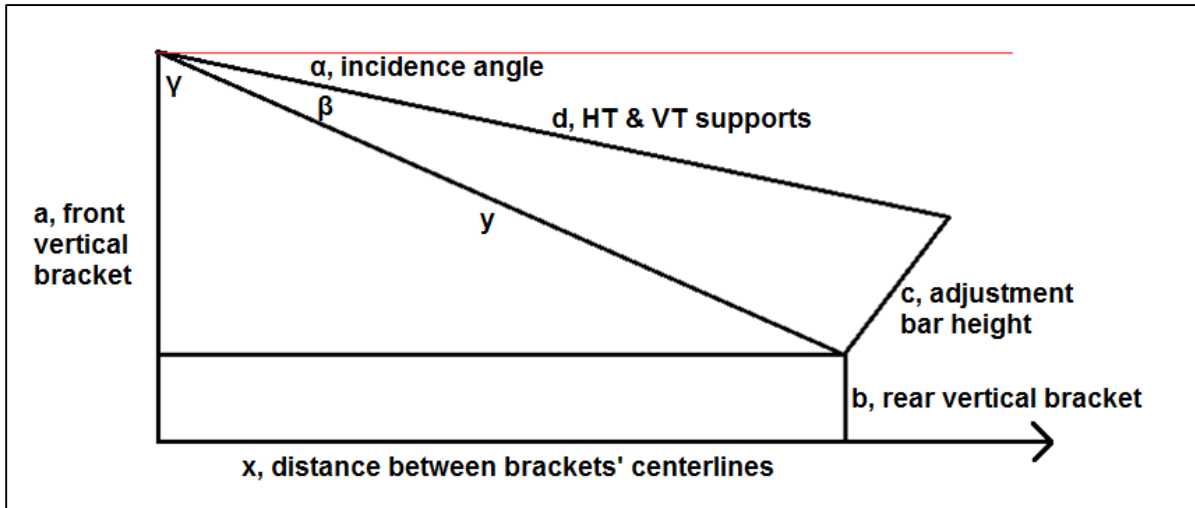


Figure 33: Tail Trim Device Geometry

Table 2: Sample Tail Trim Device Settings

Tail trim device parameters	[m]	brackets' inside distance [mm]	x [mm]	alpha [deg]	d alpha [deg]
a	0.0255	51	70.7	3.34	0.43
b	0.0122	52	71.7	2.53	0.36
c	0.0145	53	72.7	1.85	0.30
d	0.0826	54	73.7	1.27	0.25
		55	74.7	0.79	0.21
		56	75.7	0.38	0.18
		57	76.7	0.04	0.15
		58	77.7	-0.24	0.12
		59	78.7	-0.46	0.09
		60	79.7	-0.63	0.06
		61	80.7	-0.75	0.04
		62	81.7	-0.81	0.02
		63	82.7	-0.83	0.01

For the model following the first flight test, the structure that holds the horizontal and vertical stabilizers was changed to a fixed, sturdy wooden design. The attachment of the servo has been changed to a laser cut Delrin plastic to better absorb shocks and reduce weight. A slot-bar

mechanism was designed to allow actuation of the vertical stabilizer –rudder. In order to ensure an almost frictionless motion of the vertical stabilizer when aerodynamic forces are applied, two laser cut acrylic plastic elements were used. One of these element was solidly bonded to the stabilizer, one to the wooden structure. By sliding on top of each other, the carbon fiber rod is forced to remain vertical and thus motion is facilitated; thus the plates oppose all aerodynamic forces. Acrylic was chosen for the low coefficient of friction and easy manufacturability. More, one quarter-inch hole was cut into each one of these plates, as close as possible to the centers of revolution (carbon fiber rod holes), in order to solidly bond Neodymium magnets. The magnets were used to ensure that the plates are always parallel and that the vertical stabilizer does not slide out (upwards). A rendering of the entire mechanism can be seen in Figure 34.

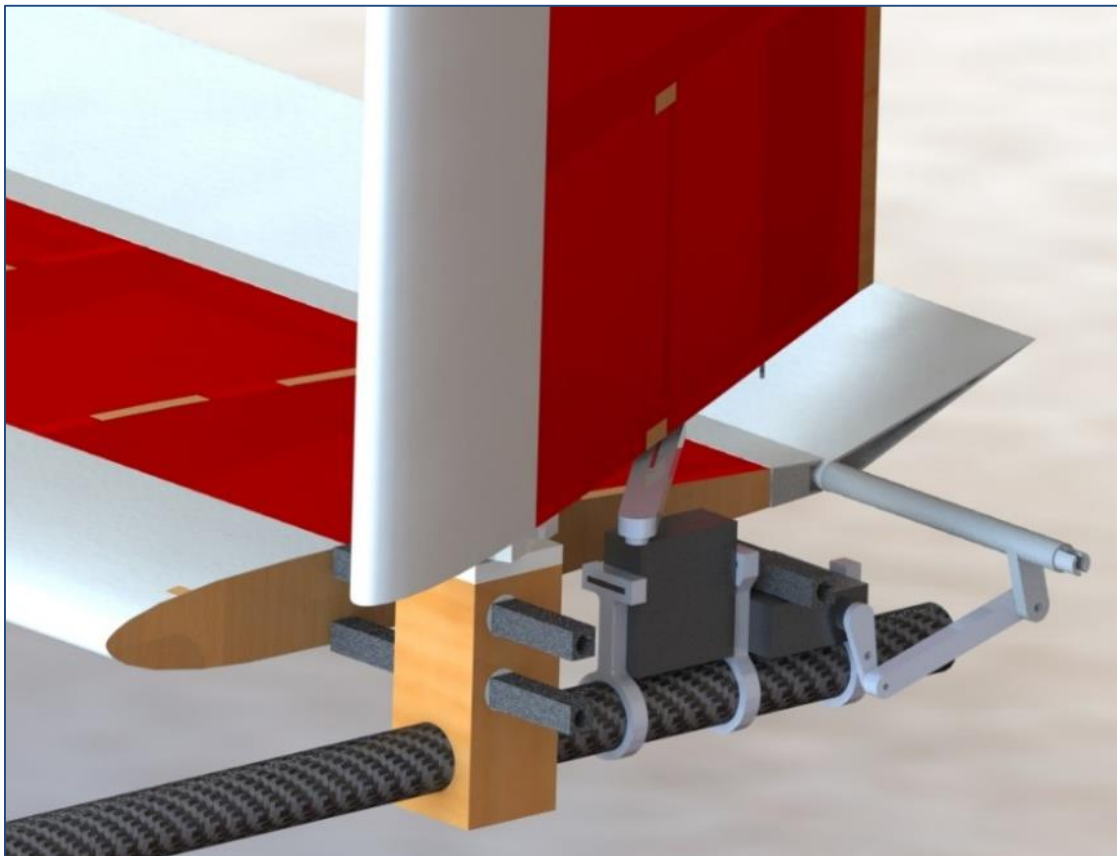


Figure 34: Final Tail Structure

The vertical stabilizer itself does not use Carbon fiber for structural purposes since the span is very small and the airfoil is symmetrical. One eight-inch carbon fiber tube is used to provide an attachment and hinge. Two very thin (0.03”) carbon fiber rods are used in order to provide an attachment point in the first, fixed design, and an actuation point in the second, moving stabilizer design. It is important to note that the thin trailing edge needed was designed to be made by extending and reinforcing the balsa ribs with a laser-cut, vertical-grain, thin (1/32”) Basswood sheet. The final internal structure of the vertical stabilizer can be seen in Figure 35.



Figure 35: Vertical Stabilizer Structure

3.0 Analysis

3.1 Aerodynamic Analysis

The theoretical lift, drag, and moment coefficient over a range of angles of attack were all obtained from XFOIL and were used to calculate the expected values of the coefficients for the full aircraft at three different speeds over the expected range for the aircraft. The average of these values at the chosen angles of attack for cruise and launch are shown in Table 3 and were used in later calculations.

Table 3: Aerodynamic Coefficients

	Chosen Cruise Parameters	Chosen Launch Parameters
Angle of Attack [degrees]	4	8
C _L wing	1.301	1.636
C _L horizontal tail	-0.274	-0.261
C _L	1.255	1.592
C _D total (except horizontal tail)	0.092	0.138
C _D tail	0.0176	0.0168
C _M wing	-0.224	-0.213

To determine the lift coefficient, the wing lift curve slope, CL_{α} , was first calculated. For a subsonic aircraft with moderate sweep angles (<30-32 degrees), a moderate aspect ratio (4-8), and a moderate taper ratio (>0.4), an estimate is given by the Polhamus formula which can be applied to both the wing and horizontal tail of an aircraft [8].

$$C_{L\alpha} = \frac{2\pi AR}{2 + \sqrt{\left\{ \left[\frac{AR^2(1-M^2)}{k^2} \left(1 + \frac{\tan^2(\Lambda_{0.5})}{(1-M^2)} \right) \right] + 4 \right\}}} \quad (5)$$

$C_{L\alpha}$ is a function of Mach number, aspect ratio and sweep angles. The parameter K is a constant which can be evaluated by the following depending on the aspect ratio for any aircraft.

$$\text{For } AR < 4 \quad k = 1 + \frac{AR(1.87 - 0.000233\Lambda_{LE})}{100} \quad (6)$$

$$\text{For } AR \geq 4 \quad k = 1 + \frac{(8.2 - 2.3\Lambda_{LE}) - AR(0.22 - 0.153\Lambda_{LE})}{100} \quad (7)$$

The lift coefficient was then calculated at each angle of attack using Equation 8.

$$C_L = C_{L\alpha}(\alpha - \alpha_{L=0}) \quad (8)$$

Due to a sudden drop in the lift coefficient of the airfoil at approximately -1.5 degrees as shown in Figure 36, the zero lift angle of attack, $\alpha_{L=0}$, is estimated using the slope of the curve at positive angles of attack. For example, using the data for 6 m/s, the actual zero lift angle of attack was -6.3 degrees but the value used was -11.9 degrees.

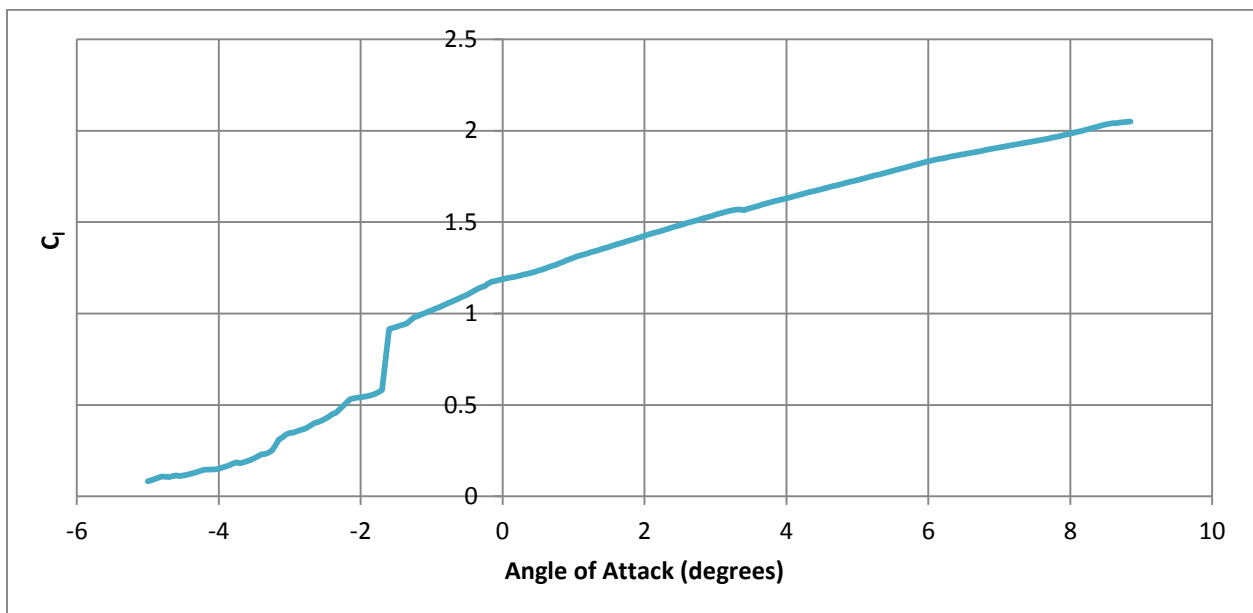


Figure 36: Airfoil Lift Coefficient

The final lift coefficient at the chosen angles of attack is the sum of the wing lift coefficient and the horizontal tail lift coefficient adjusted for the ratio of the tail planform area to the wing planform area.

The moment coefficient was calculated with Equation 9, Raymer [7].

$$C_M = C_m \frac{AR \cos^2(\Lambda)}{AR + 2 \cos(\Lambda)} \quad (9)$$

The moment coefficient was used to determine the necessary lift generated by the tail of the aircraft to stabilize the aircraft based on Equation 10.

$$L_{HT} = \frac{M_W + L_w(\bar{x}_{cg} - \bar{x}_{ac})}{l_{HT}} \quad (10)$$

$$\text{Where } M = \frac{1}{2} C_M \rho v^2 S \bar{c} \quad (11)$$

The final layout and weight of the aircraft were not known at this point so the center of gravity was estimated to be at 30% of the mean aerodynamic chord for these calculations. The tail drag coefficient corresponding to each tail lift coefficient as well as the wing drag coefficients were then calculated using Equation 12 [9].

$$C_D = C_{dmin} + K_P (C_L - C_{L_{min_drag}})^2 + K_i C_L^2 \quad (12)$$

In this equation, the minimum airfoil drag coefficient, C_{dmin} , is used in place of the parasitic drag coefficient that is often used due to the large camber of the wing. The parasitic drag coefficient represents the minimum drag coefficient of an un-cambered wing but it is not the minimum value for a cambered wing. The lift coefficient value at the same angle of attack as the minimum drag

value is $C_{l \text{ min drag}}$. The K_P term represents the contribution of pressure drag and the K_i term represents the contribution of the induced drag.

The pressure drag parameter is the slope of the linearized drag curve shown in Figure 37. Since there are several distinct line segments over the entire range of angles of attack, the segment for the range of 0 to 10 degrees was used to obtain the slope. This sufficiently covers the angles of attack the aircraft would experience during flight.

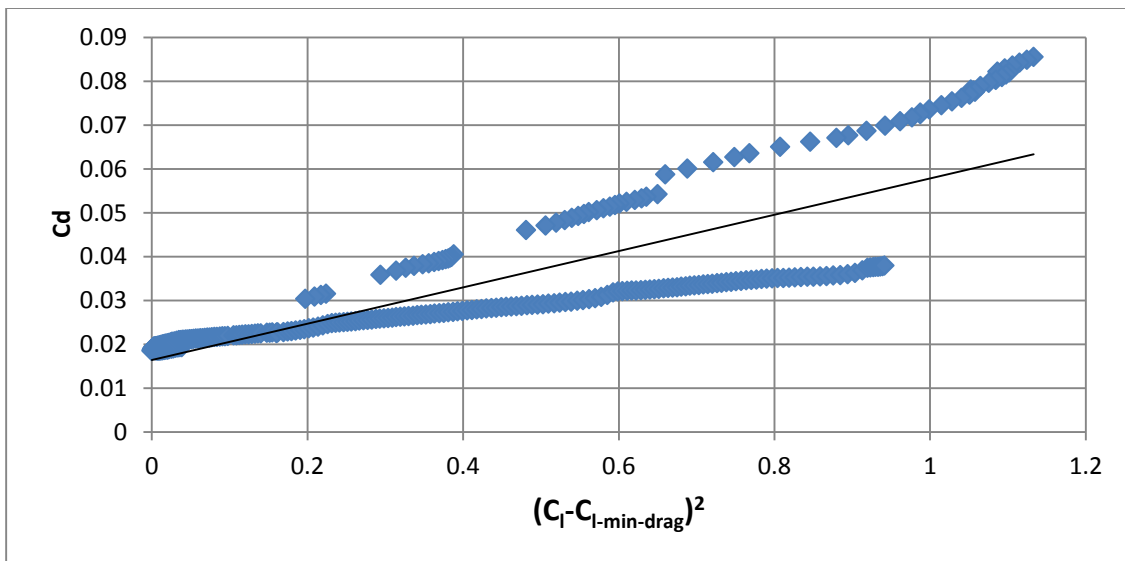


Figure 37: Linearized Drag Curve for the Calculation of K_P

The induced drag factor was calculated with Equations 13 and 14.

$$K_i = \frac{1}{\pi A R e} \quad (13)$$

$$e = 1.78(1 - 0.045AR^{0.68}) - 0.64 \quad (14)$$

The wing and horizontal tail drag coefficients were calculated with this method and the total drag coefficient was their sum, adjusting the tail value for the area ratio, added to the parasitic drag contributions of the fuselage and vertical tail calculated with the following equations.

$$C_{D0} = FF_{component} * Cf * Q * \frac{S_{wet\ component}}{S} \quad (15)$$

$$FF_{vt} = \left(1 + \frac{0.6}{\left(\frac{x}{c}\right)} \left(\frac{t}{c}\right) + 100 \left(\frac{t}{c}\right)^4 \right) * 1.34M^{0.18} (\cos\left(\Lambda_x\right))^{0.28} \quad (16)$$

$$FF_{fuselage} = 1 + \frac{60}{\left(\frac{L_f}{d_f}\right)^3} + 0.0025\left(\frac{L_f}{d_f}\right) \quad (17)$$

$$Cf = \frac{1.327}{\sqrt{RE}} \quad (18)$$

Q is a correction factor which accounts for interference drag. According to Raymer, this factor can be set to 1 for the fuselage and set to 1.03 for the vertical tail [7].

3.1.1 XFLR5 Comparison

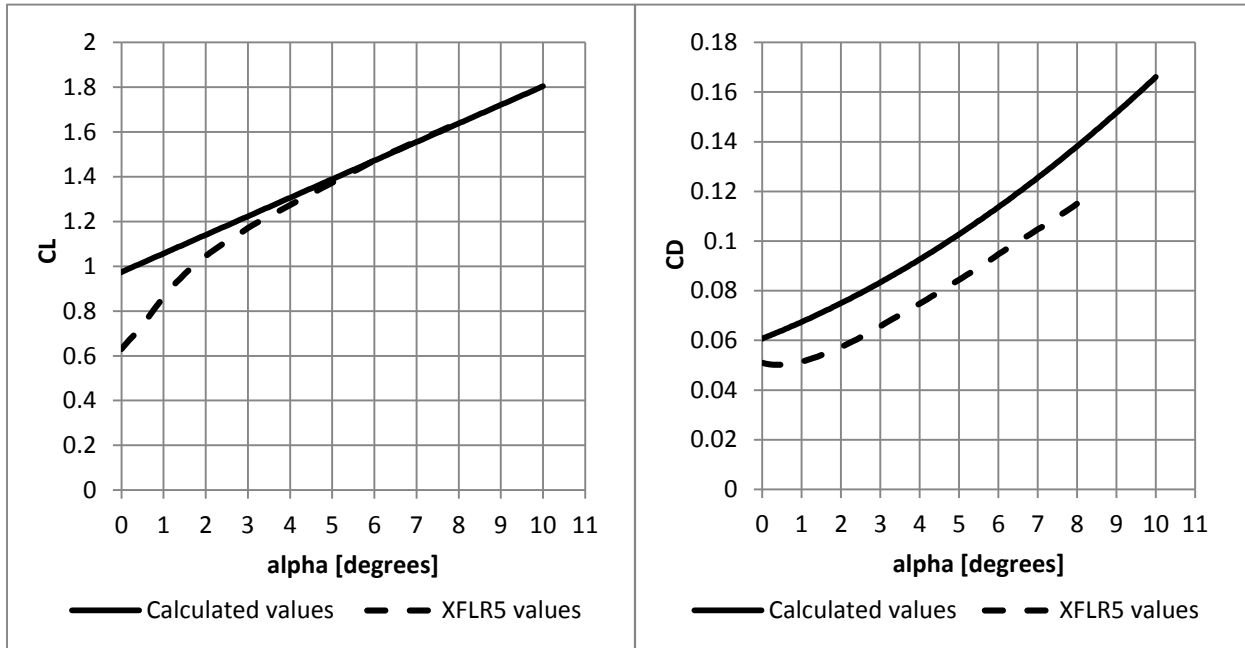


Figure 39: Comparison of Lift Coefficient Values from Calculations and XFLR5

Figure 38: Comparison of Drag Coefficient Values from Calculations and XFLR5

The theoretical aerodynamic coefficients were first verified with XFLR5 and later with wind tunnel testing. The full wing was modeled in XFLR5 and the lift and drag polars were compared to the calculated results. The corresponding pairs are shown in Figures 38-40.

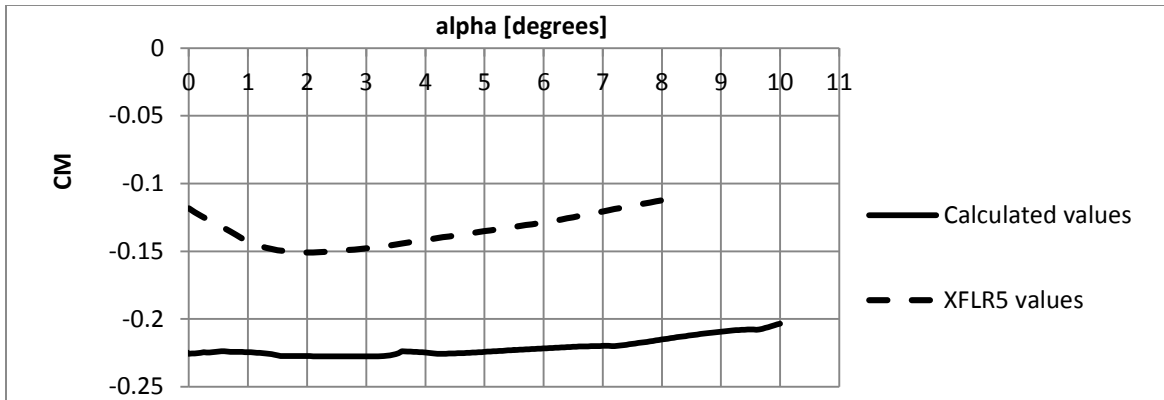


Figure 40: Comparison of Moment Coefficient Values from Calculations and XFLR5

The lift coefficient estimates differ by 40% at 0 degrees of angle of attack due to the linear approximation but converge after 6 degrees. At the chosen cruise angle of 4 degrees, there is only a 2% difference between the calculated and XFLR5 values. Therefore, the lift values were assumed to be accurate for the design process and were later verified with wind tunnel testing. The calculated drag coefficient values were all approximately 20% higher than the XFLR5 values. Since both methods are only estimates, the larger calculated values were assumed to be of sufficient accuracy for later calculations while providing for a margin of error. There is a significant difference between the moment coefficient values. However, these values were only used to estimate the contribution of the tail to the overall lift and drag. These contributions were sufficiently small that the error was negligible for the estimation of the aerodynamic coefficients. The effect of the moment generated by the wings was examined with more accuracy in the analysis of the longitudinal stability of the aircraft.

3.2 Propulsion Analysis

The propulsion system selection started from the thrust requirements at launch and cruise velocity previously determined. A table of 76 commonly available motors and the corresponding speed controllers was compiled. The parameters included were the idle current (I_0), resistances

(motor and controller), rotation speed per volt (kV), maximum current and weight. Since the batteries do not vary as much in terms of voltage, a table of common Lithium Polymer batteries based on the number of cells was used (3S and 4S). The voltage and the internal resistance were the variables. Sample tables are Table 4 and 5.

Table 4: Sample Motor Data Compilation

Motor	I₀ [Amp]	R_m [Ohm]	Kv [rpm/V]	I_{cmax} [Amp]	W [g]
AXI 2204/54 GL	0.35	0.32	1400	6	25.9
AXI 2208/20 GL	0.8	0.089	1820	12	45
AXI 1820/14 GL	1.7	0.078	860	30	151
Hacker A10-13L	0.39	0.28	1300	5	20
Hacker A30-8XL V3	2.8	0.015	1100	35	177
Hacker A30-10XL V3	1.9	0.024	900	60	177
Hyperion ZS2205 34 1587KV	0.46	0.164	1587	15	32.6
Hyperion ZS2205 38 1430KV	0.4	0.207	1430	13	32.6
Hyperion ZS3025-10	1.61	0.019	775	45	197.6
E-flite E-flite Park 180 , 2200Kv	0.3	0.91	2200	2.6	8.5
E-flite Power 25 , 870Kv	2.4	0.03	870	32	190
E-flite Six-Series BL, 2000kv	1.75	0.06	2000	26	80

Table 5: Battery Data Compilation

Battery	Voltage [V]	Resistance [Ohm]
2100mAh 3S 11.1V 20C LiPo, 13AWG EC3	11.1	0.02
3200mAh 4S 14.8V 30C LiPo, 12AWG EC3	14.8	0.025

It needs to be noted that due to conflicting available information, battery voltages were set to the values above and not to the maximum charges (determined later); the difference is significant (11.1V-12.6V) but does not seem to impact the overall choice of systems.

For the choice of propeller, the test flight data files for the propellers of the largest RC propeller manufacturer in the United States were used. The data files contain lists with the advance ratio, efficiency, thrust and power coefficients, input power, torque and thrust for ranges of rotation and air speeds. A sample fragment of a performance data file can be seen in Table 6. For this initial analysis phase, only folding propellers were chosen since they do not break on landing and they

do not pose a threat to the integrity of the costly motor. A total of nine folding propellers were used in this phase of analysis.

Table 6: Sample Propeller Performance Data File (fragment)

10x6E.dat		06/06/13					
PROP RPM = 3000							
V (mph)	J (Adv Ratio)	Pe	Ct	Cp	PWR (Hp)	Torque (In-Lbf)	Thrust (Lbf)
0.0	0.00	0.0000	0.0947	0.0565	0.000	0.029	0.030
0.3	0.03	0.0460	0.0895	0.0543	0.000	0.028	0.029
0.5	0.06	0.0905	0.0843	0.0520	0.000	0.026	0.027
0.8	0.08	0.1335	0.0792	0.0497	0.000	0.025	0.025
1.1	0.11	0.1749	0.0742	0.0473	0.000	0.024	0.024
1.3	0.14	0.2147	0.0692	0.0450	0.000	0.023	0.022
1.6	0.17	0.2530	0.0644	0.0426	0.000	0.022	0.021
16.9	0.45	0.5476	0.0398	0.0323	0.017	0.262	0.203
17.9	0.47	0.5681	0.0371	0.0309	0.016	0.251	0.189
19.0	0.50	0.5868	0.0344	0.0294	0.015	0.238	0.175
20.0	0.53	0.6038	0.0316	0.0276	0.014	0.224	0.161
21.1	0.56	0.6184	0.0287	0.0258	0.013	0.210	0.146
22.1	0.58	0.6295	0.0257	0.0239	0.012	0.194	0.131
23.2	0.61	0.6365	0.0227	0.0219	0.011	0.177	0.116
24.3	0.64	0.6375	0.0196	0.0197	0.010	0.160	0.100

A Matlab script (Appendix A) was written in order to calculate the thrust delivered at flight and take-off velocity, power usage, system efficiency and weight for every combination. The first challenge consisted in reading and parsing the data from the performance files; for this, a regular-expression (RegExp) approach was used. Next, the current, voltage, torque, rpm and power output of the motor needed to be related with the motor parameters (Excel inputs). The four fundamental formulas are represented by Equations 19-22 [10].

$$I_m = (V_m - N/K_v)/R_m \quad (19)$$

$$Q_m = (I_m - I_0) K_t \quad (20)$$

$$K_t = 60/(2 \pi K_v) \quad (21)$$

$$P_{m-out} = I_m V_b - I_m^2 R_m - I_0 N/K_v \quad (22)$$

Where R_c is the combined resistance of the motor and controller (ESC).

Following, Equations 23 and 24 [10] relate the power absorbed by the propeller and the thrust generated with the rotation speed of the motor.

$$P_{p-in} = C_p \rho (N/60)^3 D^5 \quad (23)$$

$$T = C_t \rho (N/60)^2 D^4 \quad (24)$$

The two sets of equations are relate through the power transmitted from the motor to the propeller. Setting the two values equal, an equation which yields the rpm can be written:

$$\frac{N(N_0-N)}{(K_v^2 R_c)} = C_p \rho (N/60)^3 D^5 \quad (25)$$

Where

$$N_0 = K_v(V_b - I_0 R_c) \quad (26)$$

After the rpm is found, thrust, voltages, currents and efficiencies can be calculated. For the total efficiency, the propeller and the motor efficiencies are multiplied. The motor efficiency is the ratio between mechanical output power and electrical input power, as given by Equation 27. In a similar manner, Equation 28 gives the propeller efficiency by using the thrust and velocity – power output – and the mechanical power input.

$$\eta_m = (1 - I_0/I_m)(1 - I_m R_m/V_m) \quad (27)$$

$$\eta_p = T \frac{V}{P} = J C_p/C_t \quad (28)$$

Where the dimensionless advance ratio J is given by Equation 29.

$$J = V/(D N/60) \quad (29)$$

Using the formulas above, the script iterates over each combination of motor-battery-propeller. Using the performance data files, interpolations are used to refine the curves that have steps of 1000rpm and 0.1 mph. Pairs of rpm values and motor output (propeller input) power values

from the electrical system are matched against similar pairs calculated from the performance data files. This way, the script determines the rpm that each combination will run at for the required flight speeds (take-off and cruise) and calculates the other system parameters.

The series of results from all possible combinations are sorted by thrust and efficiency. Filters are added to ensure reasonable total efficiencies and thrust values larger at least 50% larger than those required for both take-off and cruise. The continuous current required and the electrical power input are compared with the maximum values supported by the motor, as given by the manufacturer. The refined were filtered by efficiency and thrust. The top ten choices were evaluated to find the optimal combination between thrust, efficiency and weight. This last part of the decision process was done without a computer since it involves too many parameters. A compromise has been found for the Hacker A20-12XL – 10x6F motor-propeller combination. For its very low size, this system delivers much more thrust than similarly weighed combinations, for almost the same efficiency. The table containing this interim set of results can be seen summarized in Table 6; highlighted in yellow and green are the backup and final combinations of commercially available components.

Table 7: Interim Propulsion Analysis Results Sample

motor	N [RPM]	Im [A]	T [N]	eta_tot	W [g]
E-flite Park 480, 910kv, Prop10x6F	8700	15.40	5.57	0.34	87
Hyperion ZS3014-12, Prop9x5F	11800	17.33	6.04	0.32	126.3
Hyperion ZS3020-10, Prop10x6F	9500	20.42	6.90	0.32	161.7
E-flite Power 25 , 870Kv, Prop10x6F	8900	17.40	5.89	0.31	190
AXI 1820/12 GL, Prop10x6F	9400	20.32	6.73	0.31	151
Hyperion ZS3020-08, Prop9x5F	11900	18.65	6.17	0.31	161.7
Hacker A30-10XL V3, Prop10x6F	9200	19.95	6.39	0.30	177
Hacker A20-12XL, Prop10x6F	9200	20.00	6.39	0.30	78
E-flite Power 15 , 950Kv, Prop10x6F	9500	22.00	6.90	0.29	152

For the chosen configuration, a range of folding and solid propellers close to the calculated optimum were also acquired for wind tunnel testing. Tunnel testing revealed thrust values 10-15% higher than calculated. The trends for the change of propeller pitch, thickness and diameter observed theoretically were confirmed by the tunnel testing. Overall, the available thrust at the design cruise velocity is 72% more than the required value for a solid propeller and 50% for a folding propeller.

Particular care had to be given to the selection of the battery. Tests showed that even with high end hobby batteries, the voltage drop for the specified maximum continuous current can considerably affect propulsion performance. The solution was to choose a battery rated for over three times the current value needed. The battery capacity was also chosen to be much higher than what is needed on a single lap since the battery voltage drops as the stored energy decreases.

The final configuration for a fixed propeller weighs 230g, delivers 7.2N of thrust at 8.2 m/s using a 10" diameter, 5" pitch propeller with a 250W, brushless motor and a medium charged 3S 1100mAh battery. The overall efficiency is only 30% due to the very low speed, not typical for RC propellers.

3.3 Structural Analysis

Analysis was performed for the bending and shear strength of the spar and the carbon fiber rods joining the wing sections using Engineering Sandwich Beam Theory [11] and Timoshenko Beam Theory. A load factor of 2.5 was assumed in order to ensure survivability during landing. The properties of the Carbon fiber elements were provided by the manufacturer and the Balsa wood properties were estimated based on measured densities using interpolation from a large compilation of sources. Iterations based on the available materials were performed until an overall factor of safety larger than 3 was achieved for the minimum spar weight.

For Balsa wood, a sample interpolated table of values for the compression/shear moduli and for the maximum compression stress as functions of densities can be seen in Table 8. The spar web materials, critical to the sandwich beam type structure, have been weighed such that the highest densities and thus the strongest materials were used towards the root section of the spar. The table below highlights the average values used for calculations.

Table 8: Density Interpolated Balsa Strength Coefficients

	density [lb/ft³]	density [kg/m³]	E comp L [MPa]	sigma comp L max [MPa]	G LT/LR [MPa]
Estimated Values	5	80.09	1387.33	5.17	86.08
	5.2	83.30	1523.39	5.47	91.18
	5.4	86.50	1658.03	5.77	96.22
	5.6	89.70	1791.25	6.07	101.21
	5.8	92.91	1923.06	6.38	106.15
	6	96.11	2053.45	6.68	111.03
	6.2	99.31	2182.42	6.98	115.86
	6.4	102.52	2309.97	7.29	120.63
	6.6	105.72	2436.10	7.59	125.35
	6.8	108.93	2560.82	7.90	130.02
	7	112.13	2684.12	8.21	134.63
	7.2	115.33	2806.00	8.51	139.19
	7.4	118.54	2926.46	8.82	143.69
	7.6	121.74	3045.50	9.13	148.15
	7.8	124.94	3163.13	9.44	152.54
	8	128.15	3279.33	9.75	156.89
	8.2	131.35	3394.12	10.07	161.18
	8.4	134.56	3507.49	10.38	165.41
8.6	137.76	3619.44	10.70	169.59	

The calculation started with an Excel file that uses geometric and aerodynamic inputs. First, the wing span is discretized into 0.1” strips and the chord length is calculated for each strip; then the differential shear force is calculated directly from the lift formula (Equation 30) and summed to obtain the shear force at every point. The bending moment is integrated from the differential

shear results (Equation 31), and the pitching moment is integrated from the differential moments (Equations 32, 33).

$$dQ = \frac{1}{2} \rho V^2 (c dz) C_l \quad (30)$$

$$M_b(z_1) = \sum_0^{z_1} Q(z) (z - z_1) \quad (31)$$

$$dM_p = \frac{1}{2} \rho V^2 (c dz) C_m \quad (32)$$

$$M_p(z_1) = \sum_0^{z_1} (dM_p(z)) \quad (33)$$

For the flexural calculations, the spar height was approximated to be 90% of the wing thickness at any point. Based on the provided thickness of the tapered and non-tapered carbon fiber spar-caps, the thickness of the spar cap at every point was interpolated. The flexural stiffness at every point was calculated using Equation 34 [11], the dimensions being considered as in Figure 41.

$$D = \frac{2}{3} E_f f^3 + \frac{2}{3} E_c h^3 + 2E_f f h (f + h) \quad (34)$$

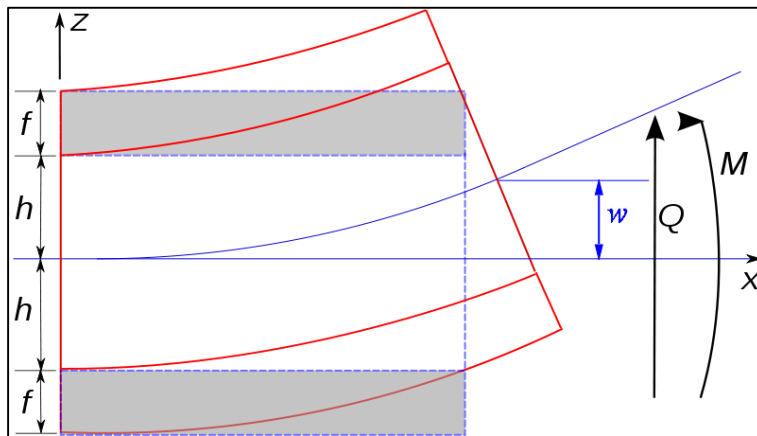


Figure 41: Engineering Sandwich Beam Notations
 [http://en.wikipedia.org/wiki/Sandwich_theory#Engineering_sandwich_beam_theory]

The compression and shear stresses in the spar-caps (faces) and the spar-webs (core) at every point along the span were calculated with Equations 35-38. For all equations, the variable z was set to half of the spar height at that point since the equations are being used to calculate the maximum stress values which occur near the surface of the sandwich beam.

$$\sigma_f = \frac{z E_f M_b(x)}{D} \quad (35)$$

$$\sigma_c = \frac{z E_c M_b(x)}{D} \quad (36)$$

$$\tau_f = \frac{Q(x) E_f}{2D} [(h + f)^2 - z^2] \quad (37)$$

$$\tau_c = \frac{Q(x)}{2D} [E_c(h^2 - z^2) + E_f f(f + 2h)] \quad (38)$$

The plotted results can be seen in Figures 42 and 43; the discontinuous shape is due to the different types of commercially available carbon fiber strips used as spar caps and to the narrower spar of the outer wing section. The shear stresses are not presented since they are much lower relative to their maximum values when compared to the compression/tension stresses.

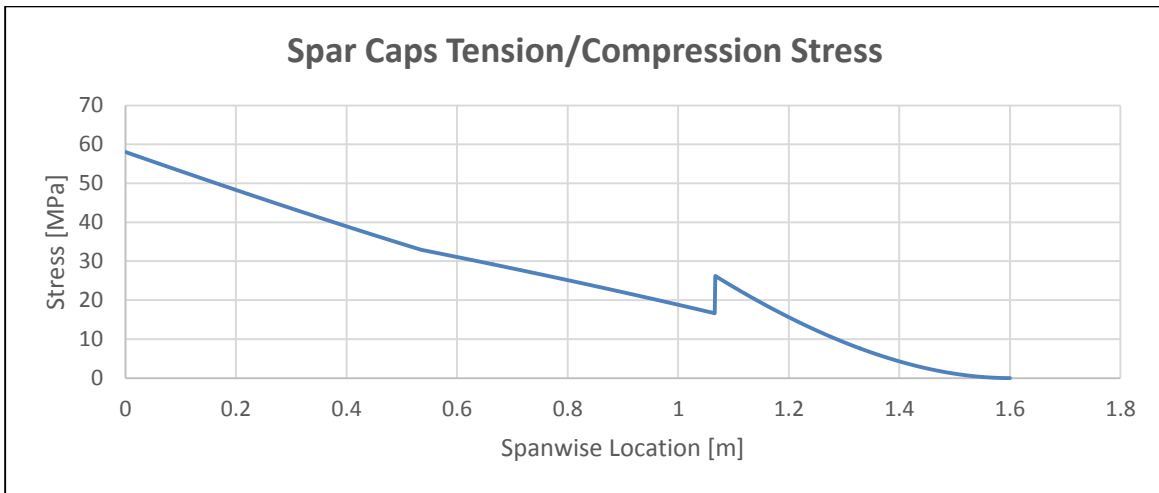


Figure 42: Spar Cap Tension/Compression Stress Diagram

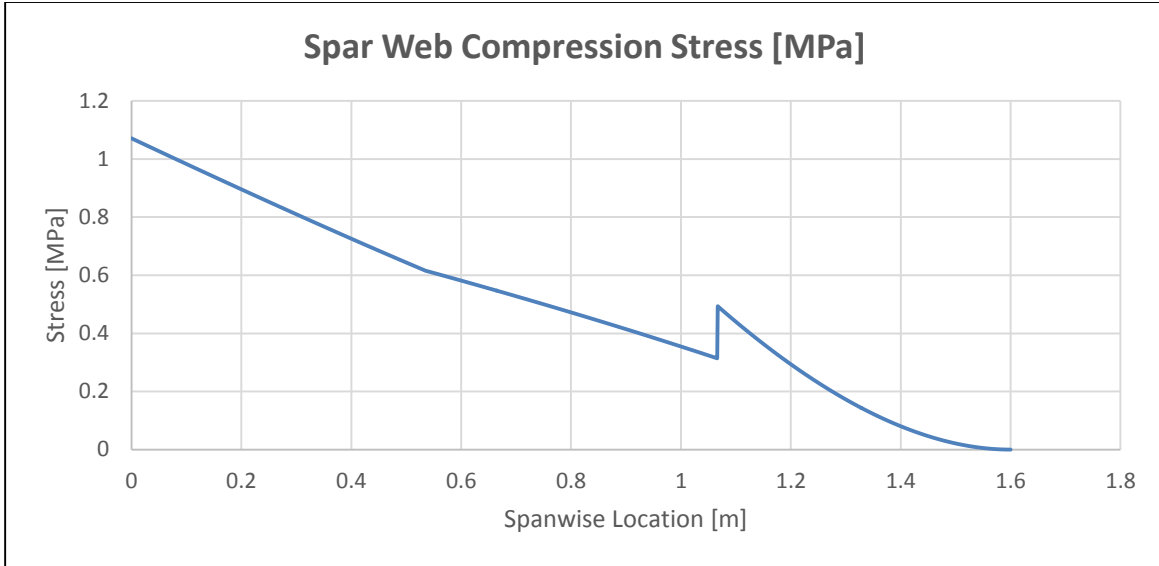


Figure 43: Spar Web Compression Stress Diagram

For the torsional calculations, due to the very complex structure, only the spar was analyzed. Obviously, the PET D-box leading edge will further improve these values, increasing the torsional stiffness. The torsional stiffness at every point was calculated using Equation 39, where the k_1 coefficient is interpolated from Table 9, as seen in Figures 44 and 45.

$$J = k_1 b h^3 \quad (39)$$

Table 9: Spar Torsional Parameters Estimation

Torsional parameter for rectangular cross section								
b/h	1	1.5	2	2.5	3	4	6	10
k1	0.141	0.196	0.229	0.249	0.263	0.281	0.299	0.312
k2	0.208	0.231	0.246	0.256	0.267	0.282	0.299	0.312

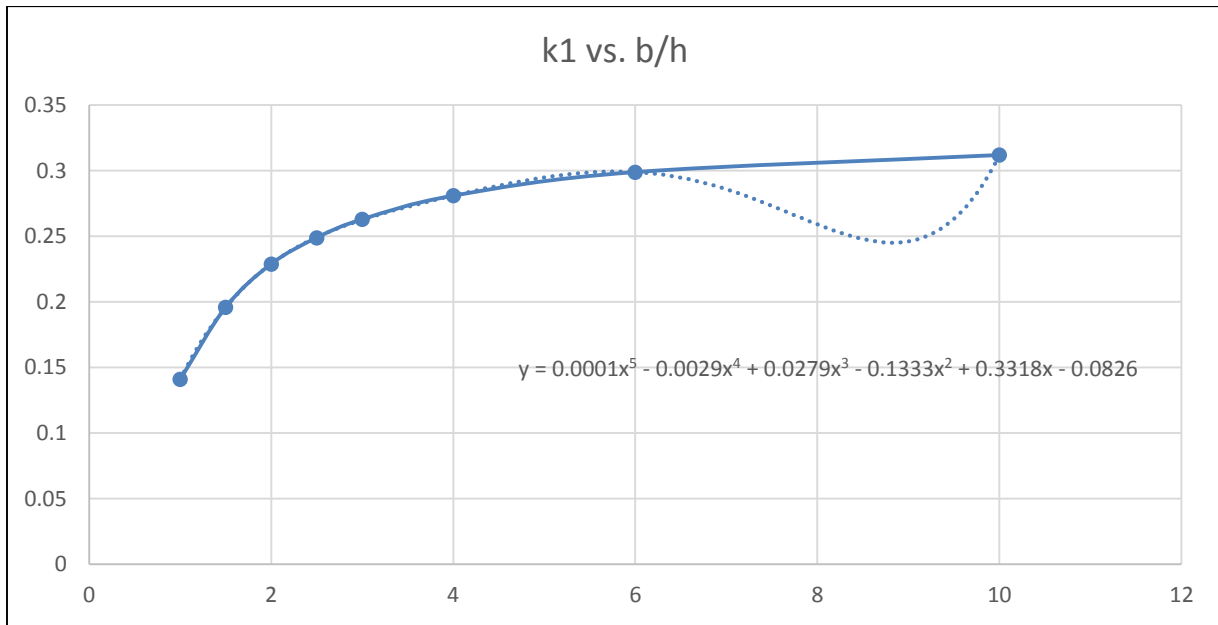


Figure 44: Torsional Parameter k_1 Interpolation

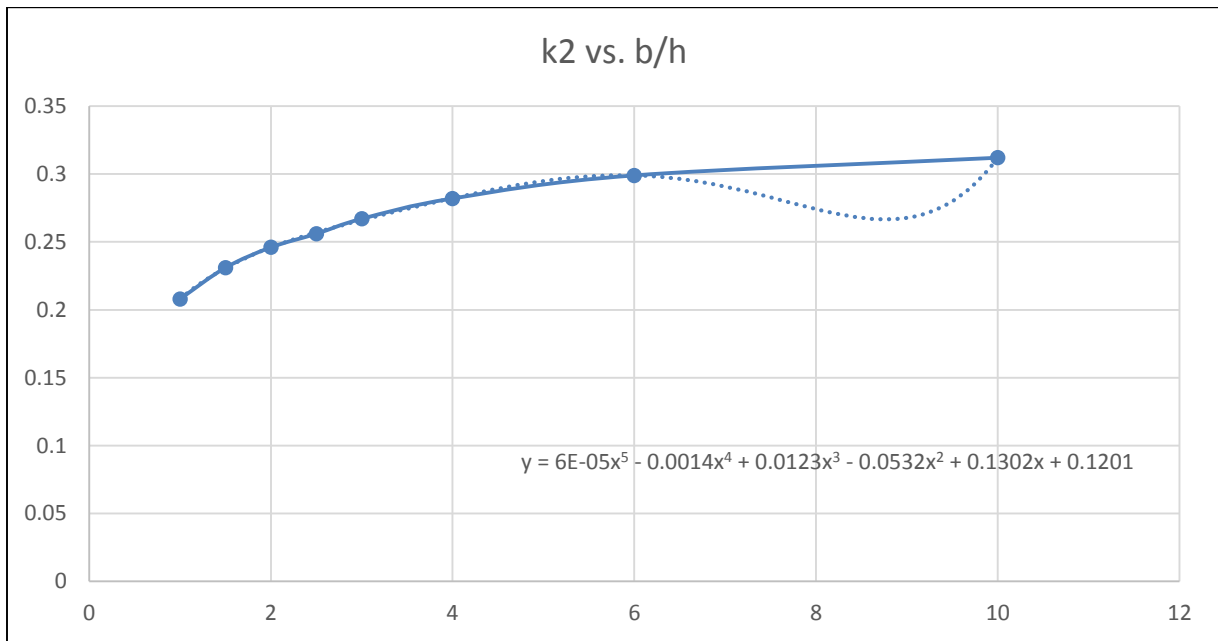


Figure 45: Torsional Parameter k_2 Interpolation

The angle of twist for each differential span-wise section was calculated with Equations 40 and 41 and then integrated to obtain the angle of twist at every station. The shear stress due to twist was calculated at every station with Equation 42 and can be observed in Figure 46.

$$\frac{T L}{\theta} = G_c J \quad (40)$$

$$d\theta(z) = \frac{M_p(z)}{\left(\frac{T L}{\theta}\right)} \quad (41)$$

$$\tau_{max-twist}(z) = \frac{M_p(z)}{8 k_2 h b^2} \quad (42)$$

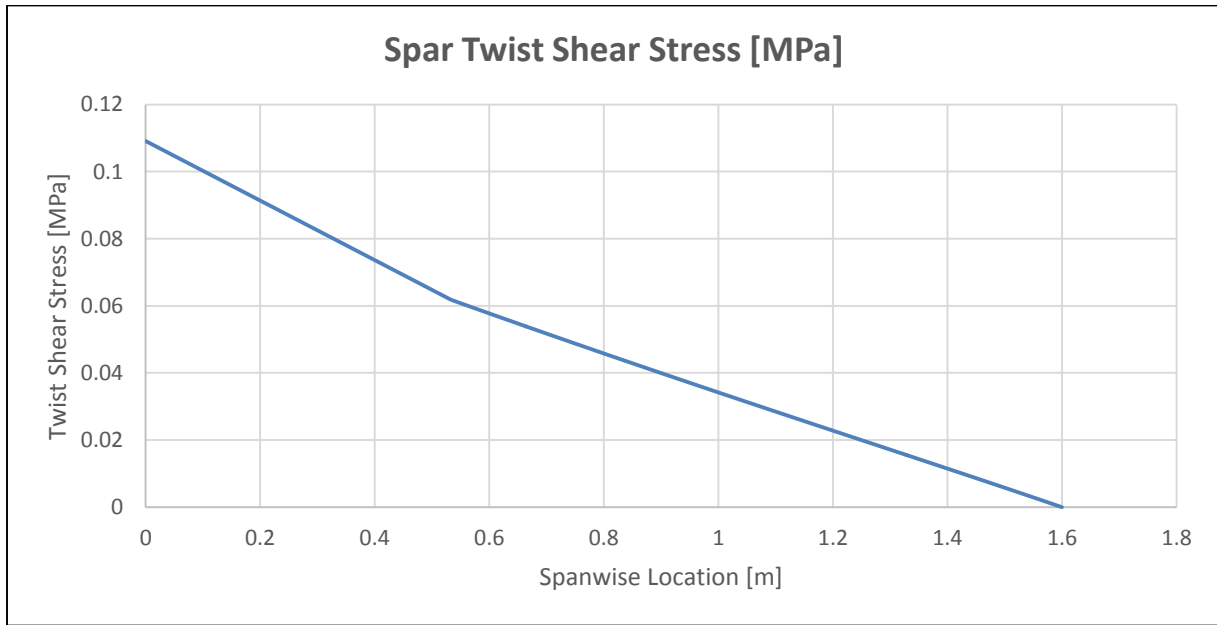


Figure 46: Spar Web Twist Shear Stress Diagram

To ensure that the carbon fiber rods joining adjacent wing sections are adequately sized, basic Timoshenko Beam Theory was applied for every pair of rods; the value of the shear force and bending moment used is taken from the interface point between the wing sections. For every case, the inputs were the rod diameter and the overall height of the assembly and the outputs were the flexural rigidity of, and the maximum bending stress in the assembly (Equations 43, 44).

$$D = 2 E \pi \left[\frac{d^2(h-d)^2}{16} + \frac{d^4}{64} \right] \quad (43)$$

$$\sigma_{max} = \frac{M_b E h}{2 D} \quad (44)$$

The factors of safety were calculated by dividing the maximum stress the material can withstand by the maximum stress the system can provide and by the load factor of 2.5. The resultant number can be seen in Table 10.

Table 10: Wing Structure Factors of Safety

	Section A			Section B			Section C		
	sigma_f max [MPa]	sigma_c max [MPa]	sigma joiner max [MPa]	sigma_f max [MPa]	sigma_c max [MPa]	sigma joiner max [MPa]	sigma_f max [MPa]	sigma_c max [MPa]	sigma joiner max [MPa]
Max Stress	58.03	1.07	21.00	32.96	0.62	3.41	26.22	0.49	1.59
UTS	1600	8.2054	2500	1600	8.2054	2210	1600	8.2054	2210
FOS	11.03	3.06	47.61	19.42	5.33	258.95	24.41	6.65	556.46

As it can be observed, the lowest factors of safety (highlighted above) come from the compression of the Balsa spar webs; increasing the thickness or modulus of the carbon fiber spar caps can improve the entire structure. It is interesting to observe that if the wood is used in the wrong grain orientation – horizontal and not vertical – this set of formulas sees factors of safety increasing by orders of magnitude. A “sanity check” can spur the check-up of the assumptions made for these calculations, and obviously, they do not stand. Since horizontal grain Balsa wood is roughly an order of magnitude weaker in compression and shear, the assumption that the core can keep the spar caps apart at a constant distance without buckling fails.

3.4 Stability Analysis

Most renowned aircraft companies test for the stability of their respective product through a combination of computer aided programs and expensive wind-tunnel tests. Unfortunately, this technology was not available to us, so we approximated the stability of the aircraft through numerical methods outlined in Marcello Napolitano's *Aircraft Dynamics: From Modeling to Simulation* [8], the United States Air Force Stability and Control DATCOM [12] and computational fluid dynamic models. Testing for the stability of the aircraft is necessary to determine if the pilot will be able to control and maneuver the aircraft after the flight path has been disrupted by a wind gust or pilot induced inputs.

Aircraft stability is divided into two different categories: static stability and dynamic stability. Static stability refers to the ability of the aircraft to return to its original state (equilibrium) after a pilot induced maneuver or environmental disturbance in the longitudinal, lateral, or both directions. Dynamic stability refers to the dynamic oscillatory motion of the aircraft following a disturbance, and to the ability to return to its original state or a different steady state after a certain period of time; the less time it takes, the larger the damping forces. Dynamic stability requires static stability, but an aircraft could be statically stable without being dynamically stable.

In order to test the stability of the aircraft, we first found the stability derivatives. The stability derivatives are coefficients that characterize the linearized equations of motion for an aircraft. The stability derivatives in Napolitano's numerical methods were all derived from geometric parameters of the aircraft. A MATLAB script (Appendix C) was created in order to conduct the analysis at different flight conditions with geometric alterations and to effectively visualize the aircraft's response.

3.4.1 Modeling the longitudinal steady state aerodynamic forces and moments

In order to begin the evaluation of the dynamic behavior of the aircraft, the equations of motion were analyzed. This includes the equations for the conservation of angular momentum and the conservation of linear momentum:

$$\begin{aligned}
 m(\dot{U} + QW - RV) &= -mg \sin \Theta + (F_{Ax} + F_{Tx}) \\
 m(\dot{V} + UR - PW) &= mg \cos \Theta \sin \Phi + (F_{Ay} + F_{Ty}) \\
 m(\dot{W} + PV - QU) &= mg \cos \Theta \cos \Phi + (F_{Az} + F_{Tz}) \\
 \dot{P}I_{xx} - \dot{R}I_{xz} - PQI_{xz} + RQ(I_{zz} - I_{yy}) &= L_A + L_T \\
 \dot{Q}I_{yy} + PR(I_{xx} - I_{zz}) + (P^2 - R^2)I_{xz} &= M_A + M_T \\
 \dot{R}I_{zz} - \dot{P}I_{xz} + PQ(I_{yy} - I_{xx}) + QR I_{xz} &= N_A + N_T
 \end{aligned}$$

Figure 47: Conservation of Linear and Angular Momentum (Napolitano, 10)[8]

The stability axis follows what is already outlined in Napolitano’s textbook [8]. As shown in Figure 48, X represents the forward longitudinal direction, Z is in the direction of gravity and lift, and a pitching moment occurs in the clockwise direction along the aircraft’s center of gravity.

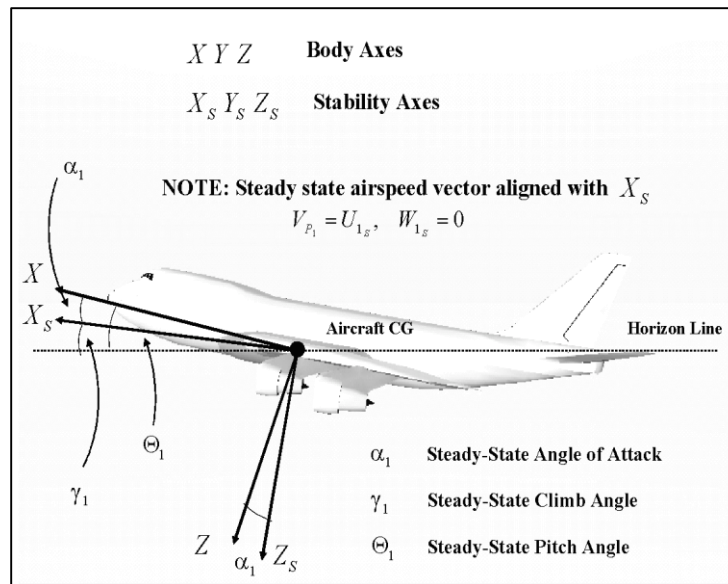


Figure 48: Aircraft Body and Stability Axis (Napolitano, 80)[8]

Two control surfaces (stabilator and elevators) are included in the analysis, which are represented in Figure 49. These contribute to the drag, lift and pitching moment stability derivatives in the longitudinal direction.

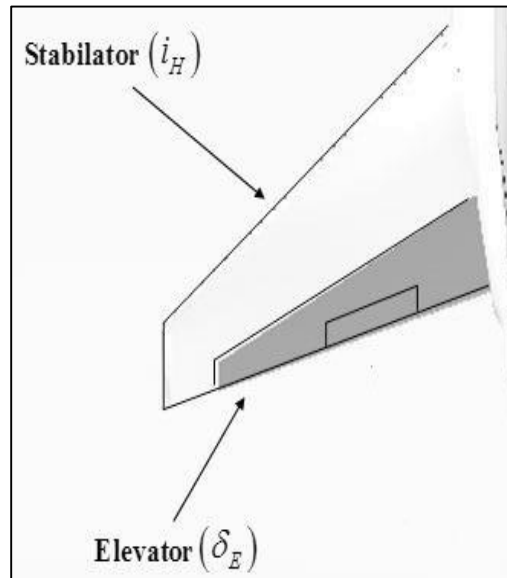


Figure 49: Stabilator and Elevator Longitudinal Control Surfaces (Napolitano, 80)[8]

3.4.1.1 Modeling the Drag stability derivatives

The drag stability derivatives consist of the evaluation of the drag coefficient (C_d) with respect to angles of attack (α), elevator deflections (δ_e), and horizontal tail stabilizer deflections (i_H). For most aircraft with conventional tails, the drag coefficient with respect to both elevator and horizontal stabilizer deflections are negligible due to limited flow exposure of the surfaces. C_{D1} , however, is not negligible. This drag coefficient integrates both the fuselage and the wing, and was found using the following conceptual expression.

$$C_{D_1} = \bar{C}_{D_0} + \frac{C_L^2}{\pi AR e} \quad (45)$$

In this equation C_{D0} is the parasitic drag coefficient, e is the Oswald efficiency factor, AR is the wings aspect ratio, and C_L is the lift coefficient. This method is not very accurate; therefore

wing tunnel testing was necessary to identify this coefficient for our particular aircraft. A summary of all the equations that were used to evaluate the drag stability derivatives can be found on Appendix B.

3.4.1.2 Modeling the Lift stability derivatives

The lift stability derivatives are also functions of angle of attack and elevator/stabilizer deflections. However, the control surfaces are more exposed in the vertical direction (Z -axis) when deflected; hence, the lift stability derivatives are heavily influenced by the elevator and stabilator. These stability derivatives also have contributions from various sections of the aircraft including the fuselage, the wings and horizontal tail.

These derivatives require the wing lift curve slope that was previously calculated in the aerodynamic analysis. Due to the size of the wings and horizontal tail, it is also very important to model the downwash effect of the wings on the horizontal tail. The downwash effect consists of vortices generated by flow on the wing that eventually affect the horizontal tail by changing the incoming flow characteristics. The downwash effect was mathematically approximated using the following formula.

$$\frac{d\varepsilon}{d\alpha} |_{Mach} = 4.44(K_{AR}K_{\lambda}K_{mr}\sqrt{\cos(\Lambda_{0.25})})^{1.19}\sqrt{1 - Mach^2} \quad (46)$$

In this formula, K_{ar} , K_{λ} and K_{mr} are coefficients that were interpolated from data in Napolitano's textbook [8]. The first two coefficients are dependent on aspect ratio and taper ratio and can be approximated using Figure 50.

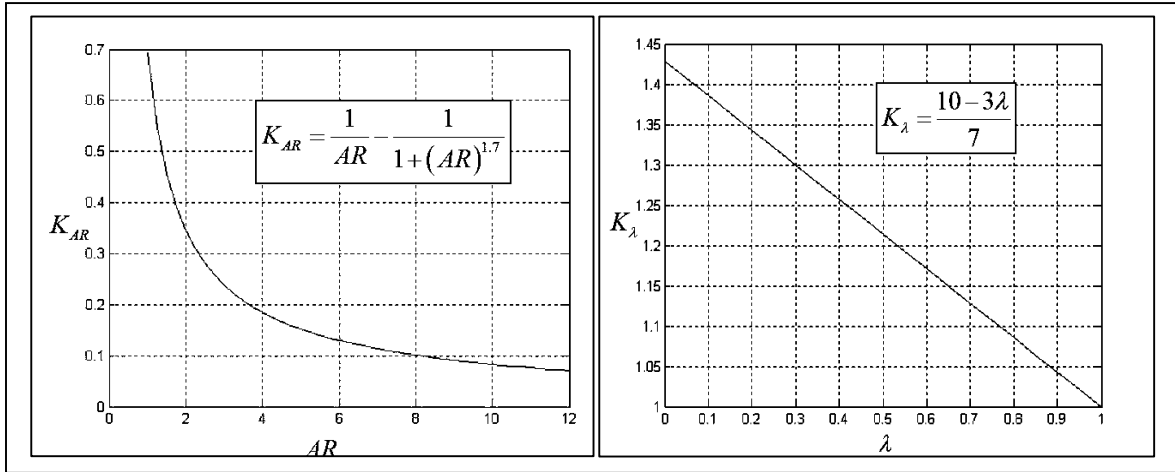


Figure 50: Geometric Coefficients for Downwash (Napolitano, 51)[8]

In order to obtain the third coefficient, values for r and m were found using the geometric sections shown in Figure 51.

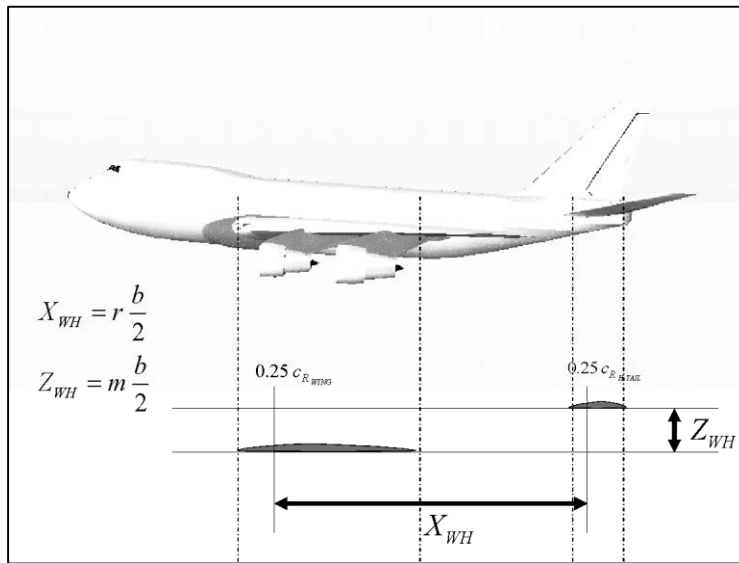


Figure 51: Wing-Tail distances in the longitudinal & vertical directions (Napolitano, 50)[8]

As shown in Figure 51, the value for m is dependent on the distance between the bottom of the wing and the bottom of the horizontal tail. The value for r was found using the distance

between the quarter-chord of the wing to the quarter cord of the horizontal tail. With these values, the last coefficient was estimated from Figure 52.

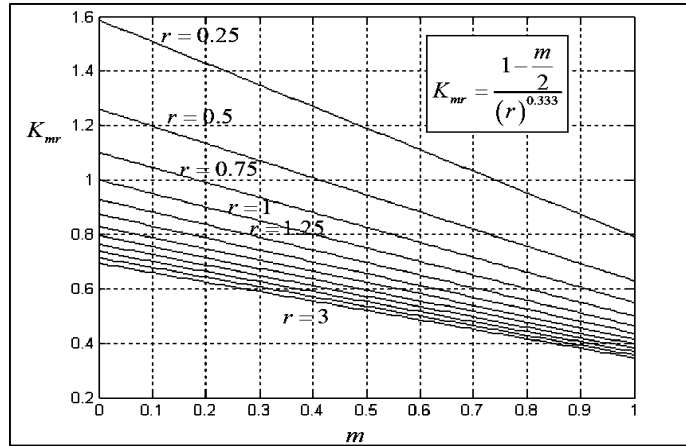


Figure 52: Geometric Coefficients for Downwash (Napolitano, 51)[8]

The efficiency of the elevator was also evaluated using empirical data. The efficiency of the elevator is a unit-less value that depends on the ratio between the mean aerodynamic center of the elevator with respect to the mean aerodynamic center of the horizontal tail. Once this ratio was found, the empirical data provided by Napolitano in Figure 53 was used to find the elevator efficiency [8].

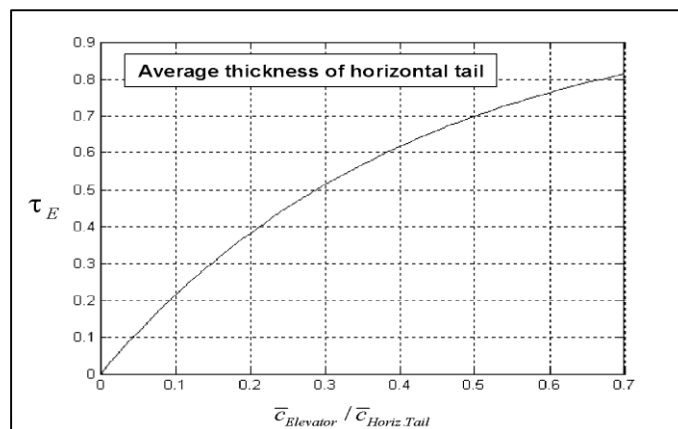


Figure 53: Typical Range for elevator surface effectiveness (Napolitano, 52)[8]

A summary of the complete equations for modeling the lift stability derivatives can be found in Appendix B.

3.4.1.3 Modeling the pitching moment stability derivatives

A third major set of stability derivatives in the longitudinal direction are the pitching moment stability derivatives. These derivatives depend on the aircraft angle of attack and elevator and stabilator deflections, just like those for lift stability derivatives. C_{m_α} , for example, is a critical aerodynamic coefficient in the longitudinal direction. This coefficient depends on both the values for the lift coefficient with respect to the angle of attack of the wing and body as well as the lift coefficient stability derivative of the horizontal tail. It also takes into account the physical behavior of the downwash effect on the horizontal tail. It is important to note that, for aircraft with conventional configuration flying at subsonic Mach number, the range of C_{m_α} is typically 4 - 5.5 (Napolitano, 89)[8]. Other important parameters to take into account when determining pitching moment stability derivatives are the differences between the aerodynamic center and the aircraft's center of gravity. For a complete set of equations to determine the pitching moment stability derivatives refer to Appendix B.

3.4.1.4 Modeling the Aircraft Aerodynamic Center

A parameter important in determining the value of the stability derivatives is the aircraft's aerodynamic center. The aerodynamic center is defined as “the point with respect to which the pitching moment for the entire aircraft does not change with variations in the longitudinal angle of attack” (Napolitano, 89)[8]. In order to determine the total aircraft aerodynamic center shown in Figure 54, it is first important to understand what the aerodynamic center is, with respect to the wing, wing body, and horizontal tail.

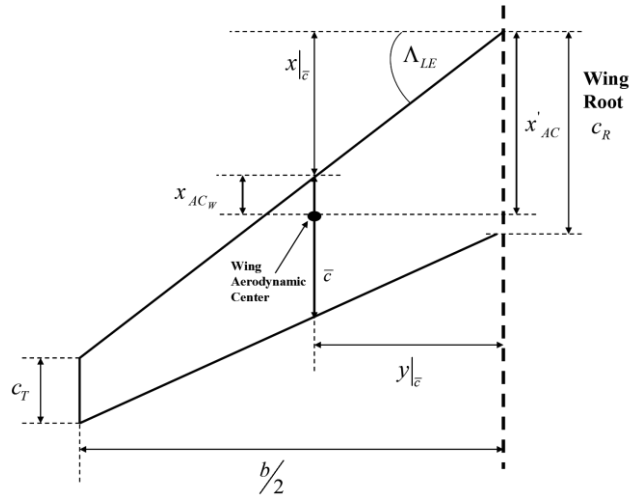


Figure 54: Location of the Wing Aerodynamic Center (Napolitano, 53)[8]

$$\bar{X}_{ACW} = K1 \left(\frac{x'_{AC}}{c_R} - K2 \right) \quad (47)$$

Equation 47 is useful in determining the aerodynamic center with respect to the wing. The coefficients K1 and K2 can be found by interpolating the graphs found in Napolitano's textbook, Figure 2.28 and Figure 2.29, respectively on pages 54 and 55 [8]. The K1 coefficient is dependent on the taper ratio of the wing while the K2 coefficient is dependent on the leading edge sweep angle. The values for the third parameter x_{AC}'/c_R can be found by interpolating curves in Figure 2.27 [8]. This parameter is tabulated as a function of taper ratio, aspect ratio, leading edge sweep angle and the Mach number. This equation gives the aerodynamic center of the wing as a fraction of the mean aerodynamic cord. The Munk Theory is a numerical approximation that can help determine the aerodynamic center as a fraction of the mean aerodynamic chord of the wing and fuselage of the aircraft. (Napolitano, 66)[8]. Since the fuselage was extremely narrow when compared to the span of the wing, the X_{AC} (wing+body) was assumed to be zero. Finally, the aerodynamic center of the entire aircraft was found using the following equation.

$$\bar{X}_{AC} = \frac{\bar{X}_{ACWB} + \frac{C_{L\alpha H} \eta_H S_H}{C_{L\alpha W}} \left(1 - \frac{d\varepsilon}{d\alpha}\right) \bar{X}_{ACH}}{1 + \frac{C_{L\alpha H} \eta_H S_H}{C_{L\alpha W}} \left(1 - \frac{d\varepsilon}{d\alpha}\right)} \quad (48)$$

3.4.1.5 Modeling the Aircraft Longitudinal Small Perturbation Aerodynamic Forces and Moments

There are sets of particular stability derivatives for lift, drag and pitching moment that are associated with perturbations in terms of velocities. One set of derivatives includes the U-derivatives. The U-derivatives are related to small perturbations in the forward speed (Napolitano, 93)[8]. Because these derivatives deal with increments in the forward speed, the results are negligible at low subsonic conditions. A second set of small perturbation stability derivatives are the C_d , C_l and C_m with respect to pitch rate (q) and rate of change of the angle of attack ($\dot{\alpha}$). A complete set of equations to find the $\dot{\alpha}$ and q derivatives can be found on Appendix B.

3.4.2 Modeling the aircrafts lateral steady state aerodynamic forces and moments

Similar to the aerodynamic forces and moments analyzed in the previous sections, the lateral steady state aerodynamic forces and moments will be induced through deflection of spoilers and rudder. The targeted forces and moments are the steady-state lateral force and the steady state rolling and yawing moments. The analysis will follow the same as those expressed in Napolitano's textbook [8], as follows.

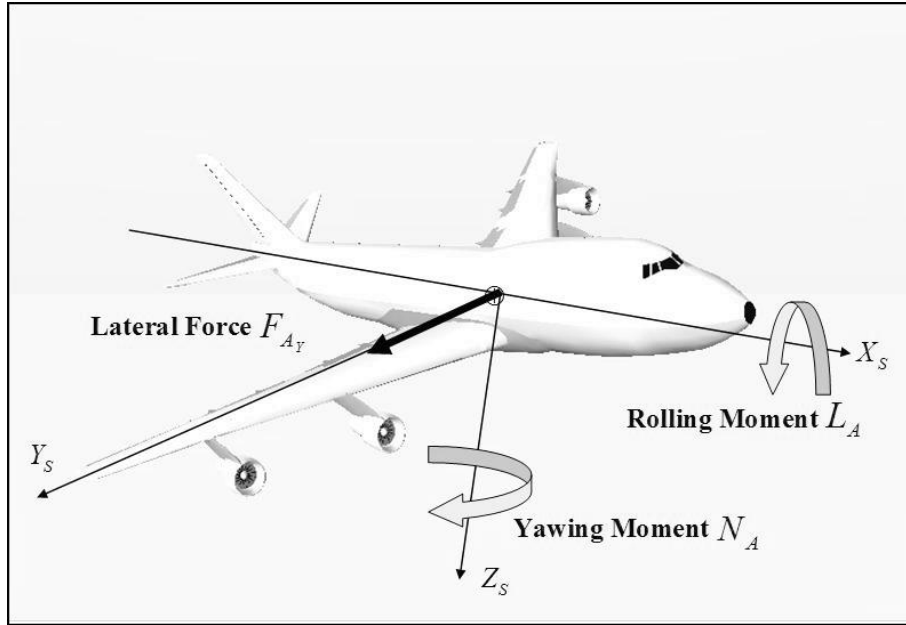


Figure 55: Steady State Lateral Directional Forces and Moments (Napolitano, 136)[8]

3.4.2.1 Modeling of the steady-state lateral force

The steady state lateral force pushes an aircraft from the side, in the Y axis as demonstrated above. This force is a summation of the steady state lateral forces due to various parts of the aircraft including the wing, body, and horizontal and vertical tail. These forces are dependent on the general shape of the aircraft body as well as the dihedral or anhedral in the aircrafts wings. Traditionally most aircraft do not have large dihedral or anhedral angles in the horizontal tail, so this force is typically zero. Since the designed aircraft will follow the same concept, the lateral force due to the horizontal tail will be approximately zero. Unlike the horizontal tail, the contribution of vertical tail to this force can be quite substantial.

The contribution of the wing to the lateral force is highly dependent on the dihedral angle of the wings. The following equation determines the contribution of the wings to the lateral aerodynamic force.

$$C_{Y\beta_w} = -0.0001 |\Gamma_w| 57.3 \quad (49)$$

In Equation 49, Γ_w is the wing dihedral angle in radians. The relationship between the steady state lateral force and the fuselage can be given by a similar expression. In order to find the contribution of the lateral force due to the fuselage, the wing configuration (high or low) with respect to the fuselage needed to be included.

The contribution to the lateral force due to the vertical tail can be found with the following equation.

$$C_{Y\beta_V} = -K_{Y_V} |C_{L\alpha_V}| \eta_V \left(1 + \frac{d\sigma}{d\beta}\right) \frac{S_V}{S} \quad (50)$$

The parameter K_{Y_V} in this equation is a function of the span of the vertical tail over two times the radius of the fuselage where the tail intersects. $C_{L\alpha_V}$ can be found through the Polhamus formula, just like $C_{L\alpha_W}$. The vertical tail effectiveness and the sidewash angle can be simplified as seen in the following equation.

$$\eta_V \left(1 + \frac{d\sigma}{d\beta}\right) = 0.724 + 3.06 \frac{S_V/S}{1 + \cos \Lambda_{C/4}} + 0.4 \frac{z_W}{d} + 0.009AR \quad (51)$$

The contribution to the lateral force due to the deflection of the rudder can be summarized by the equation below.

$$C_{Y\delta_R} = |C_{L\alpha_V}| \eta_V \frac{S_V}{S} \Delta(K_R) \tau_R \quad (52)$$

In this equation K_R is simply a correction factor for the span of rudder with respect to the vertical tail and τ_r is the control surface effectiveness for the rudder. τ_r is a function of the mean chord of the rudder divided by the mean chord of the vertical tail, this parameter can be found using the Figure 56.

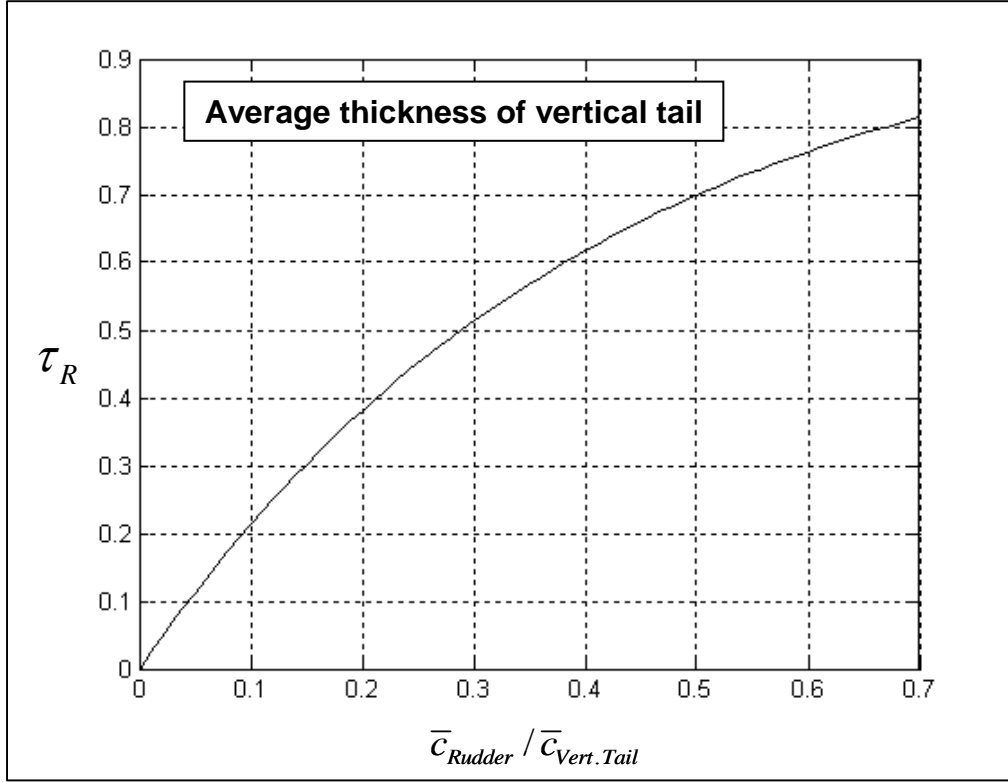


Figure 56: Effectiveness of the Rudder as a Function of $C_{Rudder}/C_{Vertical Tail}$ (Napolitano, 149)[8]

The rest of the equations used to find the total steady-state lateral forces can be found in Appendix B.

3.4.2.2 Modeling of steady-state rolling moment

Similar to the lateral steady state forces, the modeling of the steady-state rolling moment is another build-up approach in which the wings, fuselage, horizontal and vertical tails play an important role. The following equation calculates the rolling moment due to the wing-body of the aircraft.

$$C_{L\beta_{WB}} = 57.3C_{L1} \left[\left(\frac{C_{l\beta}}{C_{l1}} \right) |_{\Lambda_{c/2}} K_{M\Lambda} K_f + \left(\frac{C_{l\beta}}{C_{l1}} \right) |_{AR} \right] + 57.3 \left\{ \Gamma_W \left[\frac{C_{l\beta}}{\Gamma_W} K_{M\Gamma} + \frac{\Delta C_{l\beta}}{\Gamma_W} \right] + (\Delta C_{l\beta}) |_{ZW} + \varepsilon_W \tan \Lambda_{c/4} \left(\frac{\Delta C_{l\beta}}{\varepsilon_W \tan \Lambda_{c/4}} \right) \right\} \quad (53)$$

This equation is a function of the wing sweep angle, correction factors related to Mach number and wing sweep angle, correction factors due to the position of the fuselage, wing aspect ratio, and contribution of the wing dihedral angles. Pages 156-157 in Napolitano's textbook provide empirical graphs that were used to calculate each component in the equation. The contribution of the horizontal tail to the steady-state rolling moment was approximated to be zero since the aircraft has no dihedral. The contribution of the vertical tail due to the rolling moment can be calculated by the following equation.

$$C_{l\beta_V} = -K_{Y_V} |C_{L\alpha_V}| \eta_V \left(1 + \frac{d\sigma}{d\beta} \right) \frac{S_V}{S} \frac{(Z_V \cos \alpha_1 - X_V \sin \alpha_1)}{b} \quad (54)$$

The rolling moment coefficient associated with the deflection of the rudder ($C_{L\delta_R}$) can be found by the equation below.

$$C_{l\delta_R} = |C_{l\alpha_V}| \eta_V \frac{S_V}{S} \Delta(K_R) \tau_R \frac{(Z_R \cos \alpha_1 - X_R \sin \alpha_1)}{b} \quad (55)$$

In this equation K_r and τ_r are the same parameters used in the calculation of the steady-state lateral force due to the rudder. The fraction in the equation is simply the moment arm between the rudder and the center of gravity of the aircraft, and η_v is the effectiveness of the vertical tail. Other equations related to the calculation of the steady-state rolling moments can be found on Appendix B.

3.4.2.3 Modeling of steady-state yawing moment

The steady-state yawing moment follows the same definition as the steady-state rolling moment. The yawing moment is a contribution of wing, fuselage and the tail, but like the rolling moments, there is also a yawing moment with respect to spoiler and rudder deflections. In this particular derivative, the yawing moment due to the wings in any configuration is found to be

negligible due to the lack of wetted area. Hence, the yawing moment becomes only a function of the fuselage, vertical tail and control surface deflections. The following equation mathematically represents the contribution of the fuselage to the yawing moments.

$$C_{n\beta_B} = -57.3K_N K_{Rl} \frac{S_{B_S} l_B}{S b} \quad (56)$$

In this equation, K_N , K_{Rl} are empirical factors for the wing-body and the effect of the Reynolds number on this location. Figures 4.68 and 4.69 in Napolitano's textbook can be used to find these coefficients [8]. S_{B_S} and l_B are geometric coefficients, the fuselage side surface and the length of the fuselage respectively. The equation to find the yawing moment due to the vertical tail is very similar to the equation for finding the rolling moment.

$$C_{n\beta_V} = K_{Y_V} |C_{L\alpha_V}| \eta_V \left(1 + \frac{d\sigma}{d\beta} \right) \frac{S_V (X_V \cos \alpha_1 + Z_V \sin \alpha_1)}{S b} \quad (57)$$

This is perhaps the most important coefficient for the yawing moment. Often enough, it can be assumed that the contribution of the fuselage is negligible when compared to the vertical tail contribution. (Napolitano, 174)[8].

Another yawing moment derivatives occur due to the deflection of the rudder. The equation to calculate this derivative, seen below, is very similar to the one used to find the rolling moment due to rudder deflection.

$$C_{n\delta_R} = -|C_{l\alpha_V}| \eta_V \frac{S_V}{S} (K_R) \tau_R \frac{(X_R \cos \alpha_1 + Z_R \sin \alpha_1)}{b} \quad (58)$$

3.4.2.4 Modeling the Aircraft Lateral Small Perturbation Aerodynamic Forces and Moments

Similar to the longitudinal direction, there are also derivatives that correlate to small perturbations in the lateral direction. There are a total of nine derivatives. Three of these derivatives are known as the $\dot{\beta}$ derivatives. They are similar to the $\dot{\alpha}$ derivatives in the longitudinal direction but can be assumed to be zero due to the low magnitude of the side-wash effect. The next set of derivatives are the P derivatives which model the lateral force due to roll rate, the rolling moment due to roll rate, and the yawing moment due to the roll rate. Some of these derivatives are heavily involved mathematically and follow a build-up method similar to the derivatives explained above. There are also the R derivatives which model the lateral force, rolling moment, and yawing moment due to the yaw rates. A complete set of equations to model these derivatives can be found in Appendix B.

3.4.2.5 Modeling of steady-state rolling moment & yawing moments with Spoiler

Deflections

The design of the aircraft called for spoilers, which can be used to turn by reducing lift and adding drag to the side of the wing where the spoiler is deflected. The use of spoilers also give an advantage in landing if deployed symmetrically.

In order to estimate the stability derivatives for the rolling moment and yawing moment due to the deflection of the spoilers, two different approaches had to be considered. The first approach was a numerical approximation similar to the ones provided by Marcello Napolitano, coming from the United States Air Force Stability and Control DATCOM [12]. The set of equations include empirical data that is provided in the DATCOM for full-scale aircraft. A

complete set of equations to approximate these derivatives can be found on page 2244 for the rolling moment and page 2295 for the yawing moment [12].

Since these approximations were crude, a second approach to calculate these derivatives was considered. Through the aid of Computational Fluid Dynamic models, the lift and drag coefficients of the airfoil with spoilers deflected at various angles were simulated. Through this computational model, we computed the surface pressure on the S1223 airfoil. The force and moment coefficients were then obtained through integration of the pressure and skin friction. In order to attain the best possible results, the mesh needed to be as refined as possible. Due to the high-camber airfoil and convergence to a single point at the trailing edge, the airfoil was modified and shortened by 5% in order to facilitate the design of the mesh domain as seen in the figure below.

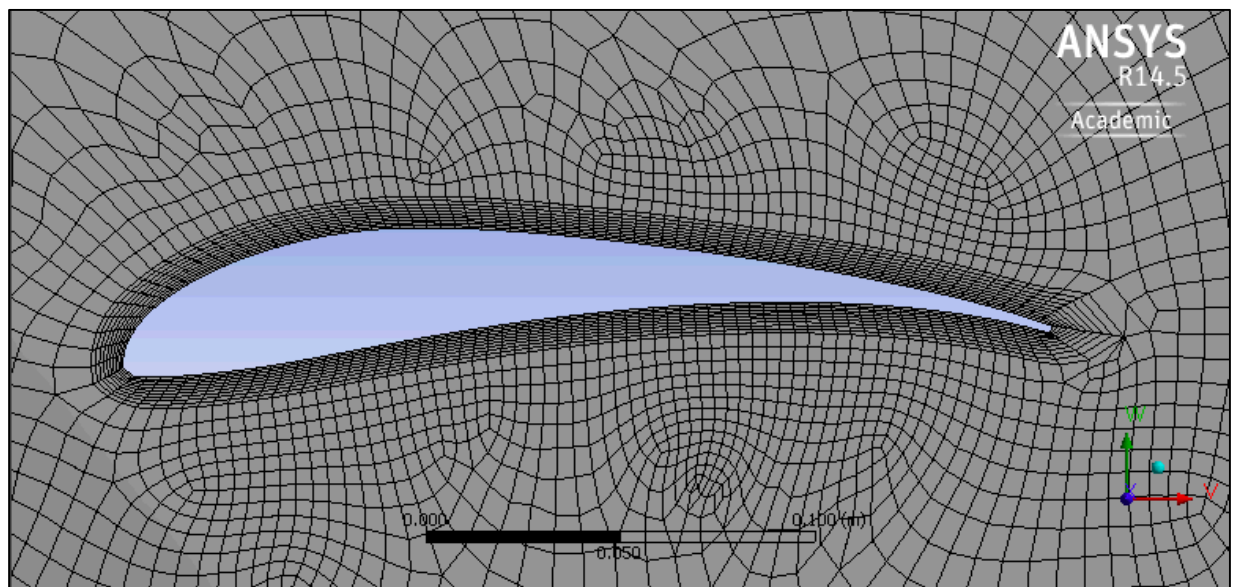


Figure 57: ANSYS C-Mesh Domain

The general set-up for the simulation followed a pressure based transfer simulation with an absolute velocity formulation and steady time in a two-dimensional space planer. The model selected was a viscous laminar model and the transition k-kl-omega.

In order to visualize the effect of the spoiler deflections, a spoiler was design to be 10% of the chord and the coordinates of the airfoil where modified to simulate the deflection of the spoiler at approximately 5, 10 and 15 degrees. These coordinate are then entered into the ANSYS design modeler to fully develop the C-mesh domain, and then for mesh development.

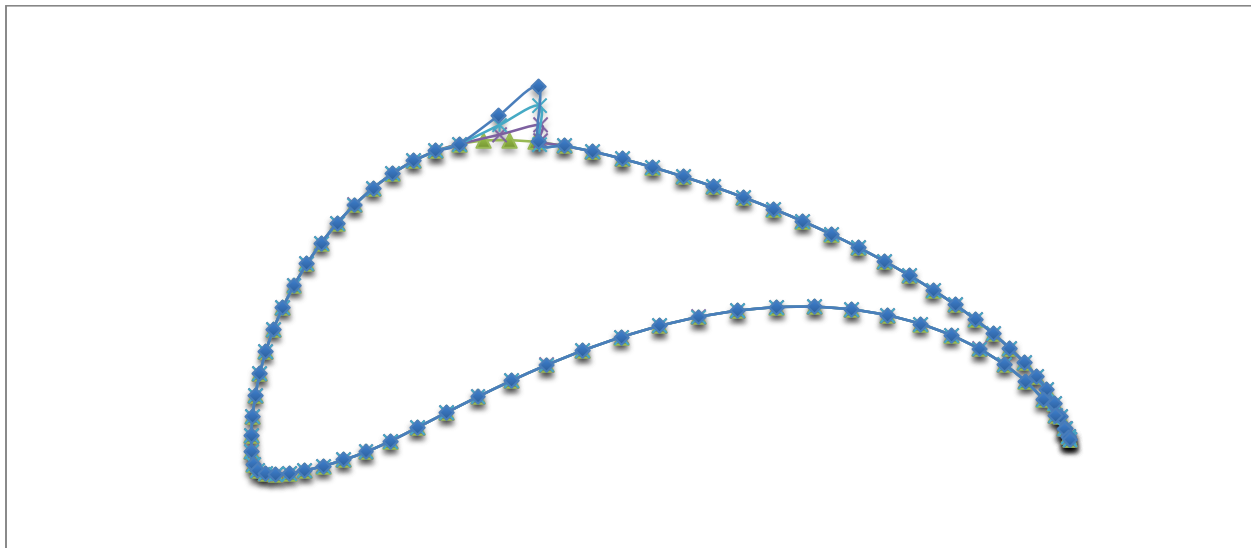


Figure 58: Modified Airfoil Coordinates for Spoiler Deflection

The figure above is an exaggerated representation of the s1223 airfoil, shown only to demonstrate the changes in the airfoils coordinates that would simulate the spoiler deflection.

Every deflection case was run at a speed of 10 m/s and lift and drag coefficient data was collected at 0, 2, 4, 6, and 8 degrees angles of attack. When all cases were completed and data had been gather, the values for lift and drag versus angle of attack were linearized in order to attain an average value for the rolling and yawing moment coefficients.

3.4.3 Aircraft Static Stability

As described by Napolitano, “An aircraft is statically stable if it features the capability of developing aerodynamic and thrust forces and moments which counteract a perturbation in a motion variable starting from a steady-state flight condition” (Napolitano, 306)[8]. The textbook provides a set of criteria that an aircraft must satisfy in order to be considered statically stable.

Table 11: Static Stability Criteria

$Ct_{xu} - CD_u < 0$	$Cl_p < 0$
$CY_\beta < 0$	$Cm_q < 0$
$CL_\alpha > 0$	$Cn_r < 0$
$Cm_\alpha < 0$	$Cl_\beta < 0$
$Cn_\beta > 0$	$Cm_u > 0$

With a finalized MATLAB code (Appendix C), it was simple to change the flight conditions or payload, and even aircraft geometry if it was necessary to determine if each configuration is statically stable.

The configuration of the aircraft used to attain the results above was the final configuration used for flight and competition. This includes geometric sizes and inertial data. As it can be seen in the table below, the parameter that changes the most is the pitching moment with respect to the angle of attack. The reason behind this is simply the addition of weight. As more weight (payload) is added to the aircraft, the center of gravity moves further away from the aerodynamic center of the wings and horizontal tail. This creates larger moment arms between them and hence a decreasing pitching moment stability derivative. The lower the value, the more stable the aircraft is in pitch.

Table 12: Static Stability Results

Stability Criteria	Zero Payload	20% Payload	50% Payload	Full Payload
$C_{t_{xu}} - CD_u < 0$	0	0	0	0
$CY_\beta < 0$	-0.3174	-0.3174	-0.3174	-0.3174
$CL_\alpha > 0$	5.9249	5.9250	5.9253	5.9257
$Cm_\alpha < 0$	-0.0571	-1.0693	-2.1477	-2.1478
$Cn_\beta > 0$	0.0824	0.0824	0.0824	0.0824
$Cl_p < 0$	-0.2032	-0.2032	-0.2032	-0.2032
$Cm_q < 0$	-24.0465	-26.1496	-28.4877	-28.4892
$Cn_r < 0$	-0.1057	-0.1057	-0.1057	-0.1057
$Cl_\beta < 0$	-0.1448	-0.1448	-0.1448	-0.1448
$Cm_u > 0$	0	0	0	0

Other stability derivatives changed due to the different flight conditions for each payload. Based on the results above, it can be certain that the aircraft is statically stable for all intended flight conditions and payloads.

3.4.4 Aircraft Dynamic Stability

“An aircraft is dynamically stable if the perturbations of the motion variables—associated with either an external disturbance or a pilot’s maneuver—decrease with time to zero or to a new set of steady-state values after either the disturbance or the pilot’s maneuver has stopped.” (Napolitano, 306) [8].

In order to proceed with the analysis, a more descriptive set of derivatives needed to be calculated. These derivatives are known as the dimensional stability and control derivatives for both the longitudinal and lateral directions. The calculation of the derivatives includes the static stability derivatives previously found, flight conditions and geometric and inertial characteristics of the aircraft.

Aircraft Dynamics: From Modeling to Simulation [8] goes over two different ways to simulate the dynamic stability of an aircraft. One method consists of solving the aircraft's equations of motion based on transfer functions and Laplace transformations. This approach expresses relationship between a single input and a single output. The desire for this model is to have a multiple input multiple output (MIMO) system. Although this is possible with transfer functions, it is not the most practical solution.

The second approach used in Napolitano's textbook [8] is a state variable modeling approach of the aircraft dynamics. A state variable model is more appropriate for this problem since it can handle a MIMO system. "The state variables of a system are defined as a minimal set of variables such that the knowledge of these variables at any initial time t_0 in addition to information on the input excitation applied at any time $t > t_0$ are sufficient to determine the state of the system at any time $t > t_0$." (Napolitano, 433)[8]. In this system, the inputs were deflections in the elevator, rudder, and spoilers. The outputs of the system created in the longitudinal direction were the longitudinal vertical acceleration, longitudinal angle of attack, linear longitudinal velocity, pitch angular rate, and the Euler pitch angle. In the lateral direction these outputs were the lateral acceleration, lateral angle of attack (sideslip angle) the roll angular rate, yaw angular rate and the Euler roll angle. The outputs were plotted against time and were effective in demonstrating the behavior the aircraft would exhibit (over time) with different inputs in the elevator, spoilers and rudder. Since the code is generated on MATLAB, it was fairly simple to test the stability of the aircraft with different payloads at different flight conditions. Below is an example of the behavior of the aircraft in flight with a 50% payload and a speed of 20 ft/sec for an elevator/rudder deflection of $\pm 2^\circ$ and a spoiler deflection of $\pm 10^\circ$ (essentially a turn).

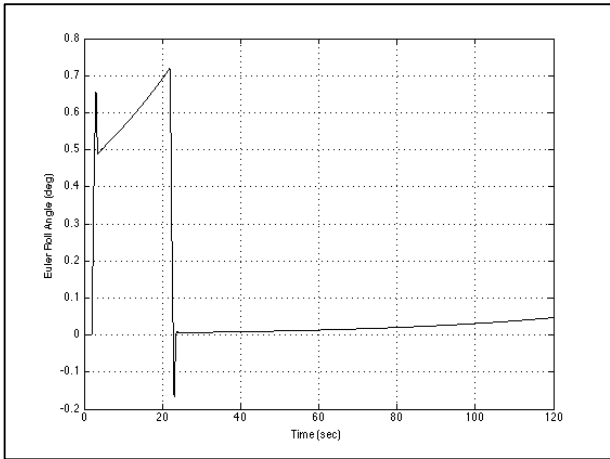


Figure 59: Euler Roll Angle Response

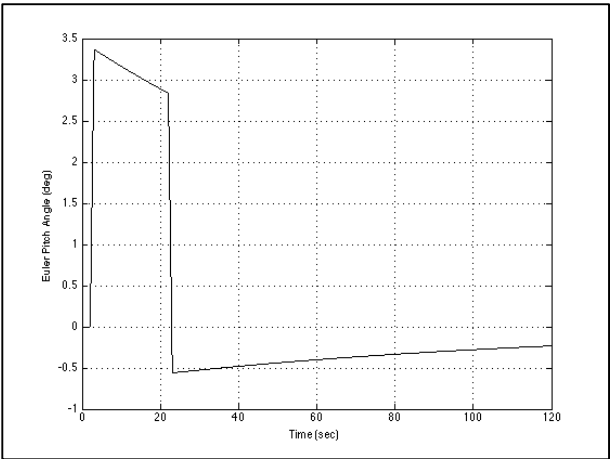


Figure 60: Euler Pitch Angle Response

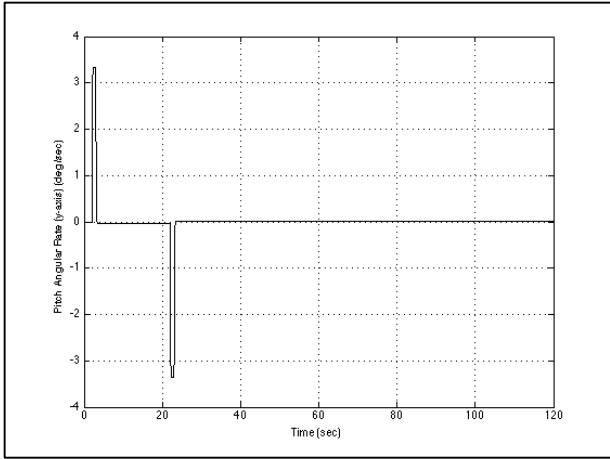


Figure 61: Pitch Angular Rate Response

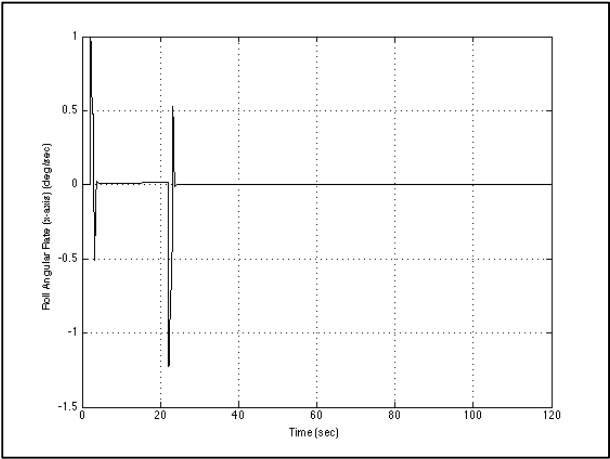


Figure 62: Roll Angular Rate Response

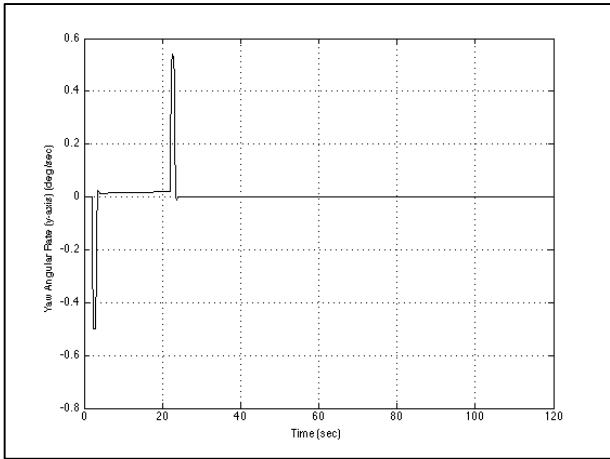


Figure 63: Yaw Angular Rate Response

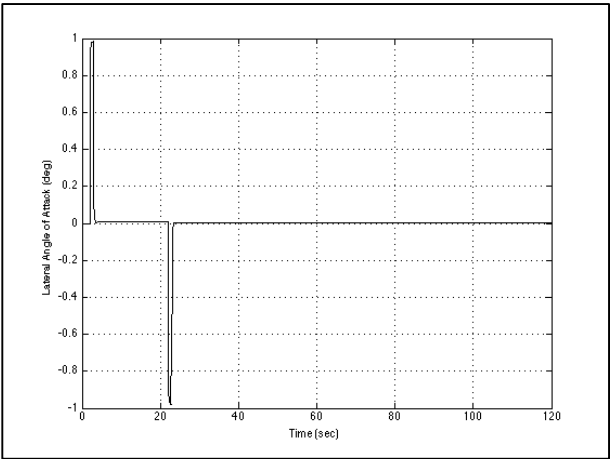


Figure 64: Lateral Angle of Attack Response

3.5 Trim Analysis

Due to the ability to change the payload weight and its location and to mechanically trim the stabilator before flight, the stability and controllability of the aircraft depend on the ground setup. In order to ensure stability with any number of payload plates, the number of steel payload plates and the location of the assembly was factored in to adjust the location of the center of gravity of the aircraft. As the number of payload plates increases linearly, the location also changes incrementally between two limit points. The two limit points were adjusted to ensure that the static margin generally stays at a comfortable level, above 0.25, for payload carrying missions (for an empty mission, the static margin is about 0.1). The static margin was calculated with Equation 59.

$$SM = \frac{x_{AC} - x_{CG}}{\bar{c}} \quad (59)$$

$$\text{Where } x_{CG} = \frac{P_n x_{CG \text{ payload}} + EW x_{CG \text{ empty}}}{P_n + EW} \quad (60)$$

Based on the total weight for each case, the moments about the center of gravity were balanced to determine the lift coefficient of the horizontal tail using Equation 61.

$$C_{L \text{ tail}} = \frac{S_{C_L w} (x_{CG} - x_{AC w}) + S_{C_M w} \bar{c}}{(x_{AC \text{ tail}} - x_{CG}) S_h} \quad (61)$$

The required angle was determined by matching the lift coefficient to aerodynamic data for the tail determined with the same method as the wings. Using the previously determined geometric formula for the tail trim device, the ultimate result of this tool is the distance that has to be set between the tail structure brackets and the payload location for every payload size. A table containing this information can thus be used to properly trim and adjust the aircraft before flight (Table 13).

Table 13: Stabilator Trim Table

# of payload plates	Payload [lbs]	Payload location [m]	Total weight [N]	Static margin	stabilator pitch up [deg]	brackets' setting [mm]
0	0.00	0.000	13.34	0.07	1.3	75.5
2	0.99	0.027	17.77	0.22	0.6	77
3	1.49	0.033	19.98	0.26	0.4	77.5
4	1.99	0.040	22.19	0.30	0.3	77.5
5	2.49	0.046	24.40	0.32	0.2	78
6	2.98	0.052	26.61	0.33	0.1	78
7	3.48	0.058	28.82	0.35	0.1	78
8	3.98	0.064	31.03	0.35	0.1	78
9	4.47	0.070	33.24	0.36	0	78.5
10	4.97	0.076	35.45	0.36	0	78.5
11	5.47	0.083	37.66	0.35	0.1	78
12	5.96	0.089	39.87	0.35	0.1	78
13	6.46	0.095	42.08	0.35	0.1	78
14	6.96	0.101	44.30	0.34	0.1	78
15	7.46	0.107	46.51	0.33	0.1	78
16	7.95	0.113	48.72	0.32	0.2	78

4.0 Preliminary Testing

Before beginning the construction of a full model, several tests were conducted to verify the performance of the design. A wing section was built for wind tunnel testing, several key structural components were structurally loaded to failure, and a foam model was built for glide testing and practice.

4.1 Wind Tunnel Testing

In order to verify the aerodynamic analysis results, a wing section with the mean aerodynamic chord of the full wings and a span of half of the length of one wing section was tested on a force balance in the wind tunnel. To remove the effects of wing tip vortices, side plates were placed at each end of the wing without being connected to the wing or force balance to prevent inaccuracies in the results.

The normal force, axial force, and the moment were recorded every 2 degrees between -6 and 12 degrees of angle of attack. The velocity was determined using the maximum velocity of 55 m/s at 62.5 Hz. A frequency of 9.4 Hz was used, corresponding to a velocity of 8.27 m/s, just over the expected cruising velocity.

The full setup is shown in Figure 65. The results for the lift and drag coefficients shown in Figure 66 and 67 were compared to both the theoretical values for the airfoil from XFOIL and the calculated values adjusted for 3D effects at the same velocity.

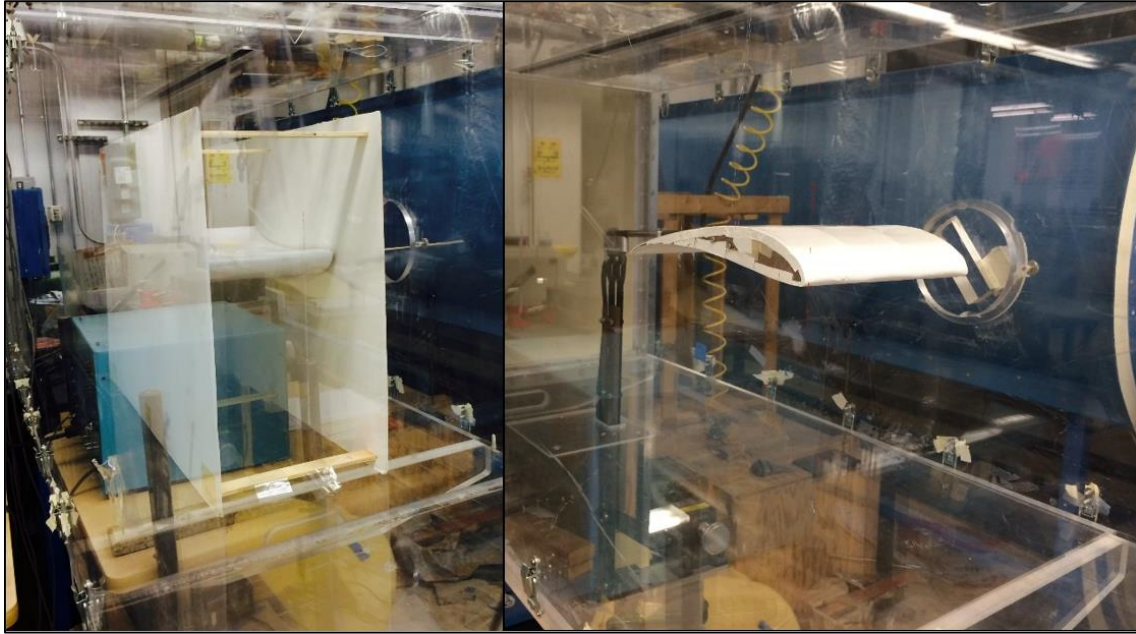


Figure 65: Wind Tunnel Wing Test Setup

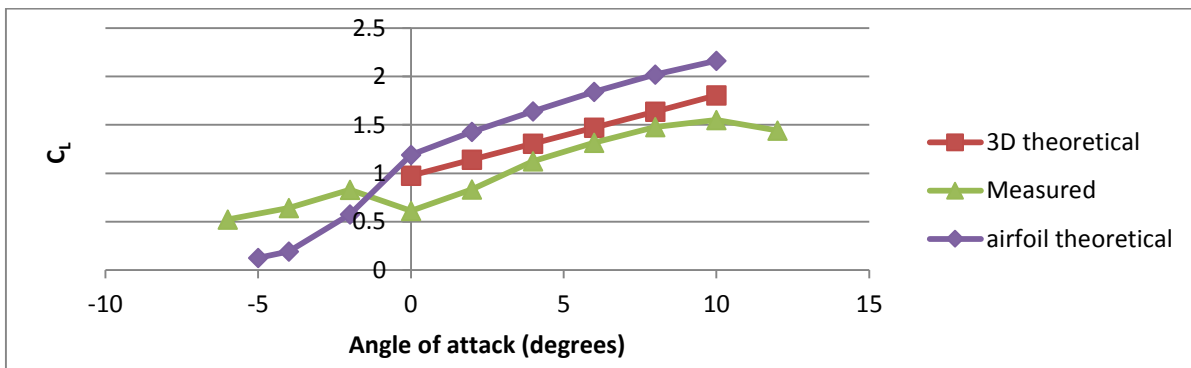


Figure 66: Experimental Lift Coefficient Compared to Theoretical Data

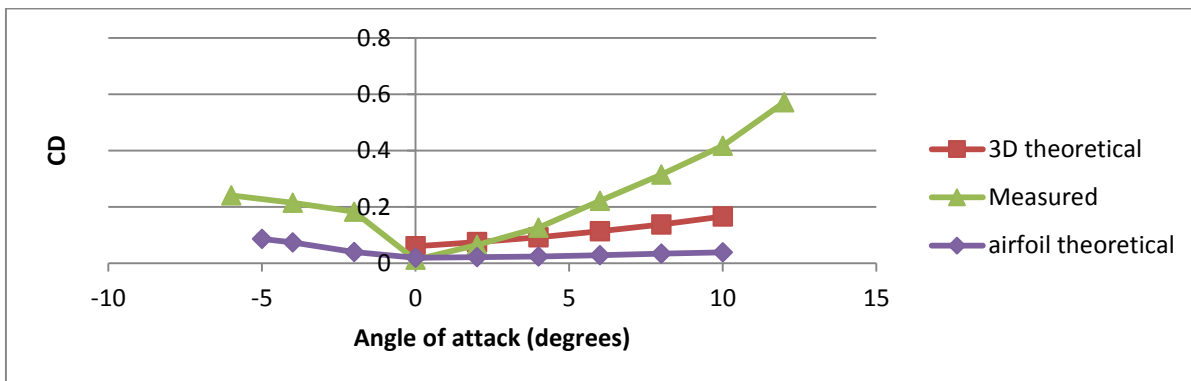


Figure 67: Experimental Drag Coefficient Compared to Theoretical Data

The force balance readings of normal and axial force were used to determine the lift and drag according to Equations 62 and 63.

$$L = N \cos \alpha - A \sin \alpha \quad (62)$$

$$D = N \sin \alpha + A \cos \alpha \quad (63)$$

The measured values for the lift coefficient were lower than the expected values and the drag coefficient grew at a much larger rate at high angles of attack. The discrepancy in lift values may have been caused by an inaccurate wind tunnel velocity, large drift of the zeroed value of the force balance, interference effects in the wind tunnel, or imperfections in the wing section. The drag results were determined to be inconclusive due to the inaccuracy of measuring the very small drag force on the wing with a force balance meant for much larger values.

In order to account for the possible overestimation of lift and underestimation of drag, motor and propeller combinations with over 30% more thrust values than those calculated to be necessary were selected for further testing. With a larger motor, the aircraft could fly at higher speeds to attain the needed lift while counteracting the larger drag force.

4.2 Structural Testing

The wing joiner between the innermost wing section and the fuselage and the central spar piece (initially Basswood) shown in Figure 68 were both tested to determine if they could withstand the high loads expected without failing.

The central spar piece was loaded as shown in Figure 69 to simulate the vertical forces between the wing joiner rods and the lengthwise rod that supports the payload bay. The spar piece was able to hold 190 pounds without failing before the test was stopped.

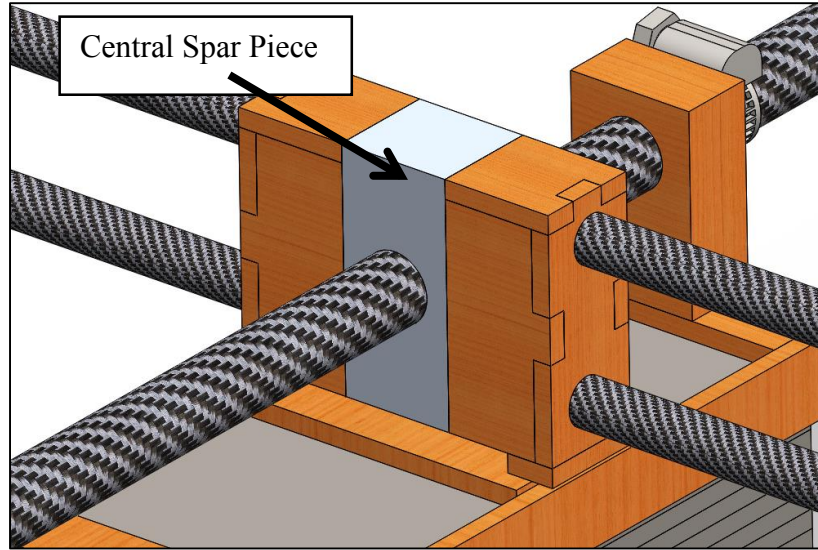


Figure 68: Fuselage with Central Spar Piece

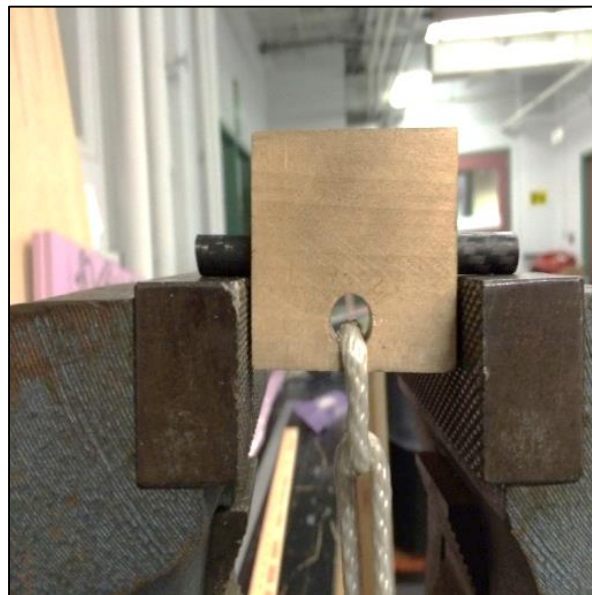


Figure 69: Central Spar Piece Test Setup

The wing joiner block test setup as shown in Figure 70 was used to simulate the loads it would experience during flight while placed between the two carbon fiber strips of the spar. The joiner failed when loaded with 56.3 Nm providing a factor of safety of 2.23 for the expected flight load. The design was then further improved by increasing the space between the holes and replacing the carbon fiber tubes with solid pultruded rods.



Figure 70: Joiner Block Test Setup

Structural testing was also conducted on the full innermost wing section using the setup shown in Figure 70. The carbon fiber tube in the joiner that was held in the vise snapped with 18.8 pounds hanging from the opposite end of the wing. This provided a bending moment of 48.4 Nm on the broken joiner, twice the expected flight load. The rest of the wing structure remained intact during the test. Given the unalterable test wing, the team was not able to fail the structure with a bending test.



Figure 71: Inner Wing Structural Test Setup

4.3 Foam Model Glide Testing

Before finalizing the aircraft design, a foam model was built as an initial prototype. Using the foam model, the aerodynamic approximations for lift and drag could be tested through the glide ratio and the stability calculations could also be verified. A foam model also allowed for early practice of the hand launch of the aircraft without risking expensive damage to the final product.

A full scale foam model of the aircraft was created with pink insulating foam. It was manufactured carefully using a hot wire and laser-cut airfoil profiles. In order to make the model, the aircraft was divided into parts. Overall, there were six wing sections (correlating with the actual plane), the fuselage, the tail boom, the elevators (which were just fixed horizontal stabilizers) and the vertical stabilizer.



Figure 72: Foam Test Glider

The foam components were assembled using a combination of wooden dowels as joiners and scotch tape as added support. Due to some sagging in the wings, large wooden dowels on the underside of the wing were used to prevent almost all of the negative dihedral. The tail boom was

originally inserted into the fuselage with a bit of wood glue, but this proved to be too unstable and the tail kept trying to spin and leave the vertical stabilizer facing downward. Two wooden dowels placed under the elevators steadied the tail as a whole.

Once the plane was assembled, it was taken to the Harrington Gymnasium for flight testing. The best flight was from a height of 9.5 feet with a distance of 37.5 feet. This made the glide ratio a little under 4.0, which was much less than anticipated. Despite the underwhelming ratio, it showed that the plane was stable in gliding. More importantly, the team thrower was able to practice in order to ensure a fast, level launch for the real aircraft.

4.4 Thrust Testing

The chosen motor and several propellers were tested in the wind tunnel. The motor was mounted to a test stand with a lever arm of 23 inches and the 48 inch perpendicular arm rested on an electronic scale. The setup is shown in Figure 73. Each propeller was tested with the battery charged to 11.5V and with the wind tunnel running at 8.2 m/s, just over the expected cruise velocity of the aircraft. The scale reading was allowed a few seconds to stabilize after full throttle was applied. Values for voltage and scale measurements were then recorded every five seconds for a period of 30 seconds. The scale measurements were used to calculate thrust.

The 10x5E (electric) propeller had the highest thrust, resulting in 72% more thrust than the necessary cruise value of 4.18 N. The 11x3.8SF (slow-flyer) propeller, larger in diameter and smaller in pitch had a slightly smaller thrust value, and was kept as a backup due to its higher acceleration. The 10x6F (folding) propeller produced 50% more thrust than needed, very close to the predicted value, and was also named a backup propeller if the landings appear to damage the motor shaft. It is very important to note that the tests were performed with an 11.5V battery voltage,

much lower than the 12.6V maximum used during flight. Therefore, the convergence between predicted and tested values is deemed to further increase, just like the total available thrust. The results are summarized in Table 14.

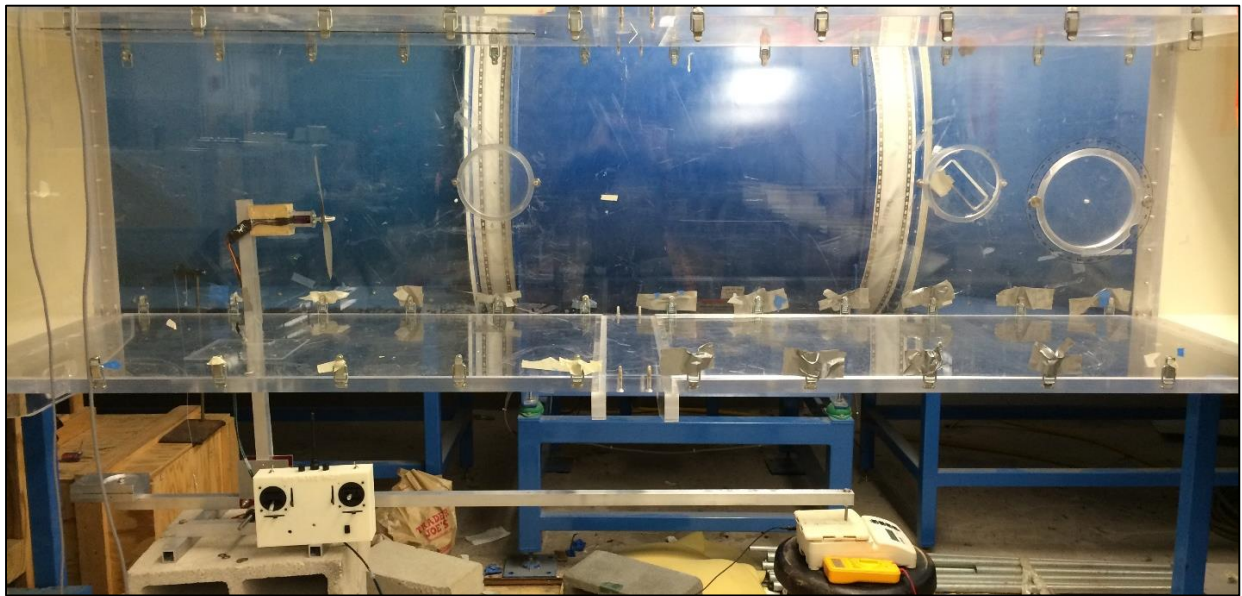


Figure 73: Thrust Testing Setup

Table 14: Thrust Test Data

Propeller	Thrust (N)	30s Voltage Drop [V]
11 x 3.8 SF	6.99	0.3
10 x 4.7 SF	6.78	0.3
10 x 3.8 SF	6.37	0.2
9 x 6 SF	5.11	N/A
10 x 7 E	5.93	N/A
10 x 5 E	7.20	0.2
9 x 6 E	5.73	N/A
10 x 6 E	6.78	0.2
10 x 6 F	6.26	0.2

5.0 Fabrication

5.1 Wing Fabrication

The ribs and spars of the wings were manufactured in many pieces that were then assembled into the full wing sections. The ribs were made using a two part process. The front part of each rib was laser cut from a sheet of 1/8" balsa wood and the trailing edges were made of 3D printed plastic. The trailing edge of the airfoil was too thin to be laser cut without burning the wood and the thin Balsa was too fragile to hold the airfoil profile when covered with tightly sealed Mylar.



Figure 74: Balsa Rib Set

The balsa wood chosen for the ribs was the lightest grade balsa wood with a density of approximately 4lbs/ft³. The ribs were not supplying the main structural support of the wing so they were designed to save weight. Each profile was modeled in SolidWorks, transferred to AutoCAD, and then loaded into the laser cutter in the Washburn shops at WPI. The balsa wood setting for the laser cutter was adjusted to 60% speed and 50% power. By experimentally tuning the default settings, a more precise cut with no burns was achieved.

The small trailing edge pieces were made using the Objet 3D printer after being modeled in SolidWorks. Although the process was very precise, there were two major drawbacks. The first drawback was that each piece took at least 20 minutes to print. The second being that each piece needed to be hand cleaned using a small brush and needle, adding to the already long time needed to create the final product. However, the drawbacks were acceptable since the process resulted in relatively strong, lightweight, and accurate trailing edges for the ribs. Once the leading and trailing edge pieces were made, they were assembled using CA glue.

Making the spar for this plane proved to be an involved process. Due to the sandwich beam design, the spar for each of the six wing sections was broken up into seven pieces. The inner spar pieces were made out of balsa wood and the piece on either end of each section was made out of bass wood. Each piece was approximately 3 inches wide and 0.5 or 0.3 inches thick.

In order for the spar to be made precisely, the balsa wood pieces needed to be outsourced to a wood shop run by facilities at WPI. This was necessary because there are no available wood shops at WPI for the students. Working with Balsa wood of any kind in the machine shops resulted in pieces that needed to be sanded by hand, and with the working tolerances required by the design, that method was not viable. When outsourced, the 30 balsa pieces of the spar were accurate to a few hundredth of an inch, within the working tolerances of the design; a small amount of manual sanding took care of the surplus material.



Figure 75: B-Section Spar Webs Ready for Assembly

The bass wood pieces of the spar were able to be manufactured in the Higgins machine shop at WPI. In total, ten of these basswood joiner pieces were used in the wings. While sizing them correctly was relatively easy, drilling the holes straight was not. This was due to the fact that the holes had to be drilled through the longest dimension of each piece which is counterintuitive according to standard fabrication principles. Despite going against these principles, the pieces were able to be made using an indicator, center drill, and the proper speeds and feeds.

Once the ribs, webs and joiners blocks were ready, the spar was assembled. In order to line everything up to the precision that was needed, jigs were created. One jig was able to be used for the A and B sections of the wing, while another smaller jig was needed for the smaller C section. A method to assemble the ribs and spar pieces together in the jig was developed in order to ensure the wing section was correctly aligned. A rendering of the basic jig can be seen in Figure 76; the different colors are used to highlight the different elements of the assembly. The jig was created from laser cut Masonite hard-board.

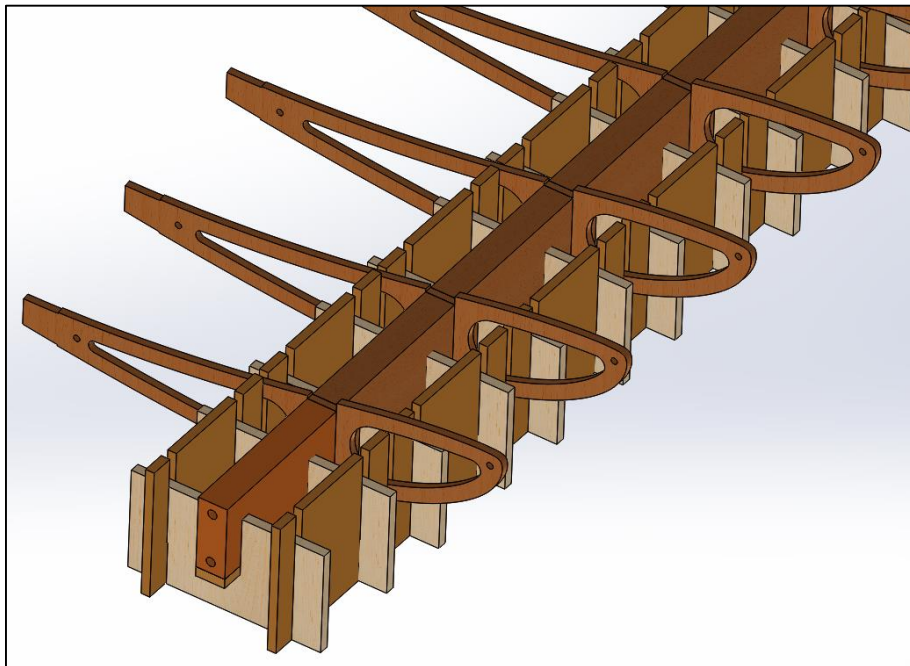


Figure 76: Wing Assembly Jig Concept

The assembly order proved to be very important. First, the bottom carbon fiber strip would be placed directly on the jig. Then, one of the outermost ribs would be placed on top. This would be followed by a small amount of glue on the rib, then one of the seven spar pieces. This method was continued using the appropriate rib and spar piece until the assembly was complete. In order to complete the sandwich beam, a strip of carbon fiber was glued along the top of the spar with epoxy. The resin used to glue the components together was left to set for approximately 24 hours under the pressure exerted by clamps. The spar was then wrapped with Kevlar thread in an X pattern, going both ways (left/right) to ensure no twists exists due to the binding. The connection between the outermost ribs and the basswood joiner was reinforced with small balsa wood triangle pieces with the proper grain orientation.



Figure 77: Wing Structure Assembly Process

The most feature of the jig assembly was discovered only after the first time the jig was used. Apart from the horizontal tabs glued to the torsion-box that keep the assembly locked in a horizontal plane, both sets of vertical components are removable. During assembly, small drops that are squeezed out tend to bond the spar web to the chord-wise elements of the jig. After the

resin sets, the wing skeleton and vertical elements of the jig are lifted off the table and the span-wise supports are removed easily. The chord-wise elements need to be twisted carefully, removed one by one and then cleaned for the next assembly. If the jig elements would have been bonded together permanently, the wing skeleton would probably not come off the jig in its entirety.

Once the inner structure of the wing section was complete, the covering was attached. The order in which the covering was added was important; the design ensured that the edge of any overlapping materials faced away from the incoming air flow. The covering for each wing section was attached in three sections. The first step was covering the trailing edge with a 0.005" PET film and CA glue, done carefully by hand. The second piece was *Solite* Mylar which was ironed over the middle section across the span of the wing. A small (~1 inch) trim iron was used for the difficult bottom wing surfaces (under-camber). Finally, the leading edge was covered with a PET film, in a similar fashion to the trailing edge, but in overlapping strips, each filling the space between two ribs. This design change was due to excessive warping in the PET film during the folding process over the leading edge.

5.2 Fuselage Fabrication

The fuselage of the aircraft needed multiple elements to be able to the wings in place and keep the payload steady. The bottom of the fuselage, or the skid, was made with Rohacell foam covered and laminated with fiber glass, under partial vacuum. A Masonite jig was laser cut and assembled in order to cut the foam to size and then hold it in place while it was setting under partial vacuum. To ensure that the vacuum value was appropriate, laminating film was cut and folded in place over the wet foam-epoxy-fiberglass; it was then attached to the laminating table with double sided sticky tape and duct tape. A hole was punched through and connected to the vacuum pump hose; it was sealed in place with special plumbing product that solidifies quickly.



Figure 78: Landing Skid Foam Assembly Process



Figure 79: Landing Skid Vacuum Lamination

A 0.46" carbon fiber tube was used as the focal point of construction. Two boxes with holes for the carbon fiber tube were attached to the front and back of the foam base. These boxes were made using the laser cutter so there was no considerable wiggle room for the carbon fiber

rod. This four foot tube was broken into sections. Each section had a ferrule and two 3D printed alignment elements glued at one of the ends, such that it could be inserted a few inches into the next section. Since there was a 0.005” factory gap between the ferrules and the tubes, the ferrules were laminated with one layer of paper and thin CA glue. The laminated ferrules were sanded down until the fit with the carbon fiber tubes was very tight.

The cradle that holds the payload in place was also created to be attached to the central carbon fiber tube. The sliding wooden pieces were manually milled to great precision, and the other components were laser cut; everything was assembled manually. The 16 payload plates were made using a CNC mill. They were then fixed with nuts and machine screws to ensure a clean, flush bottom surface.

The central wing joiner assembly was placed on the carbon fiber tube between the two sliders for the payload. Two wooden boxes and one aluminum rectangular prism needed to be made to accomplish this goal. The wooden boxes were made by laser cutting the faces and then gluing them together. The aluminum piece needed to be manufactured using the manual mill. The most important dimension was the position of the holes for the carbon fiber rods that give the wings a four degree incidence angle.

5.3 Tail Fabrication

The horizontal tail was built with a very similar process to the wings. However, the thickness of the spar was three times lower than that of the thinnest wing spar and the geometry of the jig was more complex. Balsa wood elements had to be used to support the spar and ribs in order to align everything properly. Removing the cured stabilizer structure from the assembly jig proved to be more difficult than the same process for the wings. Due to the reduced thickness of the jig elements, some broke and had to be replaced after each assembly. Another tedious task was

to laminate the carbon fiber joiner tubes and sand them until they fit tightly into the square brackets of the tail structure that holds the stabilizers in place.



Figure 80: Horizontal Stabilizer Assembly Process

The vertical tail was built in a simpler fashion. Due to the design, the laser cut components were manually assembled on the torsion box – a really flat table. A particular problem was the asymmetry introduced by applying the Mylar film. Careful rounds of heat-shrinking the Mylar film on one side were able to correct for the issue. Also, for all three stabilizer elements, handling had to be done very carefully since the torsional stiffness was very small until the leading edge PET film was applied.

6.0 Flight Testing

Two flight tests were performed with the aircraft. The first test ended in a crash but allowed major components of the design to be proven successful. A few modifications were made in preparation for the second test, which better confirmed the flight worthiness and capabilities of the design.

6.1 Flight Test 1

The first flight test confirmed the thrust, lift and drag calculations. In the controls area, longitudinal control proved effective but a rudder was determined to be needed for critical situations such as rapid gusts of side wind where small sized spoilers would be too slow. The spoilers were also extended for additional roll control.

On the structural side, the wings spars and the fuselage proved to have the necessary strength to withstand a rough landing, apart from the element joining the wings to the fuselage, which split along the grain – in shear. Reinforcements were designed in order to add lateral strength to the wing roots and an Aluminum replacement was manufactured for the wing-fuselage joiner.

The test also determined that there is no real need for the tail trim due to the very narrow range of incidence angles. A sturdier, non-adjustable, wooden bracket was designed and a new trim table was calculated to ensure the elevator could provide the necessary adjustments to the moment balance and keep the aircraft steady in pitch. In Table 15, a positive angle represents a downward elevator deflection. With many of the payload settings, the elevator deflection angle necessary for steady flight is almost negligible.

Table 15: Elevator Trim Table

# of payload plates	0	2	3	4	5	6	7	8	9	10	11	12	13	14	15	16
Elevator deflection (degrees)	3.09	1.41	0.94	0.60	0.37	0.21	0.10	0.03	0.00	-0.01	0.01	0.04	0.09	0.16	0.23	0.32

6.2 Flight Test 2



Figure 81: Flight Test 2 Aircraft Setup

In the second flight test, the aircraft circled the field several times while exhibiting excellent stability. The elevator provided the necessary pitch control and the extended spoilers combined with the rudder were able to successfully turn the aircraft on a decently small-radius trajectory. The spoilers were used at their full deflection of 45 degrees during turns.

Unfortunately, as the aircraft was making its final turn, the rudder was deflected too much and the additional yawing caused the aircraft to enter sideslip. In the resulting rapid loss of altitude, the aircraft landed at a slight roll angle with the root section of the right wing taking most of the impact. Since the element joining the fuselage and the wings was made of Aluminum, the root wing section spar took most of the horizontal force and failed. It is noteworthy that the spar is not

designed for considerable forces in this plane, but additions of composite spar wrapping at the root can greatly improve it. The fuselage and tail, as well as the left wing sections survived the impact, thus validating the greater part of the design. The need for an element between the fuselage and the wings that can absorb impact was deemed necessary.

For the second flight test the team used a GPS unit to track the motion of the aircraft and gather statistical data. An overlap of the flight course can be seen in Figure 82.



Figure 82: Flight Test 2 Path (Satellite View)

Even though the GPS data for velocity plotted in Figure 83 is a bit rough, an average can give the order of magnitude of the aircraft velocity: 33 mph or 53 km/h or 15m/s. The relatively constant flight regime that can be seen between the 14 and 23 seconds marks shows an even higher cruise velocity of 37 mph or 60 km/h or 17 m/s. These values, double the estimated

needed values, show that the extra thrust greatly increased the flight speed, suggesting that such case should be included into the aerodynamic analysis. An estimation of the top speed could later be used in refined thrust analysis since flight velocity is a very important factor.

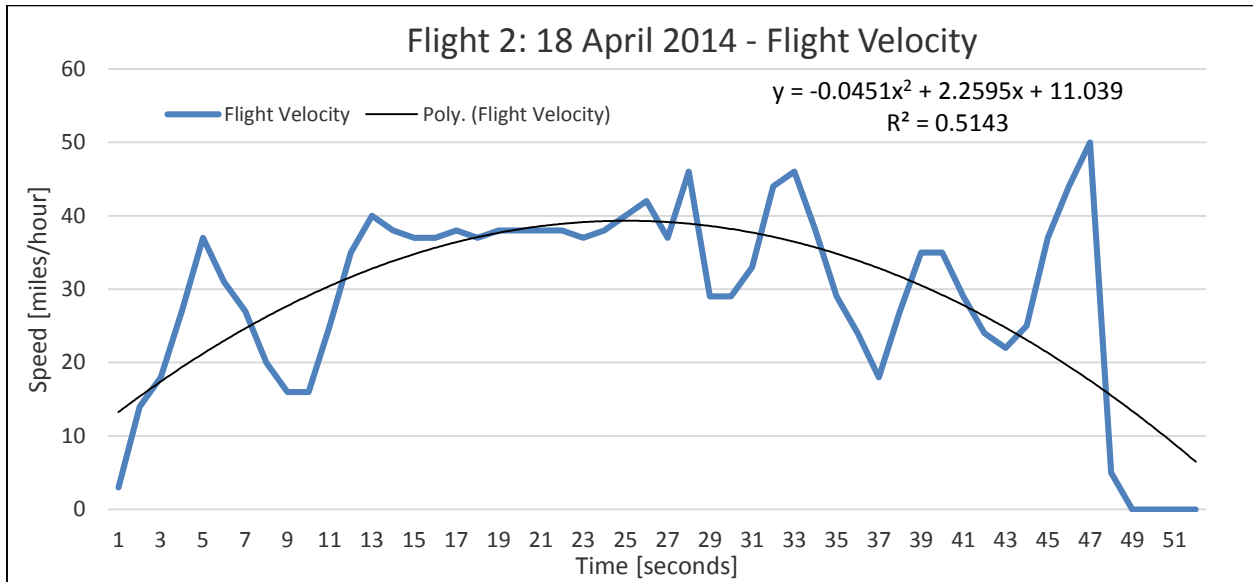


Figure 83: GPS Flight Test Velocity Data

A compilation of images showing the aircraft before the flight, during take-off and in flight can be seen in Appendix D.

7.0 Recommendations for Future Work

Even though our team did not take the aircraft to competition, the experience gathered allows us to forward some pieces of advice for future teams:

- a) Find sponsors early because the budget usually proves not to be enough.
- b) Engineering an aircraft should not refer to creating a simple and safe amateur/hobby-like design. Do not be afraid to have an intricate or eccentric design as long as it promises to provide considerably more performance.
- c) Carefully study past competition entries and use any previously developed tools and concepts that seem useful (such as the propulsion analysis script / approach).
- d) Try to use predictable systems such that every aspect of the design can be pushed to the limit for added performance.
- e) Increase the size of the control surfaces that stability analysis deems appropriate by at least 50%. Empirical data gathered from higher speed and size aircraft does not seem to perfectly apply to the control of MAVs.
- f) Choose a propulsion system that has a predicted thrust considerably higher than the drag value calculated, since, at low speeds and fast wind gusts, extra power can make the difference between flight and rapid loss of altitude.
- g) Develop a force balance that can measure small amounts of lift and drag, since no appropriate alternative is available at WPI.
- h) Put a solid amount of time and effort into a CAD model. Any inaccuracies might result in miscalculated CG's and components that do not fit. While components can be rebuilt, using ballast to balance the plane adds a hefty weight penalty.
- i) Test components and perform changes to the design as the project progresses.

- j) Carefully plan how everything will be assembled before starting the manufacturing process; materials are not cheap and sometimes mistakes are difficult to correct.
- k) Flight testing is very important. If the budget allows, develop several iterations of the aircraft such that it can fly a few times before competition. If the aircraft is very large and expensive, develop flexible / impact absorbing elements that join the wings and tail stabilizers to the fuselage such that a mild crash does not produce critical damage.
- l) Work every week as if the competition date was approaching very fast; concentrating an inappropriately large amount of work during the last weeks of the project is not comfortable and can yield poorer results.

8.0 Conclusion

The challenge set by this project required the design and construction of a lightweight aircraft capable of carrying a large payload and of being packed in a fixed size box. Through careful planning and design, a wing area of just over one square meter was able to fit into a 24” by 18” by 8” box along with the fuselage, tail, and all other necessary components. A strong, lightweight structure was designed around a sandwich beam wing spar and a single carbon fiber rod running the entire length of the aircraft. Detailed aerodynamic and stability analyses ensured predictable performance and allowed for successful control over the aircraft using spoilers, elevators, and a rudder.

Even though the aircraft was not entered into the SAE Aero Design Competition, the team created an aircraft capable of achieving a competitive score while remaining within the limitations set by the rules. The final aircraft, weighing 3.5 pounds and capable of carrying 8 pounds, was created following a detailed design process and analysis. The standards set in this process as well as in the innovations made in the design will be useful for future WPI teams competing in the SAE Aero Design Competition.

References

- [1] SAE. "2014 Collegiate Design Series: SAE Aero Design East and West Rules.": 1-53. Web. 30 Aug. 2013. http://students.sae.org/cds/aerodesign/rules/2014_aero_rules.pdf
- [2] Blair, J., Crosby, P., Connors, E., 2012, "Design of a Micro Class Aircraft for the 2012 SAE Aero Design East Competition," Worcester Polytechnic Institute, DJO 1201, Worcester, MA.
- [3] Crathern, K., Lopes, R. F. V., Momose, T., 2013, "Micro Aircraft Competition Design - Flying Wing," Worcester Polytechnic Institute, Worcester, MA.
- [4] Henriques, Jasmine . "Unmanned Aerial Vehicles (UAV): Drones for Military and Civilian Use." Global Research. N.p., n.d. Web. 29 Apr. 2014.
<<http://www.globalresearch.ca/unmanned-aerial-vehicles-uav-drones-for-military-and-civilian-use/5374666>>."
- [5] Amazon Prime Air." Amazon Prime Air. N.p., n.d. Web. 29 Apr. 2014.
<<http://www.amazon.com/b?node=8037720011>>.
- [6] "Raven RQ-11A." (UAV) : UAS Advanced Development Center. N.p., n.d. Web. 29 Apr. 2014. <<http://www.avinc.com/uas/adc/raven/>>.
- [7] Raymer, Daniel P. (2012) *Aircraft Design: A Conceptual Approach*. 5th ed. Blacksburg, VA: American Institute of Aeronautics and Astronautics.
- [8] Napolitano, Marcello. (2011) *Aircraft Dynamics: From Modeling to Simulation*. Hoboken, NJ: Wiley.
- [9] Traub, Lance W. (2007) Unified Approximation for Nonparabolic Drag Polars. *Journal of Aircraft*, 44(1), 343-345.

- [10] Nielsen, L., “Prop formulae”, Aarhus Modelflyve Club [online], 1998 , URL:
http://www.amc-rc.dk/modelteknik/prop/Prop_formulae_03.pdf [cited 27 March 2014].
- [11] Zenkert, D., An Introduction to Sandwich Construction, Engineering Materials Advisory Services Ltd, UK, 1995.
- [12] United States Air Force Stability and Control DATCOM

Appendix A – Propulsion Analysis Script

Main script

```

%%%Worcester Polytechnic Institute
%%%Micro Aircraft 2 MQP
%%%Main propulsion analysis script
tic;
clc;
clear;
warning('off');
%%%Input files - battery and motors
batteries = xlsread('batteries.xlsx');%name, Vb, Rs
[motors, names, raw] = xlsread('motors.xlsx', 'one');%name, IO, Rm, Kv, Icmax, W
propellers = {'PER3_8x4F.dat', 'PER3_9x5F.dat', 'PER3_10x6F.dat', ...
    'PER3_11x8F.dat', 'PER3_12x85F.dat', 'PER3_13x7F.dat', 'PER3_13x10F.dat', ...
    'PER3_14x10F.dat', 'PER3_15x12F.dat'}; %filenames

%%%Input Parameters
V = 8; %cruise speed [m/s]
Vto = 7; %takeoff speed [m/s]
tf = 5*60; %flight time [s]

%%%run calculations
master_output_matrix = [];%filtered results
master_output_matrix2 = [];%raw results
n_motors = size(motors,1);
n_propellers = numel(propellers);

for i=1:n_propellers
    filename = propellers{i};
    propname = strrep(filename, '.dat', '');
    propname = strrep(propname, 'PER3_', '');
    propname = strcat(' Prop ', propname);
    count = 0;
    results = [];
    for j=1:n_motors
        count = count+1;
    end
end

```

```

Vb = batteries(1,1);
Rs = batteries(1,2);
I0 = motors(j,1);
Rm = motors(j,2);
Kv = motors(j,3);
Icmax = motors(j,4);
W = motors(j,5);

[N,Vm,Im,T,eta_eng,eta_prop,T_to,E,eta_tot]...
    = compute_config(filename,I0,Rm,Kv,Vb,Rs,V,Vto,tf);

    results = [results;
N,Im,Icmax,T,T_to,eta_eng,eta_prop,eta_tot,E,W,Vm];
end

%%%filter and store the results
filtered_results = [];
names2 = cell(1);
count = 0;
for i=1:n_motors
    if(results(i,4)>5.5 && results(i,4)<7 && results(i,2)<results(i,3) ...
        && results(i,8)>0.25)% 5.5<T<7, Im<Icmax, eta_tot>0.25
        filtered_results = [filtered_results; results(i,:)];
        count = count +1;
        names2{count} = strcat(names{i,1},propname);
    end
end

if(numel(filtered_results)>0)
    data_cells=num2cell(filtered_results);
    output_matrix=[names2',data_cells];
    master_output_matrix = [master_output_matrix; output_matrix];
end

%%%store unfiltered(raw) results too
uf_results = [];
names3 = cell(1);
count = 0;
for i=1:n_motors
    uf_results = [uf_results; results(i,:)];
    count = count +1;
    names3{count} = strcat(names{i,1},propname);
end
data_cells=num2cell(uf_results);
output_matrix=[names3',data_cells];
master_output_matrix2 = [master_output_matrix2; output_matrix];
end

%%%write to xls
col_header={'motor','N [RPM]','Im [A]','Icmax [A]','T [N]','Tto
[N]','eta_eng',...
    'eta_prop','eta_tot','E [mAh]','W [g]','Vm [V]'};
master_output_matrix = [col_header;master_output_matrix];
Ofilename = 'Results.xlsx';
xlswrite(Ofilename,master_output_matrix);

```

```
master_output_matrix2 = [col_header;master_output_matrix2];  
Ofilename = 'Results_raw.xlsx';  
xlswrite(Ofilename, master_output_matrix2);  
  
Time_spent = toc
```



```

else %start storing data
    [tokens,matches] = regexp(tline,expression,'tokens','match');
    if(isempty(matches) == false)%found a useful table row
        intable = true;
        temp_row = [];
        for (i=1:1:8)
            temp_row = [temp_row,str2num(tokens{1}{i})];
        end
        temp_table = [temp_table; temp_row];
        num = tokens{1}{2};
    else
        if(intable == true)%found empty row after useful table
            intable = false;
            inarea = false;
            data_tables{table_count} = temp_table;
        end
    end
end
end
tline = fgetl(fid);
end
fclose(fid);

%%%%%%%%%for cruise
%%%%%%%%%Select only rpm tables that have the needed V__mph and get:
propdata = []; %matrix with columns: (rpms/1000), Ct, Cp, T_meas - for given
V
for (i=1:1:table_count)
    current_table = data_tables{i};
    %check if velocity is within range
    [rows,columns] = size(current_table);
    if(V__mph < current_table(rows,1) && V__mph > current_table(1,1))
        %this sheet is usable
        p = polyfit(current_table(:,1),current_table(:,4),3);
        Ct = polyval(p,V__mph);
        p = polyfit(current_table(:,1),current_table(:,5),3);
        Cp = polyval(p,V__mph);
        p = polyfit(current_table(:,1),current_table(:,8),3);
        T_meas = polyval(p,V__mph);
        rpm = str2num(char(array_of_rpms(i)))/1000;
        propdata = [propdata;[rpm,Ct,Cp,T_meas]];
    end
end

%%%%%%%%%Interpolate Ct, Cp, T_meas as functions of rpm for given V
rpms = propdata(:,1)*1000;
nr_rpms = numel(rpms);
p_Ct = polyfit(rpms,propdata(:,2),4);
p_Cp = polyfit(rpms,propdata(:,3),4);
p_T_meas = polyfit(rpms,propdata(:,4),4);
N_temp = rpms(1,1):100:rpms(nr_rpms,1); %RPM (temporary vector)
Ct = polyval(p_Ct,N_temp);
Cp = polyval(p_Cp,N_temp);
T_meas = polyval(p_T_meas,N_temp);

%%%%%%%%%Calculations for optimal configuration

```

```

%fprintf('%%%%%%%% For cruise velocity %%%%%%%%%\n');
Vm = (Vb*Rm+N_temp*Rs/Kv)/Rt; %temporary vector
Im = (Vb*(1-(Rm/Rt))-N_temp*Rs/(Kv*Rt))/Rs; %temporary vector
Pout = (Im-I0).*(Vb-Im*Rt); %temporary vector
Pp_in = Cp.*((N_temp/(60*gR)).^3)*rho*(D^5); %temporary vector
P_diff = abs(Pout-Pp_in); %temporary vector
[min_diff,loc] = min(P_diff(:)); %temporary vector
Ct1 = Ct(loc); %dimensionless thrust coefficient, function of J
Cp1 = Cp(loc); %dimensionless power coefficient, function of J
N = N_temp(loc); %motor rpm [RPM]
Vm1 = Vm(loc); %voltage at motor poles [V]
Im1 = Im(loc); %current through motor [A]
Pout1 = Pout(loc); %motor mechanical output power, prop input power
Pin = Im1.*Vm1; %input power to motor [W]
T = rho*(D^4)*(Ct1*N*N)/(3600*gR*gR); %thrust [N]
Qm = (Im1-I0)/Kt; %motor torque [Nm]
eta_eng = Pout1/Pin; %engine efficiency
eta_prop = T*V/Pout1; %propeller efficiency
eta_tot = eta_eng*eta_prop; %total/overall efficiency
E = (Im1*Vm1*tf/Vm1)*1000/3600; %energy used (mAh)

%%%%%%%%%%for takeoff
%%%%%%%%%Select only rpm tables that have the needed Vto_mph and get:
propdata = []; %matrix with columns: (rpms/1000), Ct, Cp, T_meas - for given
V
for (i=1:1:table_count)
    current_table = data_tables{i};
    %check if velocity is within range
    [rows,columns] = size(current_table);
    if(Vto_mph < current_table(rows,1) && Vto_mph > current_table(1,1))
        %this sheet is usable
        p = polyfit(current_table(:,1),current_table(:,4),3);
        Ct = polyval(p,Vto_mph);
        p = polyfit(current_table(:,1),current_table(:,5),3);
        Cp = polyval(p,Vto_mph);
        p = polyfit(current_table(:,1),current_table(:,8),3);
        T_meas = polyval(p,Vto_mph);
        rpm = str2num(char(array_of_rpms(i)))/1000;
        propdata = [propdata;[rpm,Ct,Cp,T_meas]];
    end
end

%%%%%%%%%Interpolate Ct, Cp, T_meas as functions of rpm for given V
rpms = propdata(:,1)*1000;
nr_rpms = numel(rpms);
p_Ct = polyfit(rpms,propdata(:,2),4);
p_Cp = polyfit(rpms,propdata(:,3),4);
p_T_meas = polyfit(rpms,propdata(:,4),4);
N_temp = rpms(1,1):100:rpms(nr_rpms,1); %RPM (temporary vector)
Ct = polyval(p_Ct,N_temp);
Cp = polyval(p_Cp,N_temp);
T_meas = polyval(p_T_meas,N_temp);

%%%%%%%%%Calculations for optimal configuration
%fprintf('%%%%%%%% For takeoff velocity %%%%%%%%%\n');
Vm = (Vb*Rm+N_temp*Rs/Kv)/Rt; %temporary vector

```

```

Im = (Vb*(1-(Rm/Rt))-N_temp*Rs/(Kv*Rt))/Rs; %temporary vector
Pout = (Im-I0).*(Vb-Im*Rt); %temporary vector
Pp_in = Cp.*((N_temp/(60*gR)).^3)*rho*(D^5); %temporary vector
P_diff = abs(Pout-Pp_in); %temporary vector
[min_diff,loc] = min(P_diff(:)); %temporary vector
Ct2 = Ct(loc); %dimensionless thrust coefficient, function of J
Cp2 = Cp(loc); %dimensionless power coefficient, function of J
N_to = N_temp(loc); %motor rpm [RPM]
Vm_to = Vm(loc); %voltage at motor poles [V]
Im_to = Im(loc); %current through motor [A]
Pout_to = Pout(loc); %motor mechanical output power, prop input power
Pin_to = Im_to.*Vm_to; %input power to motor [W]
T_to = rho*(D^4)*(Ct2*N_to*N_to)/(3600*gR*gR); %thrust [N]
Qm_to = (Im_to-I0)/Kt; %motor torque [Nm]
eta_eng_to = Pout_to/Pin_to; %engine efficiency
eta_prop_to = T_to*Vto/Pout_to; %propeller efficiency

```

Appendix B – Stability Analysis Formulae

All images in this Appendix come from Reference 8 (Napolitano).

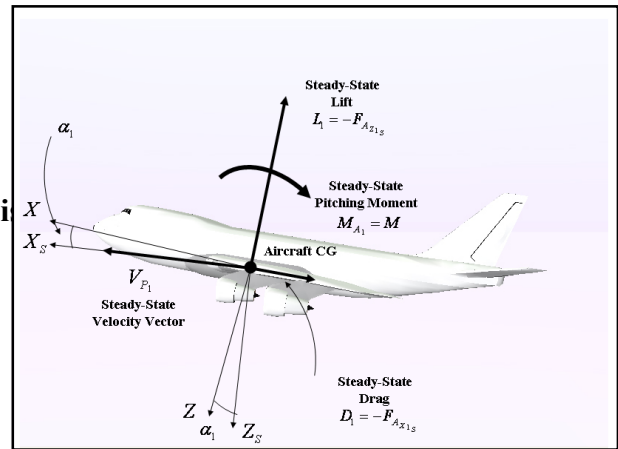
$$f_{A_x} = \bar{q} S \left\{ - \left[c_{D_u} + 2c_{D_1} \right] \left(\frac{u}{V_{P_1}} \right) + \left[-c_{D_\alpha} + c_{L_1} \right] \alpha - c_{D_{\dot{\alpha}}} \left(\frac{\dot{\alpha} \bar{c}}{2V_{P_1}} \right) - c_{D_q} \left(\frac{q \bar{c}}{2V_{P_1}} \right) - c_{D_{\delta_E}} \delta_E - c_{D_{i_H}} i_H \right\}$$

$$c_{D_1} = \frac{T_1}{\bar{q}_1 S} = c_{D_0} + c_{D_\alpha} \alpha_1 + c_{D_{\delta_E}} \delta_{E_1} + c_{D_{i_H}} i_{H_1}$$

$$c_{L_1} = \frac{W}{\bar{q}_1 S} \longleftarrow L_1 = c_{L_1} \bar{q} S = W$$

$$c_{D_0} = c_D \Big|_{\alpha=\delta_E=i_H=0^\circ} \longleftarrow \text{[5],[6] or wind tunnel analysis}$$

$$c_{D_\alpha} \longleftarrow \text{[5],[6] or wind tunnel analysis}$$



SPECIAL CASE : ‘uncambered’ aircraft (with parabolic ‘drag’ polar curve)

$$\bar{c}_{D_0} = c_{D_0}$$

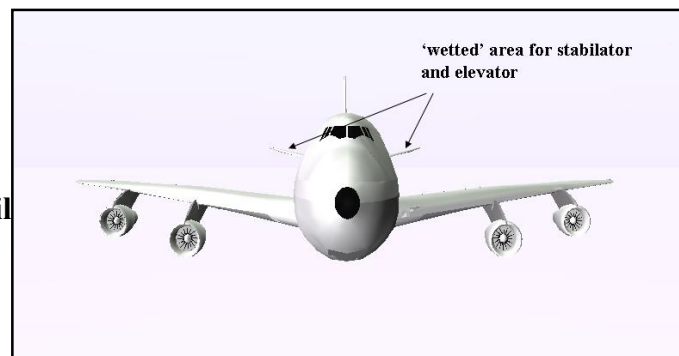
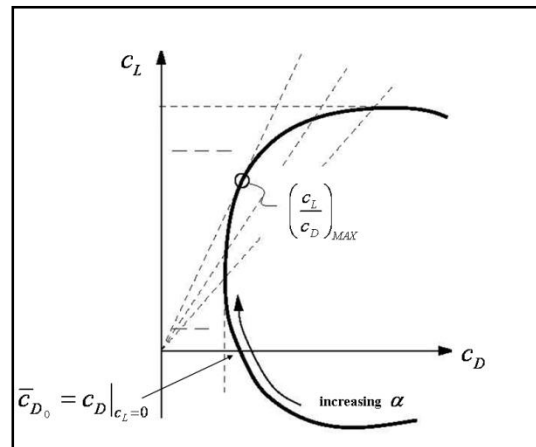
$$c_{D_\alpha} \approx \left(\frac{2c_{L_1}}{\pi AR e} \right) c_{L_\alpha}$$

$$c_{D_u} = Mach \cdot \frac{\partial c_D}{\partial Mach} \approx 0 \quad \text{at low subsonic}$$

$$c_{D_{\dot{\alpha}}} \approx 0$$

$$c_{D_q} \approx 0$$

$$\left. \begin{array}{l} c_{D_{\delta_E}} \approx 0 \\ c_{D_{i_H}} \approx 0 \end{array} \right\} \text{... except for large horizontal tail} \\ \text{Large dihedral/anedral angles}$$

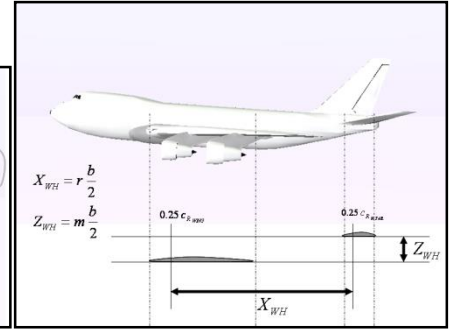
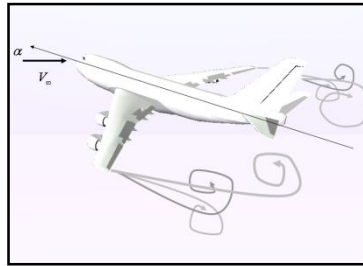


$$f_{A_z} = \bar{q} S \left\{ -[c_{L_u} + 2c_{L_1}] \left(\frac{u}{V_{P_1}} \right) + [-c_{L_\alpha} - c_{D_1}] \alpha - c_{L_{\dot{\alpha}}} \left(\frac{\dot{\alpha} \bar{c}}{2V_{P_1}} \right) - c_{L_q} \left(\frac{q \bar{c}}{2V_{P_1}} \right) - c_{L_{\delta_E}} \delta_E - c_{L_{i_H}} i_H \right\}$$

$$c_{L_1} = \frac{W}{\bar{q}_1 S} \longleftarrow L_1 = c_{L_1} \bar{q} S = W$$

$$c_{D_1} = \frac{T_1}{\bar{q}_1 S} = c_{D_0} + c_{D_\alpha} \alpha_1 + c_{D_{\delta_E}} \delta_{E_1} + c_{D_{i_H}} i_{H_1}$$

$$c_{L_\alpha} = c_{L_{\alpha_{WB}}} + c_{L_{\alpha_H}} \eta_H \frac{S_H}{S} \left(1 - \frac{d\varepsilon}{d\alpha} \right)$$



$$\left(\frac{d\varepsilon}{d\alpha} \right)_{Mach} = 4.44 \left(K_{AR} K_\lambda K_{mr} \sqrt{\cos(\Lambda_{0.25})} \right)^{1.19} \sqrt{1 - Mach^2}$$

“Downwash” effect
(Chapter II)

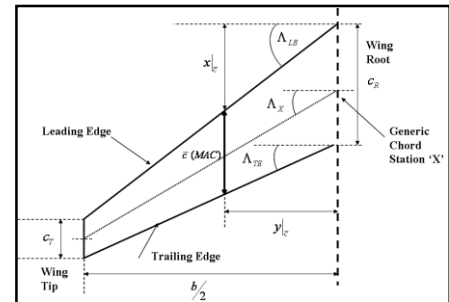
Polhamus
formula
(Chapter II)

$$c_{L_\alpha} = \frac{2\pi AR}{2 + \sqrt{\left[\frac{AR^2 (1 - Mach^2)}{k^2} \left(1 + \frac{\tan^2(\Lambda_{0.5})}{(1 - Mach^2)} \right) \right] + 4}}$$

$$c_{L_u} = \left(\frac{Mach^2}{1 - Mach^2} \right) \cdot c_{L_1}$$

$$c_{L_{\dot{\alpha}}} \approx c_{L_{\dot{\alpha}_W}} + c_{L_{\dot{\alpha}_H}}$$

$$c_{L_{\dot{\alpha}_H}} \approx 2c_{L_{\alpha_H}} \eta_H \frac{S_H}{S} (\bar{x}_{AC_H} - \bar{x}_{CG}) \frac{d\varepsilon}{d\alpha}$$



$$c_{L_q} \approx c_{L_{qW}} + c_{L_{qH}} \quad c_{L_{qW}} \Big|_{Mach=0} = \left(\frac{1}{2} + 2 \cdot |\bar{x}_{AC_W} - \bar{x}_{CG}| \right) c_{L_{\alpha_W}} \Big|_{Mach=0}$$

$$c_{L_{qW}} = \left[\frac{AR + 2 \cos \Lambda_{c/4}}{AR \cdot B + 2 \cos \Lambda_{c/4}} \right] \cdot c_{L_{qW}} \Big|_{Mach=0} \approx 0$$

$$B = \sqrt{1 - Mach^2 (\cos \Lambda_{c/4})^2}$$

$$c_{L_{qH}} \approx 2c_{L_{\alpha_H}} \eta_H \frac{S_H}{S} (\bar{x}_{AC_H} - \bar{x}_{CG})$$

$$c_{L_{i_H}} = \eta_H \frac{S_H}{S} c_{L_{\alpha_H}}$$

$$c_{L_{\delta_E}} = \eta_H \frac{S_H}{S} c_{L_{\alpha_H}} \tau_E = c_{L_{i_H}} \tau_E$$

$$m_A = \bar{q} S \bar{c} \left\{ \left[c_{m_u} + 2c_{m_1} \right] \left(\frac{u}{V_{P_1}} \right) + c_{m_\alpha} \alpha + c_{m_{\dot{\alpha}}} \left(\frac{\dot{\alpha} \bar{c}}{2V_{P_1}} \right) + c_{m_q} \left(\frac{q \bar{c}}{2V_{P_1}} \right) + c_{m_{\delta_E}} \delta_E + c_{m_{i_H}} i_H \right\}$$

$c_{m_1} = 0$ at steady-state trimmed conditions

$$c_{m_u} = -c_{L_1} \frac{\partial \bar{x}_{AC_W}}{\partial Mach}$$

$$c_{m_\alpha} = c_{L_{\alpha_W}} (\bar{x}_{AC_{WB}} - \bar{x}_{CG}) - c_{L_{\alpha_H}} \eta_H \frac{S_H}{S} \left(1 - \frac{d\varepsilon}{d\alpha} \right) (\bar{x}_{AC_H} - \bar{x}_{CG})$$

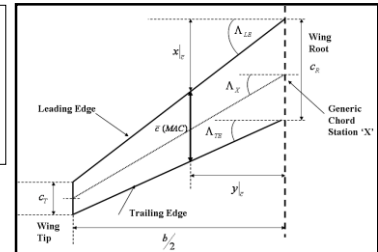


“Downwash” effect
(Chapter II)

$$\left(\frac{d\varepsilon}{d\alpha} \right)_{Mach} = 4.44 \left(K_{AR} K_\lambda K_{mr} \sqrt{\cos(\Lambda_{0.25})} \right)^{1.19} \sqrt{1 - Mach^2}$$

Polhamus
formula
(Chapter II)

$$c_{L_\alpha} = \frac{2\pi AR}{2 + \sqrt{\left[\frac{AR^2 (1 - Mach^2)}{k^2} \left(1 + \frac{\tan^2(\Lambda_{0.5})}{(1 - Mach^2)} \right) \right] + 4}}$$



$$c_{m_{\dot{\alpha}}} \approx c_{m_{\alpha_H}}$$

$$c_{m_{\alpha_H}} \approx -c_{L_{\alpha_H}} (\bar{x}_{AC_H} - \bar{x}_{CG}) \approx -2c_{L_{\alpha_H}} \eta_H \frac{S_H}{S} (\bar{x}_{AC_H} - \bar{x}_{CG})^2 \frac{d\varepsilon}{d\alpha}$$

$$c_{m_q} \approx c_{m_{qW}} + c_{m_{qH}}$$

$$c_{m_{qW}} = \left[\frac{\left(\frac{AR^3 \tan^2 \Lambda_{c/4}}{AR \cdot B + 6 \cos \Lambda_{c/4}} \right) + \frac{3}{B}}{\left(\frac{AR^3 \tan^2 \Lambda_{c/4}}{AR + 6 \cos \Lambda_{c/4}} \right) + 3} \right] \cdot c_{m_{qW}} \Big|_{Mach=0} \approx 0$$

$$c_{m_{qW}} \Big|_{Mach=0} = -K_q c_{L_{\alpha W}} \Big|_{Mach=0} \cos \Lambda_{c/4} \cdot C$$

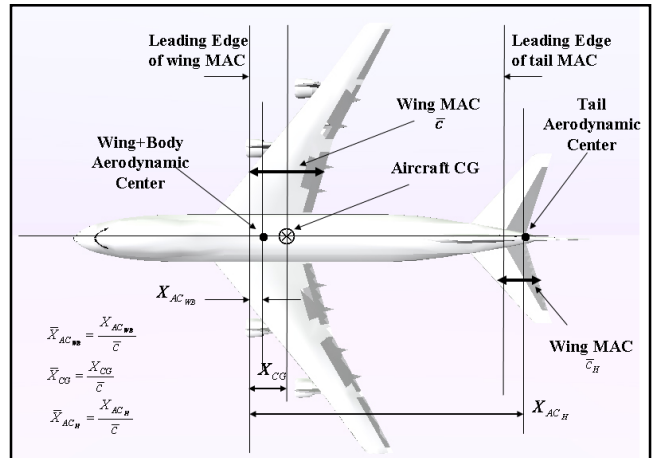
$$C = \frac{AR \left(0.5 |\bar{x}_{AC_W} - \bar{x}_{CG}| + 2 |\bar{x}_{AC_W} - \bar{x}_{CG}|^2 \right)}{AR + 2 \cos \Lambda_{c/4}} + \frac{1}{24} \left(\frac{AR^3 \tan^2 \Lambda_{c/4}}{AR + 6 \cos \Lambda_{c/4}} \right) + \frac{1}{8}$$

$$c_{m_{qH}} \approx -2c_{L_{\alpha_H}} \eta_H \frac{S_H}{S} (\bar{x}_{AC_H} - \bar{x}_{CG})^2$$

$$c_{m_{i_H}} = -c_{L_{\alpha_H}} \eta_H \frac{S_H}{S} (\bar{x}_{AC_H} - \bar{x}_{CG})$$

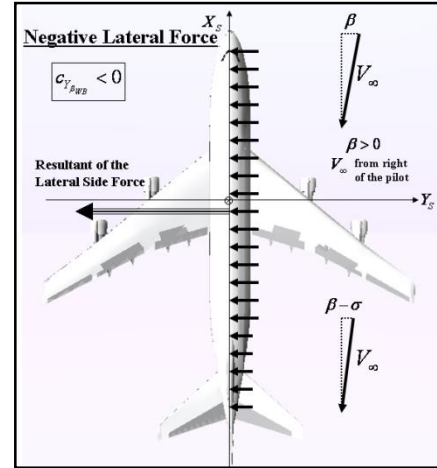
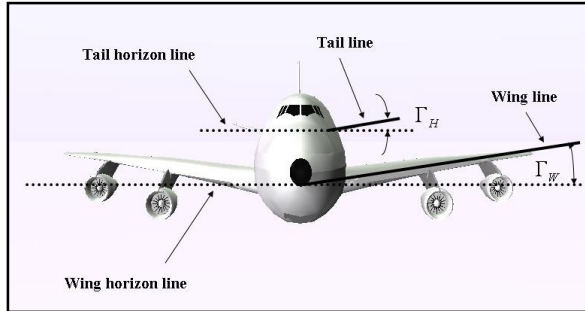
$$c_{m_{\delta_E}} = -c_{L_{\alpha_H}} \eta_H \frac{S_H}{S} (\bar{x}_{AC_H} - \bar{x}_{CG}) \tau_E =$$

$$= c_{m_{i_H}} \tau_E$$



$$f_{A_y} = \bar{q} S \left\{ c_{Y_\beta} \beta + c_{Y_{\dot{\beta}}} \left(\frac{\dot{\beta} b}{2V_{P_1}} \right) + c_{Y_p} \left(\frac{p b}{2V_{P_1}} \right) + c_{Y_r} \left(\frac{r b}{2V_{P_1}} \right) + c_{Y_{\delta_A}} \delta_A + c_{Y_{\delta_R}} \delta_R \right\}$$

$$c_{Y\beta} = (c_{Y\beta_W} + c_{Y\beta_B}) + c_{Y\beta_H} + c_{Y\beta_V}$$



$$c_{Y\beta_W} \approx -0.0001 |\Gamma_W| \cdot 57.3$$

$$c_{Y\beta_B} \approx -2 \cdot K_{\text{int}} \cdot \frac{S_{P \rightarrow V}}{S}$$

$$c_{Y\beta_H} \approx -0.0001 |\Gamma_H| \cdot 57.3 \cdot \eta_H \cdot \left(1 - \frac{d\sigma}{d\beta} \right) \frac{S_H}{S}$$

$$\eta_H \cdot \left(1 - \frac{d\sigma}{d\beta} \right) = 0.724 + 3.06 \frac{S_H/S}{1 + \cos(\Lambda_{c/4})} + 0.4 \frac{Z_W}{d} + 0.009 \cdot AR$$

$$c_{Y\beta_V} \approx -k_{Y_V} \cdot |c_{L_{\alpha_V}}| \eta_V \cdot \left(1 - \frac{d\sigma}{d\beta} \right) \frac{S_V}{S}$$

$$\eta_V \cdot \left(1 - \frac{d\sigma}{d\beta} \right) = 0.724 + 3.06 \frac{S_V/S}{1 + \cos(\Lambda_{c/4})} + 0.4 \frac{Z_W}{d} + 0.009 \cdot AR$$

Polhamus formula with

$$c_{Y_{\dot{\beta}}} \approx 0$$

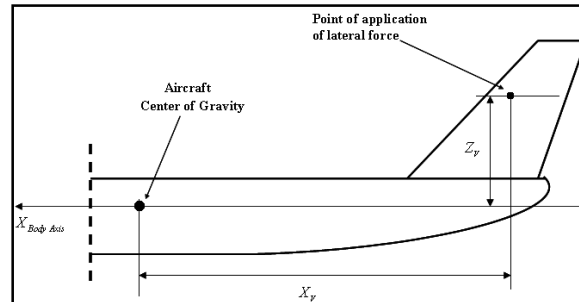
$$AR_{V_{\text{eff}}} = c_1 \cdot AR_V \cdot [1 + K_H (c_2 - 1)]$$

$$c_{Y_p} \approx c_{Y_{pV}} = 2 c_{Y_{\beta V}} \frac{(Z_V \cos \alpha_1 - X_V \sin \alpha_1)}{b}$$

$$c_{Y_r} \approx c_{Y_{rV}} = -2 c_{Y_{\beta V}} \frac{(X_V \cos \alpha_1 + Z_V \sin \alpha_1)}{b}$$

$$c_{Y_{\delta_A}} \approx 0$$

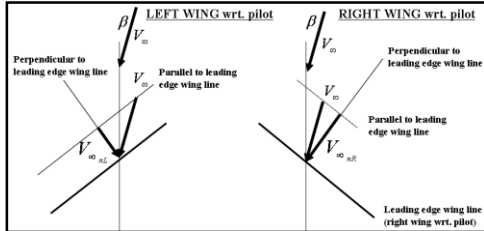
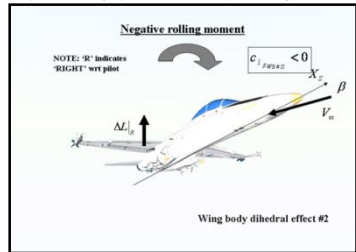
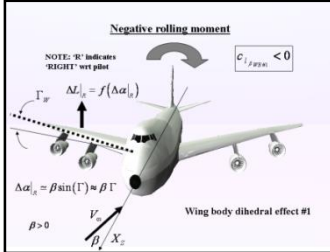
$$c_{Y_{\delta_R}} = |c_{L_{\alpha_V}}| \eta_V \frac{S_V}{S} K_R \tau_R$$



$$l_A = \bar{q} S b \left\{ c_{l_\beta} \beta + c_{l_{\dot{\beta}}} \left(\frac{\dot{\beta} b}{2V_{P_1}} \right) + c_{l_p} \left(\frac{p b}{2V_{P_1}} \right) + c_{l_r} \left(\frac{r b}{2V_{P_1}} \right) + c_{l_{\delta_A}} \delta_A + c_{l_{\delta_R}} \delta_R \right\}$$

$$c_{l_\beta} = c_{l_{\beta_{WB}}} + c_{l_{\beta_H}} + c_{l_{\beta_V}}$$

$$c_{l_{\beta_{WB}}} \approx c_{l_{\beta_{WB}}} \left| \begin{array}{l} \text{Dihedral Effect \#1} \\ \text{(due to } \Gamma \text{ angle)} \end{array} \right. + c_{l_{\beta_{WB}}} \left| \begin{array}{l} \text{Dihedral Effect \#2} \\ \text{(due to High/Low Wing)} \end{array} \right. + c_{l_{\beta_{WB}}} \left| \begin{array}{l} \text{Dihedral Effect \#3} \\ \text{(due to Sweep Angle } \Lambda_{LE}) \end{array} \right.$$



$$c_{l_{\beta_{WB}}} = c_{L_1} \left[\left(\frac{c_{l_\beta}}{c_{L_1}} \right)_{N_c/2} K_{M_A} K_f + \left(\frac{c_{l_\beta}}{c_{L_1}} \right)_{AR} \right] + \Gamma_W \left[\frac{c_{l_\beta}}{\Gamma_W} K_{M_\Gamma} + \frac{\Delta c_{l_\beta}}{\Gamma_W} \right]$$

$$+ \left(\Delta c_{l_\beta} \right)_{Z_W} + \varepsilon_W \tan \Lambda_{c/4} \left(\frac{\Delta c_{l_\beta}}{\varepsilon_W \tan \Lambda_{c/4}} \right)$$

$$c_{l_{\beta_H}} = c_{l_{\beta_{WB}}}|_H \eta_H \left(1 - \frac{d\sigma}{d\beta} \right) \frac{S_H}{S} \frac{b_H}{b} \approx 0$$

$$c_{l_{\beta_V}} = -k_{X_V} \cdot |c_{L_{\alpha_V}}| \eta_V \cdot \left(1 - \frac{d\sigma}{d\beta} \right) \frac{S_V}{S} \cdot \frac{(Z_V \cos \alpha_1 - X_V \sin \alpha_1)}{b}$$

$$c_{l_{\dot{\beta}}} \approx 0$$

$$c_{l_p} = c_{l_{p_{WB}}} + c_{l_{p_H}} + c_{l_{p_V}}$$

$$c_{l_{p_{WB}}} \approx c_{l_{p_W}} = RDP \cdot \frac{k}{\beta}, \quad c_{l_{p_H}} \approx \frac{1}{2} \left(c_{l_{p_W}} \right)_H \frac{S_H}{S} \left(\frac{b_H}{b} \right)^2, \quad c_{l_{p_V}} \approx 2 c_{Y_{\beta_V}} \left(\frac{Z_V}{b} \right)^2$$

$$c_{l_r} = c_{l_{r_W}} + c_{l_{r_V}}$$

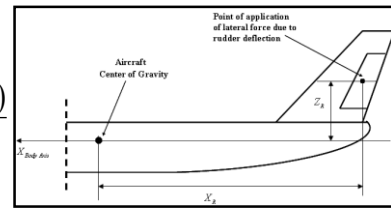
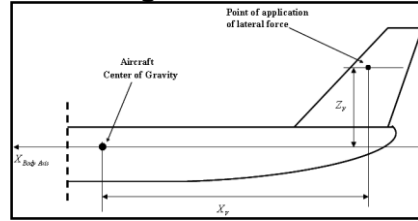
$$c_{l_{r_W}} \approx \left(\frac{c_{l_r}}{c_{L_1}} \right)_{Mach} \cdot c_{L_1} + \left(\frac{\Delta c_{l_r}}{\Gamma} \right) \cdot \Gamma + \left(\frac{\Delta c_{l_r}}{\varepsilon_W} \right) \cdot \varepsilon_W \quad (rad^{-1})$$

$$c_{l_{r_V}} \approx -2 \cdot c_{Y_{\beta_V}} \cdot \frac{(X_V \cos \alpha_1 + Z_V \sin \alpha_1)}{b} \cdot \frac{(Z_V \cos \alpha_1 - X_V \sin \alpha_1)}{b}$$

$$c_{l_{\delta_A}} = \left(c_{l_{\delta}} \right)_{Left} + \left(c_{l_{\delta}} \right)_{Right}$$

$$c_l = \left[\left(\frac{c_{l_{\delta}}}{2} \right)_{Left} + \left(\frac{c_{l_{\delta}}}{2} \right)_{Right} \right] \cdot 2 \cdot \delta_A \leftarrow c_{l_{\delta}} = \tau_A \cdot c_{l_{\delta}}' \leftarrow c_{l_{\delta}}' = \frac{RME \cdot k}{\beta}$$

$$c_{l_{\delta_R}} = c_{Y_{\delta_R}} \left(\frac{Z_R \cos \alpha_1 - X_R \sin \alpha_1}{b} \right) = |c_{L_{\alpha_V}}| \eta_V \frac{S_V}{S} K_R \tau_R \left(\frac{Z_R \cos \alpha_1 - X_R \sin \alpha_1}{b} \right)$$



$$n_A = \bar{q} S b \left\{ c_{n\beta} \beta + c_{n\dot{\beta}} \left(\frac{\dot{\beta} b}{2V_{P_1}} \right) + c_{n_p} \left(\frac{p b}{2V_{P_1}} \right) + c_{n_r} \left(\frac{r b}{2V_{P_1}} \right) + c_{n\delta_A} \delta_A + c_{n\delta_R} \delta_R \right\}$$

$$c_{n\beta} = c_{n\beta_W} + c_{n\beta_B} + c_{n\beta_H} + c_{n\beta_V}$$

$$c_{n\beta_B} = -57.3 K_N K_{R_1} \frac{S_{B_S} l_B}{S b}$$

$$c_{n\beta_H} \approx 0$$

$$c_{n\beta_V} \approx 0$$

$$c_{n\beta_V} = k_{Y_V} \cdot |c_{L_{\alpha_V}}| \eta_V \cdot \left(1 - \frac{d\sigma}{d\beta} \right) \frac{S_V}{S} \cdot \frac{(X_V \cos \alpha_1 + Z_V \sin \alpha_1)}{b}$$

$$c_{n\dot{\beta}} \approx 0$$

$$c_{n_p} = c_{n_{p_W}} + c_{n_{p_V}}$$

$$c_{n_{p_W}} \approx \left(\frac{c_{n_p}}{c_{L_1}} \right) \Big|_{\substack{\text{Mach} \\ C_L=0}} c_{L_1} + \left(\frac{\Delta c_{n_p}}{\varepsilon_W} \right) \varepsilon_W$$

$$c_{n_{p_V}} \approx -2 \cdot c_{Y_{\beta_V}} \cdot \frac{(X_V \cos \alpha_1 + Z_V \sin \alpha_1)}{b} \cdot \frac{(Z_V \cos \alpha_1 - X_V \sin \alpha_1 - Z_V)}{b}$$

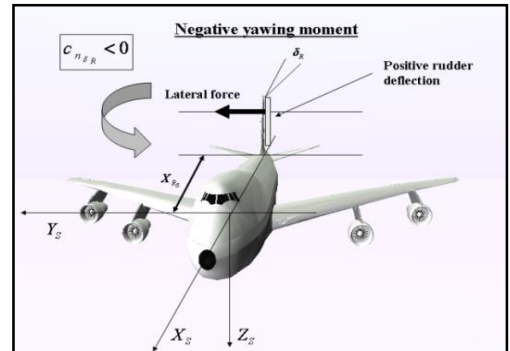
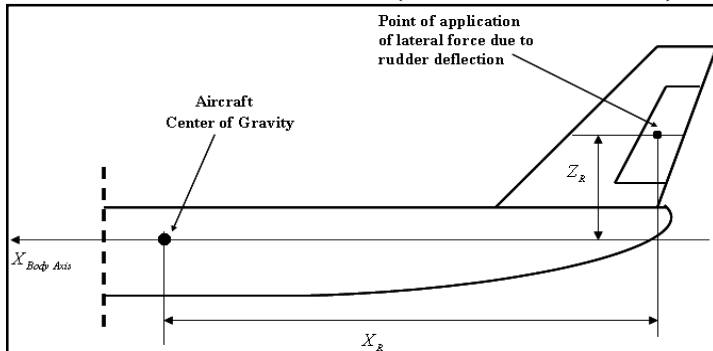
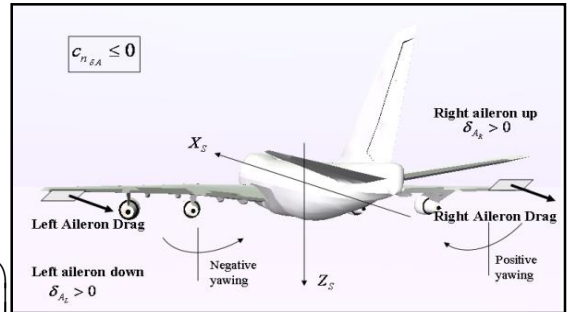
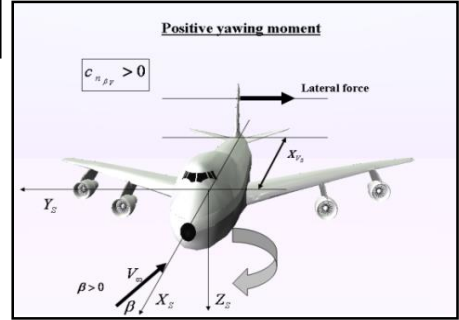
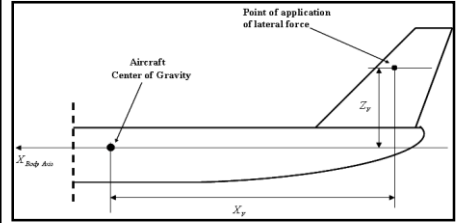
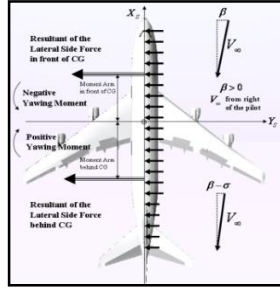
$$c_{n_r} \approx c_{n_{r_W}} + c_{n_{r_V}}$$

$$c_{n_{r_W}} \approx \left(\frac{c_{n_r}}{c_{L_1}} \right) \cdot c_{L_1}^2 + \left(\frac{c_{n_r}}{\bar{c}_{D_0}} \right) \cdot \bar{c}_{D_0}$$

$$c_{n_{r_V}} \approx 2 \cdot c_{Y_{\beta_V}} \cdot \frac{(X_V \cos \alpha_1 + Z_V \sin \alpha_1)^2}{b^2}$$

$$c_{n\delta_A} = K_{n_A} c_{L_1} c_{l_{\delta_A}}$$

$$c_{n\delta_R} = -|c_{L_{\alpha_V}}| \eta_V \frac{S_V}{S} K_R \tau_R \left(\frac{X_R \cos \alpha_1 + Z_R \sin \alpha_1}{b} \right)$$



Appendix C – Stability Analysis Script

```
%Major Qualifying Project
%Micro Air Vehicle Team 2 - 2014

%% Stability Derivatives, Static Stability, Dynamic Stability

% This Document is intended for educations purposes. It details numerical
methods to approximate an aircraft's
% Stability Derivatives using the methods described in Aircraft Dynamics
% and from Modeling to Simulations by Marcello R. Napolitano as well as
% sources like the United States Air Force Stability and Control Digital
% DATCOM. It also uses State Variable Modeling for both the Longitudinal
% Dynamics and Lateral Dynamics of the aircraft.

clc; clear all; close all;
%%Physical Variables
g = 32.178; %Gravity in Ft/sec^2
rho = 1.23; %kg/m^3
a = 1116.44; %Speed of sound in ft/s

% %% Flight Conditions, Mass and Inertial Data for Zero Payload Flight
% Vp1 = 13; %ft/sec
% xCG_root = 9.094; %distance from CG to wing root in inches, input from
Solidworks
% m = 2.79; %Mass (lbs)
% Ixxb = 11.92*0.0310809502; %Moment of Inertia x-axis (slug ft^2)
% Iyyb = 8.23*0.0310809502; %Moment of Inertia y-axis (slug ft^2)
% Izzb = 20.12*0.0310809502; %Moment of Inertia z-axis (slug ft^2)
% Ixzb = 0.13*0.0310809502; %Product of Inertia xz-plane (slug ft^2)

% %% Flight Conditions, Mass and Inertial Data for Minimal Payload (2 plates)
% Vp1 = 15; %ft/sec
% xCG_root = 6.8688; %distance from CG to wing root in inches, input from
Solidworks
% m = 3.88; %Mass (lbs)
% Ixxb = 11.96*0.0310809502; %Moment of Inertia x-axis (slug ft^2)
% Iyyb = 9.20*0.0310809502; %Moment of Inertia y-axis (slug ft^2)
% Izzb = 21.06*0.0310809502; %Moment of Inertia z-axis (slug ft^2)
% Ixzb = 0.29*0.0310809502; %Product of Inertia xz-plane (slug ft^2)

% %% Flight Conditions, Mass and Inertial Data for Half Payload (8 plates)
Vp1 = 19.9; %ft/sec
xCG_root = 4.4588; %distance from CG to wing root in inches, input from
Solidworks
m = 6.84; %Mass (lbs)
Ixxb = 12.03*0.0310809502; %Moment of Inertia x-axis (slug ft^2)
Iyyb = 11.44*0.0310809502; %Moment of Inertia y-axis (slug ft^2)
Izzb = 23.24*0.0310809502; %Moment of Inertia z-axis (slug ft^2)
Ixzb = 0.64*0.0310809502; %Product of Inertia xz-plane (slug ft^2)

% %% Flight Conditions, Mass and Inertial Data for Full Payload (16 plates)
% Vp1 = 25; %ft/sec
```

```

% xCG_root = 4.4588; %distance from CG to wing root in inches, input from
Solidworks
% m = 10.68; %Mass (lbs)
% Ixxb = 12.53*0.0310809502; %Moment of Inertia x-axis (slug ft^2)
% Iyyb = 24.20*0.0310809502; %Moment of Inertia y-axis (slug ft^2)
% Izzb = 12.19*0.0310809502; %Moment of Inertia z-axis (slug ft^2)
% Ixzb = 0*0.0310809502; %Product of Inertia xz-plane (slug ft^2)

%% Geometric Inputs
%Given Geometric Parameters of the wing
ct = .75; % Length of the Tip Chord (ft)
cr = 1.25; % Length of the Root Chord (ft)
DeltaLE = 0.022; % Leading Edge Sweep Angle (rad)
XwhR = 5.276; % Distance between the tip of the leading edge of the wing and
the tip of the leading edge of the tail (ft)
Zwh = 0.1574; % Vertical distance between the bottom of the tail and the
bottom of the wing (ft)
b = 10.5; %total wing span in ft
S = 11.3796; %Wing area in ft^2
%Given Geometric Parameters of the Horizontal Tail
bh = 3.0208; % Span of the tail (ft)
cth = .6667; % Length of the Tip Chord of the tail (ft)
crh = .6667; % Length of the Root Chord of the tail (ft)
DeltaLEh = 0; % Tail Leading Edge sweep angle
%Given Geometric Parameters of the Vertical Tail
b2v = 1.5208; %ft Double the height of the vertical tail
ctv = .6667; %ft Length of the tip chord of the vertical tail
crv = .6667; %ft length of the root chord of the vertical tail
deltalev = 0; %rad Leading edge sweep angle of the vertical tail
%wing tail geometric parameters
Xvs = 4.6823; %ft, distance from CG to c/4 of vertical tail
Zvs = .3732; %ft
Xrs = 4.6823; %ft
Zrs = 0.3732; %ft % Xrs and Zrs are relative to the rudder. To determine the
value of these parameters, you can look at the Napolitano TextBook. (pg. 160,
168)
%Other geometric Inputs. For our aircraft there is no rudder. We assumed
%values to be 0.
d = .1; %ft This is the fuselage diameter
%% Other General Inputs for Which Numerical Calculations are not Necessary.
BTheta = 0; %Pitch Angle
Alpha1 = 4/57.3; %Steady-State Angle of Attack (rad)
CD0 = 0.1
CDalpha = 0.01;
CTxu = 0;
CL0 = 1.2175
CM0 = -0.2244
CMtu = 0;
CMtalpha = 0;
CDde = 0;
CDih = 0;
CNTbeta = 0;
CL1 = 1.3;
CD1 = 0.093;
CM1 = 0;
CTx1 = 0;
CMt1 = 0;

```

```

%The following stability derivatives were calculated through approximation
%methods provided in the UNITED STATES AIR FORCE DATCOM.
CYds = 0;
CLds = 0.022;
CNds = 0.004;

%% Geometric and General Calculations
q_bar = 0.5*rho*((Vp1*0.3048)^2)*0.02089; %dynamic pressure in lbf/ft^2
M = Vp1/a; %Mach number
%Wing Geometric Parameters;
Lambda = .754; %Taper Ratio, for a regular tapered wing is simply ct/cr
AR = b^2/S; %Aspect Ratio
MAC = ((2/3)*cr)*((1+Lambda+Lambda^2)/(1+Lambda)); %Mean Aerodynamic Chord
(cbar) (ft)
%Xmac = (b/6)*((1+2*Lambda)/(1+Lambda))*tan(DeltaLE); %Distance between mean
aerodynamic chord and the leading edge of the wing (ft)
Xmac = 0.035;%ft
sweepangleathalf = atan(tan(DeltaLE)-(4*(1/2)*(1-Lambda)/(AR*(1+Lambda))));
%Sweep Angle at half of the leading edge of the wing(rad)
sweepangleatquarter = atan(tan(DeltaLE)-(4*(1/4)*(1-
Lambda)/(AR*(1+Lambda))));%Sweep Angle at a quarter of the leading edge of
wing(rad)
%Horizontal Tail Geometric Parameters
Lambdah = cth/crh; % Tail Taper Ratio
Sh = (bh/2)*crh*(1+Lambdah); %Area of the Horizontal Tail (ft^2)
ARh = bh^2/Sh; %Aspect Ratio of the tail
Cbarh = ((2/3)*crh)*((1+Lambdah+Lambdah^2)/(1+Lambdah)); %Mean Aerodynamic
Chord (ft) of the tail
Xmach = (bh/6)*((1+2*Lambdah)/(1+Lambdah))*tan(DeltaLEh); %Distance between
mean aerodynamic chord and the leading edge of the tail (ft)
sweepanglehalfoftail = atan(tan(DeltaLEh)-(4*(1/2)*(1-
Lambdah)/(ARh*(1+Lambdah)))); %Sweep Angle at half of the leading edge of
tail (rad)
sweepangleatquarteroftail = atan(tan(DeltaLEh)-(4*(1/4)*(1-
Lambdah)/(ARh*(1+Lambdah))));%Sweep Angle at a quarter of the leading edge of
tail(rad)
%Calculation of vertical tail geometric parameters
lambdav = ctv/crv;
s2v = (b2v/2)*crv*(1+lambdav);%note that s2v is twice the value of the area
of the vertical tail.
ARv = b2v^2/s2v;
cbarv = (2/3)*crv*(1+lambdav +lambdav^2)/(1+lambdav);
xmacv = (b2v/6)*((1+2*lambdav)/(1+lambdav))*tan(deltalev);
ymacv = (b2v/6)*((1+2*lambdav)/(1+lambdav));
sweepangleofverticaltailathalf = atan(tan(deltalev)-((4*0.5*(1-
lambdav)/(ARv*(1+lambdav))));

%Wing-Tail Geometric Calculations and Parameters
Xwh = XwhR +(crh/4)-(cr/4); %Distance between the quarter chord point of the
wing and the quarter chord point of the horizontal tail
Xach = XwhR + Xmach + (Cbarh/4) - Xmac; % This is the distance between the
Mean Aerodynamic Chord of the Wing and the Mean Aerodynamic Chord of the tail
Xach = 5.13;
% knowing Xwh and the given Zwh we can now calculate the wing-tail
% geometric parameters that will be needed for the analysis of the downwash

```

```

% effect
r = 2*Xwh/b;
m = 2*Zwh/b;
% if the aspect ratio of the wing is less than 4 use the following equation
% to calculate k (k being the wing-lift slope coefficient for our equation
% of lift
%K = 1 + (AR*(1.87 - 0.000233*DeltaLE)/100)
%If the Aspect Ratio of the wing is greater than or equal to 4 use the
%following equation.
K = 1 + ((8.2-2.3*DeltaLE)-AR*(0.22-0.153*DeltaLE))/100;

%Center of gravity
XCG = (xCG_root-(Xmac*12))/(MAC*12); %the center of gravity, normalized

%Inputs to help with Calculation of Aerodynamic Center
%K1 = 1.13; %changes with Lambda
%K2 = 0.1; %changes with Lambda, DeltaLE
xprimeac = .3; %this value was calculated using figure 2.27 on Napolitano
book and its already divided by cr.
%%Note the values above are calculated by interpolating functions and
%%looking the numbers up on a graph since they vary with speed and leading
%%edge sweep angles. Pages 54-55 of the Napolitano text book.
%XACw = K1*(xprimeac - K2);
XACw = 0.25;
XACb = 0; %Aerodynamic Center Shift due to Body.
XAch = Xach/MAC; % No equation to calculate this value is given.
XACwb = XACw + XACb;

%Inputs of Surface Effectiveness
%Now we want to calculate the lift stability derivative with respect to the
%elevator deflection
tauE = .4; %for 22% c_elevator/c_HT (page 52)
%tauE is the effectiveness of the elevator as functions for the Mean
%aerodynamic chord of the elevator divided by the mean aerodynamic chord of
%the horizontal tail. (See See Aircraft Dynamics and Control by Napolitano
%pg. 85).
%Horizontal Tail Efficiency
Hte = .9;
%vertical tail efficiency.
nv = 0.95;
%% Inputs to Help with the Calculations for the Lateral Components of Static
Stability
%vertical tail lift slope coefficient
%calculating ARveff
%find c1 using lambdav and figure 4.15 on page 144 in Napolitano TextBook and
bv/2r1 (Where r1 is the distance
%between the bottom of the vertical tail and the bottom of the fuselage.
c1= 1.1; %using the above
%find c2 using the figure 4.16 on book.
Xachv = Xmach + (0.25*Cbarh);
%can now use xachv and divided it by cbarv to find c2 using the table 4.16
%also use Zh/bv where if Zh is above cg its considered negative. (Zh is the
%distance between the horizontail tail and vertical tail).
c2 = 1.25;
%finally we can use Sh/Sv and table 4.18 to find the value of Khv
%remember that Sv needs to be half of s2v.

```

```

Khv = 1.25;
%wing contribution due to the geometric dihedral angle
%using lambda and sweepanglehalf in degrees and figure 4.43 on page we can
find x1 =
%clb/gammaw
gammaw = 0; %for this particular aircraft we have an anhedral.
x1 = -0.000175; %(1/deg^2)
Zw = -.125; %this is the vertical distance from the wing root (at the 25%
station) and the fuselage centerline.Fig 4.45 It will be negative
%if it is above the fusela centerline.(ft)
%using the table 4.44
Kmt = 1.0;
%using the given lambda and the Aspect ration and the sweepanglehalf (in
%degrees)using figure 4.39 to find (clb/cl1) at the sweepangle at half.
x3 = -0.001; %(1/deg)
m1 = M*cos(sweepanglehalf);
m2 = AR/(cos(sweepanglehalf));
%using the previously calculated m1 and m2 we use figure 4.40 to find Kma
kma = 1.0;
A = 1.125; %ft the length between the tip of the fuselage to the half point
of the wing.
x4 = A/b;
%using x4 and m2 we can use figure 4.41 to find kf
kf = 0.98;
%Wing contribution to the dihedral effect due to wing twist angle.
%assuming a twist angle of ew = 2 deg = 0.0345 rad and using lambda and
%aspect ration we can use figure 4.46 to find
%deltaclb/ew*tan(sweepangleatquarterchord) or X, which helps find clbwb5.
ew = 0;
% Now we need to find the contribution of the vertical tail.
%using the equation bv/2r1 and figure 4.13 we can find out kyv values.
kyv = 1;
alpha1 = 0.0698; % this is the steady state angle of attack in rad
%Now the contribution of the body.
Spv = 1.8; %ft^2, now this value is the location of the fuselage where the
flow transitions from potential to viscous. Talk to Professor Linn.
%using the value from using Zw/D/2 and the table on figure 4.8 we get Kint.
Kint = 0.410;
%To find the body contribution, we will need to use various parameters.
%Including Lcg, lb, L^2b Sbs, Zmax and Wmax. These parameters can be found
%in figure 4.67 of book page 172, also use figure 4.68 and 4.69 to find Kn
%and Krei
lcg = .81;
lb = 6;
Sbs = .533;
z1 = .2605;
z2 = .041667;
zmax = .2667;
wmax = .2;
Kn = 0.001;
% well will have to find the reynolds number for the fueselage using page.
% 221.
Krel = 1;
%Wing contribution due to the wing-fuselage position
fuselageaverageheight = 0.1667; %ft
fuselageaveragewidth = 0.1667; %ft
%% Defining Geometry for Rudder

```

```

Yri = 0;
Yrf = 0.79; % Ft
Ni = Yri/(.5*b2v);
Nf = Yrf/(.5*b2v);
%Using the variables found above and the lambdav, we use figure 4.27
Kri = 0;
Krf = 1;
%Using the Cbarrudder and Cbarverticaltail which are lengths specified on p
%148, the length from the back of the rudder to the front of the rudder and
%the length from the back of rudder to the front of the tail
Cbarrudder = 0;
Cbarverticaltail = 0;
%use the variables above and figure 4.26 to find rudder efficiency
tauR = 1;
%% Defining Geometry for Ailerons
%Now we calculate the contribution of the ailerons to the rolling moments.
Yai = 0; %the lengths of the ailerons (inner) Measured from center of
fuselage to inner tip of aileron
Yao = 0; %the lengths of the ailerons (outer)Measure from center of fuselage
to outer tip of aileron
Nia = Yai/(b/2);
Noa = Yao/(b/2);
beta = sqrt(1-M^2);
deltabeta = atan(tan(sweepangleatquarter)/beta)*(180/pi);%Degrees
%Now using the values found above, and our lambda we can use figure 4.51,
%Nia and Noa to find out RMEi and RMEo
RMEi = 0;
RMEo = 0;
cbaraileron = 0; %Thickness of the aileron
cbarwingataileron = 0; %Thickness of wing with aileron
%using figure 4.55 we can find the aileron effectiveness
tauA = 0;
%Now to find the contribution of the ailerons to the yawing moments.
%Use Nia and Noa along with lambda and figure 4.73 to find our KNa value.
Knai = 0;
Knao = 0;
DKNA = 0;
%Now the calculation of CLp
%First the calculation of CLpw.
deltabeta;
Lambda;
%Using the above parameters, we go to figure 4.80 and 4.81 to find RDP
RDP = -0.15;
%Now to find the contribution of the horizontal tail using the following
%parameters.
beta;
deltabetaH = atan(tan(sweepangleatquarteroftail)/beta)*(180/pi);
%Using the parameters found above and lambdah and figures 4.80 and 4.81 we
%can get our RDPH
RDPH = -0.11;
%Now we can use the lambda and AR and figure 4.83 to find the (CNp/EW)
%values, we will call D5
D5 = 0.0001;
%Now we can use our lambda, AR, sweep angle at the quarterchord in degrees
%and figure 4.85 and we will find our clr/cll at mach 0 value, which we
%will call L6.
L6 = 0.29;

```

```

%Using lambda and AR, we can use figure 4.87 to find our CLR/EW or L9
L9 = .016;%(1/rad*deg)
%Using figure 4.89, our lambda, AR, sweepangleatquarter, and XAC-XCG we
%will find out (Cnr/Cl1) which we will call W
W = -0.0181; %(1/rad) (Talk to Linn)
%% Defining Geometry for the Spoilers

%% Calculation of the Longitudinal Stability Derivatives
CLaw = (2*pi*AR)/(2+sqrt((AR^2*(1-M^2)/K^2)*(1+(tan(sweepangleathalf)^2/(1-
M^2))))+4));
%% Modeling the Downwash Effect
%The downwash effect is considered to be an aerodynamic longitudinal
interference generated by
%the wing on the horizontal tail due to a system of vorticies created by
%the wing itself.
Kar = 1/AR - 1/(1+(AR)^1.7); %using the aspect ration and values for the wing
Klambda = (10-(3*Lambda))/7;
Kmr = (1-(m/2))/r^0.33;
%now the downwash effect function
%first comes the detaepsilon/deltaalpha equation at a mach of 0.
downwash = ((Kar*Klambda*Kmr*sqrt(cos(sweepangleatquarter)))^1.19)*4.44;
%Now to calculate the actual value of the downwash effect on the stability
%derivate we need to take the lift coeffient of the wing at zero mach
%number and divide this by a given traveling mach number and multiply it by
%the detaepsilon/deltaalpha equation or downwash. Note for our airplane the
%totaldownwash may simlby be the downwash since our traveling speed will be
%assumed to be mach 0.
Clalphaw0 = (2*pi*AR)/(2+sqrt((AR^2*(1-
0)/K^2)*(1+(tan(sweepangleathalf)^2/(1-0))))+4));
totaldownwasheffect = downwash*(CLaw/Clalphaw0);

%% Longitudinal Stability Derivatives
%Now we use the values we have from the horizontal tail to attain the
%horizontal life - slope.
% for this section we use the samel nomenclature that we use when find the
% k values for the wing. if AR is less than 4 use this, if greate than 4
% use the second. For this wing, ARh is less than 4
Kh = 1 + ((8.2-2.3*DeltaLEh)-ARh*(0.22-0.153*DeltaLEh))/100;
CLah = (2*pi*ARh)/(2+sqrt((ARh^2*(1-
M^2)/Kh^2)*(1+(tan(sweepangleathalfoftail)^2/(1-M^2))))+4));
%CLAlphawb = Clalphaw*(1 + (0.025*(d/b))-(0.25*(d/b)^2)); To be used only
%if indicated by professors. Typical approximation in subsonic flight is
%claw = clawb
%% Longitudinal Stability Derivatives (CL)
CLalpha = CLaw + CLah*1*(Sh/S)*(1-totaldownwasheffect)
%1 is the tail efficiency
%% Calculation of the Longitudinal Stability Derivative CL with respect to
the elevator
CLde = 1*(Sh/S)*CLah*tauE
%% Calculation of the Longitudinal Stability Derivative CL with respect to
the Stabilator
CLih = 1*(Sh/S)*CLah
%% Total Lift stability derivative which include the control derivatvies
%Cl1 = Missing Component (lift coefficient evaluated at the initial cond).
%+ CLa*alpha + CLse*tauE + CLih*ih; The missing component is the value of
%CL associated with alpha = 0. Use the CL vs Alpha graph of the airfoil.

```

```

%% Longitudinal Stability Derivatives (CM)
%% %CMa is the pitching moment stability derivative with respect to the angle
of attack.
CMalpha = CLaw*(XCG-XACwb)- CLah*1*(Sh/S)*(1-totaldownwasheffect)*(XACH-XCG)
%% %CMse is the pitching moment stability derivative with respect to the
elevator deflection
CMde = -CLah*1*(Sh/S)*(XACH-XCG)*tauE
%% CMih is the pitching moment stability derivative with respect to the
stabilator deflection
CMih = -CLah*1*(Sh/S)*(XACH-XCG)
%% Total Aerodynamic Center
%The total aerodynamic center of the aircraft can be evaluated using the
%following equations, which includes the aerodynamic center of the wing,
%tail, downwash effect, tail efficiency, and the lift stability derivatives
%with respect to the angle of attack for both the horizontal tail and the
%wing
XAC = (XACwb + (CLah/CLaw)*1*(Sh/S)*(1-totaldownwasheffect)*XACH)/(1 +
(CLah/CLaw)*1*(Sh/S)*(1-totaldownwasheffect))
%% Longitudinal Stability Derivatives (CD1, CL1, CM1)
%These are steady state terms. They depend
%of the specific steady-state conditions for aircraft while CM1 = 0. By
%definition the trim conditions.
%% Modeling (CDu CLu CMu)
%associated with the small perturbations in the forward speed.
%CDu, models the increase in drag for small increments in forward speed.
%This is negligible at low subsonic speed.
CDu = 0
%CLu, models the increase in lift for small increments in the forward
%speed. This is negligible at low subsonic speeds.
CLu = 0
%CMu, models the change in pitching moment for small increments in the
%forward speed. This is negligible for us.
CMu = 0
%% Modeling of CDadot, CLadot, CMadot and CDq, CLq, CMq.
%Describe aerodynamics effects that deal with the rate of change in the angle
of
%attack and pitch rate q.
%However, the drag coefficients CDadot and CDq are always negligible.
CLalphadot = 2*CLah*1*(Sh/S)*(XACH-XCG)*totaldownwasheffect
COE = sqrt(1-M^2*cos(sweepangleatquarter)^2);
var1 = AR + 2*cos(sweepangleatquarter);
var2 = AR*COE+2*cos(sweepangleatquarter);
var3 = (.5+2*abs(XACw-XCG))*Clalphaw0;
CLqw = (var1/var2)*var3;
CLqh = 2*CLah*1*(Sh/S)*(XACH-XCG);
CLq = CLqw+CLqh
CMalphadot = -2*CLah*1*(Sh/S)*(XACH-XCG)^2*totaldownwasheffect
CMq = -2*CLah*1*(Sh/S)*(XACH-XCG)^2

%% Lateral Stability Derivatives
AREff = c1*ARv*(1+Khv*(c2-1));
% since our value for AREff is less than 4, we apply the polhamus formula
% for AR,4.
Kv = 1 +(AREff*(1.87 - 0.000233*deltalev)/100);
%% Modeling CL alpha with respect to the vertical tail

```

```

CLav = (2*pi*AREff)/(2+sqrt((AREff^2*(1-
M^2)/Kv^2)*(1+(tan(sweepangleofverticaltailathalf)^2/(1-M^2))+4));
%% Modeling CLb which is the Steady State Rolling Moment with respect to the
wing and body
clbwb1 = 57.3*gammaw*(x1*Kmt);%(1/rad)
Sfavg = pi*(fuselageaverageheight/2)*(fuselageaveragewidth/2); %average cross
sectional area of the fuselage
db = sqrt(Sfavg/0.7854); %ft, the fuselage diameter
clbwb3 = 57.3*CL1*(x3*kma*kf);%(1/rad)
clbwb2 = 57.3*(1.2*sqrt(AR)/57.3)*(Zw/b)*(2*db/b); %for either a high wing or
low wing configuration. (1/rad)
%using our lambda and aspect ratio, we can use figure 4.42 to find x*,
%which will be a function of (clb/cl1)AR which is -0.00094
clbwb4 = 57.3*CL1*-0.00094;
% %Wing contribution to the dheadrla effect due to wing twish angle.
clbwb5 = 57.3*ew*tan(sweepangleatquarter)*(-3.2*10^-5);
%Wing contribution to the dihedral effect
x5 = -0.0005*AR*(db/b)^2;
clbwb6 = 57.3*gammaw*x5;
%% total clbwb (Steady State Rolling Moment from the Wing and Body
clbwb = clbwb1+clbwb2+clbwb3+clbwb4+clbwb5+clbwb6; %(1/rad)
%% Horizontal Tail Contribution to the Steady State Rolling Moment
%Because the aircraft does not have a significant dihedral or anhedral
%angles, the horizontal tail contribution will be 0.
clbh = 0;
%% Vertical Tail Contribution to the Steady State Rolling Moment
% Now to find the f = nv*(1+dsigma/dbeta), the vertical tail efficienct times
the sidewash angle.
f = 0.724 + 3.06*(.5*s2v/S)/(1 +
cos(sweepangleatquarter))+0.4*(Zw/db)+0.009*AR;
clbv = -kyv*abs(CLav)*f*((.5*s2v)/S)*((Zvs*cos(alpha1)-Xvs*sin(alpha1))/b);
%% Now we find the total clb or steady state rolling moments due to the
sideslip angle.
CLbeta = clbwb + clbv + clbh %(1/rad)
%% now we move into the calculation of the Cyb or the steady state lateral
forces due to the sideslip angle.
%% Contribution of the Wing to the Steady State Lateral Forces Due to
Sideslip Angle
%Cybw = -0.0001*abs(gammaw)*57.3 where gammaw is the dihedral angle. Needs to
be
%positive. For this aircraft gammaw is less than zero, so cybw will be 0.
Cybw = -0.0001*abs(0)*57.3
%% Contribution of the body to the Steady State Lateral Forces Due to
Sideslip
Cybb = -2*Kint*(Spv/S); % rad^-1
%% Contribution of the vertical tail to the Steady State Lateral Forces Due
to Sideslip
Cybv = -kyv*CLav*f*(s2v/S);% rad^-1
%% Steady State Lateral Forces Stability Derivative
CYbeta = Cybw+Cybb+Cybv % rad^-1
%% Contribution to the yawing moments due to sideslip angle from the wings
Cnbw = 0;
%% Contribution to the yawing moments due to sideslip angle from the body
Cnbb = -57.3*Kn*Krel*(Sbs/S)*(lb/b);
%% Contribution to the yawing moments due to sideslip angle from the vertical
tail
Cnbv = -Cybv*(Xvs*cos(alpha1)+Zvs*(sin(alpha1)))/b; %rad^-1

```

```

%% Yawing Moments Stability Derivative due to Sideslip Angle
CNbeta = Cnbb+Cnbv+Cnbw %rad^-1

%% Contribution of the ailerons to the steady state lateral forces
CYda = 0; %this is zero because the forces associated with asymmetric
deflections of ailerons act along the vertical and horizontal directions.
Negligible in lateral direction
%% Contribution of the Rudder to the Steady State lateral Forces
DKR = Krf - Kri;
CYdr = abs(CLav)*.88*(.5*s2v/S)*DKR*tauR
%% Contribution of the rudder to yawing moments.
CNdr = -CYdr*((Xrs*cos(alpha1))+Zrs*sin(alpha1))/b %rad^-1
%% Contribution of the ailerons to the rolling moments.
KA = CLaw*beta/(2*pi);
KA1 = (beta*AR)/(KA);
DRME = RMEo-RMEi;
cldprime = DRME*KA/beta;
cld = tauA*cldprime;
CLda = 0.5*(cld+cld) %Rad^-1
%% Contribution of the rudder to the rolling moments.
CLdr = CYdr*(Zrs*cos(alpha1)-Xrs*sin(alpha1))/b % (1/rad)
%% Contribution of the Ailerons to Yawing Moments
CNda = DKNA*CL1*CLda
%Clarification on this part of the analysis.
%% Now we will find the derivatives due to small perturbations on the lateral
section.
%% CYp
CYp = 2*Cybv*(Zvs*cos(alpha1)-Xvs*sin(alpha1))/b % (1/rad)
%% CLp
CLpw = RDP*(KA/beta); %Contribution of the wing
beta;
KAh = CLah*beta/(2*pi);
KA1h=(beta*ARh)/KAh;
CLph = RDP*(KAh/beta); %Contribution of the Horizontal Tail
CLpv = 2*Cybv*(Zvs/b)^2; %Contribution of the Vertical Tail
CLp = CLpw+CLph+CLpv
%% CNp
B = sqrt(1-M^2*cos(sweepangleatquarter)^2);
C =
(AR+4*cos(sweepangleatquarter))/(AR*B+4*cos(sweepangleatquarter))* (AR*B+(.5*(
(AR*B)+4*cos(sweepangleatquarter)))*tan(sweepangleatquarter)^2)...
/(AR+(.5*(AR+4*cos(sweepangleatquarter)))*tan(sweepangleatquarter)^2);
%now we will need (Cnp/CL1)at a mach number where CL = 0. We are callings
%this equation, D
D1 = (AR+6*(AR+cos(sweepangleatquarter)));
D2 = ((XCG-
XAC)*(tan(sweepangleatquarter)/AR))+(tan(sweepangleatquarter)^2/12);
D3 = (AR+cos(sweepangleatquarter));
D = ((D1*D2)/D3)*(-1/6);
D4 = C*D;
CNpw = D4*CL1+D5*ew; %Terrible Representation of the number, not a very
accurate value.
CNpv = -2*Cybv*((Xvs*cos(alpha1))+Zvs*sin(alpha1))/b)*(((Zvs*cos(alpha1))-
Xvs*sin(alpha1)-Zvs)/b);

```

```

CNp = CNpw + CNpv %Total Value for CNp
%% CYr
CYr = 2*Cybv*(Xvs*cos(alpha1)+Zvs*sin(alpha1))/b % (1/rad)
%% CLr
L1 = sqrt(1-M^2*cos(sweepangleatquarter)^2);
L2 = (AR*(1-L1^2))/(2*L1*(AR*L1+2*cos(sweepangleatquarter)));
L3 = (AR*L1+2*cos(sweepangleatquarter))/(AR*L1+4*cos(sweepangleatquarter));
L4 = (tan(sweepangleatquarter)^2)/8;
L5 = (AR+2*cos(sweepangleatquarter))/(AR+4*cos(sweepangleatquarter));
L = (1+L2+L3*L4)/(1+L5*L4);
L7 = L6*L;
L8 =
(1/12)*(pi*AR*sin(sweepangleatquarter))/(AR+4*cos(sweepangleatquarter));%(r
ad^-2)
CLrw = L7*CL1+L8*(gammaw*(pi/180))+L9*2; %rad^-1 %Wing Contribution
CLrv = -2*Cybv*((Xvs*cos(alpha1)-Zvs*sin(alpha1))/b)*((Zvs*cos(alpha1)-
Xvs*sin(alpha1))/b); % (1/rad) %Vertical Tail Contribution
CLr = CLrw+CLrv % (1/rad)
%% CNr
CNrw = W*(CL1)^2; %Wing Contribution
CNrv = 2*Cybv*(Xvs*cos(alpha1)+Zvs*sin(alpha1))^2/b^2; %Vertical Tail
Contribution
CNr = CNrw+CNrv %Total
%% Longitudinal Dimensional Stability Derivatives
Xu = (((-q_bar*S)*(CDu+2*CD1))/(m*Vp1))*g; % (1/sec)
Xalpha = (((-q_bar*S)*(CDalpha-CL1))/(m))*g; % (ft*sec^2)
Zu = (((-q_bar*S)*(CLu+2*CL1))/(m*Vp1))*g; % (1/sec)
Zalphadot = (((-q_bar*S*MAC*CLalphadot))/(2*m*Vp1))*g; % (ft*sec^-1)
Mu = (((q_bar*S*MAC)*(CMu+2*CM1))/(m*Iyyb)); % (ft^-1*sec^-1)
Malpha = (((q_bar*S*MAC)*(CMalpha))/(Iyyb)); % (sec^-2)
Malphadot = (((q_bar*S*MAC*CMalphadot)/(Iyyb))*(MAC/(2*Vp1))); % (sec^-1)
Xtu = (((q_bar*S)*(CTxu+2*CTx1))/(m*Vp1))*g; % (sec^-1)
Zalpha = (((-q_bar*S)*(CLalpha+CD1))/m)*g; % (ft*sec^-2)
Zq = (((-q_bar*S*MAC*CLq))/(2*m*Vp1))*g; % (ft*sec^-1)
MTu = (((q_bar*S*MAC)*(CMtu+2*CMt1))/(Iyyb*Vp1)); % (ft^-1*sec^-1)
MTalpha = (((q_bar*S*MAC)*(CMtalpha))/(Iyyb)); % (sec^-2)
Mq = ((q_bar*S*MAC*CMq)/(Iyyb))*(MAC/(2*Vp1)); % (sec^-1)
%% Longitudinal Dimensional Control Derivatives
Zde = (((-q_bar*S*CLde)/m)*g; % (ft*sec^-2)
Mde = ((q_bar*S*MAC*CMde)/Iyyb); % (sec^-2)
Xde = (((-q_bar*S*CDde)/m)*g; % (ft*sec^-2)
Zih = (((-q_bar*S*CLih)/m)*g; % (ft*sec^-2)
Mih = ((q_bar*S*MAC*CMih)/Iyyb); % (sec^-2)
Xih = (((-q_bar*S*CDih)/m)*g; % (ft*sec^-2)
%% Lateral Dimensional Stability Derivatives
Ybeta = ((q_bar*S*CYbeta)/m)*g; % (ft*Sec^-2)
Yr = ((q_bar*b*S*CYr)/(2*m*Vp1))*g; % (ft*sec^-1)
Yp = ((q_bar*b*S*CYp)/(2*m*Vp1))*g; % (ft*sec^-2)
Lbeta = (q_bar*S*(b)*CLbeta)/Ixxb; % (sec^-2)
Lp = (q_bar*S*(b^2)*CLp)/(Ixxb*Vp1^2); % (sec^-1)
Lr = (q_bar*S*(b^2)*CLr)/(Ixxb*Vp1^2); % (sec^-1)
Nbeta = (q_bar*S*b*CNbeta)/(Izzb); % (sec^-2)
NTbeta = (q_bar*S*b*CNTbeta)/(Izzb); % (sec^-2)
Np = (q_bar*S*(b^2)*CNp)/(2*Izzb*Vp1); % (Sec^-1)
Nr = (q_bar*S*(b^2)*CNr)/(2*Izzb*Vp1); % (sec^-1)
%% Lateral Dimensional Control Derivatives
Yda = ((q_bar*S*CYda)/m)*g; % (ft*sec^-2)

```

```

Ydr = ((q_bar*S*CYdr)/m)*g; %(ft*sec^-2)
Yds = ((q_bar*S*CYds)/m)*g; %(ft*sec^-2)
Lda = ((q_bar*S*CLda*b)/Ixxb);%(sec^-2)
Ldr = ((q_bar*S*CLdr*b)/Ixxb);%(sec^-2)
Lds = ((q_bar*S*CLds*b)/Ixxb);%(sec^-2)
Nda = ((q_bar*S*CNda*b)/Izzb);%(sec^-2)
Ndr = ((q_bar*S*CNdr*b)/Izzb);%(sec^-2)
Nds = ((q_bar*S*CNds*b)/Izzb);%(sec^-2)
%% Primed Longitudinal Dimensional Stability Derivatives
%% Alpha-Dot Coefficients
z_u_prime = (Zu/(Vp1-Zalphadot));
z_alpha_prime = (Zalpha/(Vp1-Zalphadot));
z_q_prime = (Zq+Vp1)/(Vp1-Zalphadot);
z_theta_prime = -(g*sin(BTheta))/(Vp1-Zalphadot);
z_de_prime = Zde/(Vp1-Zalphadot);
z_ih_prime = Zih/(Vp1-Zalphadot);
%% U-dot Coefficients
x_u_prime = (Xu+Xtu);
x_alpha_prime = Xalpha;
x_theta_prime = -g*cos(BTheta);
x_q_prime = 0;
x_de_prime = Xde;
x_ih_prime = Xih;
%% Q-dot Coefficients
m_u_prime = (Malphadot*z_u_prime)+Mu;
m_alpha_prime = (Malphadot*z_alpha_prime)+Malpha;
m_theta_prime = Malphadot*z_theta_prime;
m_q_prime = (Malphadot*z_q_prime)+Mq;
m_de_prime = (Malphadot*z_de_prime)+Mde;
m_ih_prime = (Malphadot*z_ih_prime)+Mih;
%% Double Primed Longitudinal Dimensional Stability Derivatives
z_u_doubleprime = z_u_prime*Vp1;
z_alpha_doubleprime = z_alpha_prime*Vp1-g*sin(BTheta);
z_q_doubleprime = (z_q_prime-1)*Vp1;
z_theta_doubleprime = (z_theta_prime*Vp1)+g*sin(BTheta);
z_de_doubleprime = (z_de_prime*Vp1);
z_ih_doubleprime = (z_ih_prime*Vp1);
%% Setting up Matrices for State Variable Analysis
A_long = [z_alpha_prime z_u_prime z_q_prime z_theta_prime
          x_alpha_prime x_u_prime x_q_prime x_theta_prime
          m_alpha_prime m_u_prime m_q_prime m_theta_prime
          0 0 1 0];

B_long = [z_de_prime z_ih_prime
          x_de_prime x_ih_prime
          m_de_prime m_ih_prime
          0 0];

C_long = [z_alpha_doubleprime z_u_doubleprime z_q_doubleprime z_theta_prime
          1 0 0 0
          0 1 0 0
          0 0 1 0
          0 0 0 1];

D_long = [z_de_doubleprime z_ih_doubleprime
          0 0
          0 0
          0 0
          0 0];

```

```

%% Longitudinal Dynamic Stability Response to a Generic Longitudinal Maneuver
sys = ss(A_long, B_long, C_long, D_long);
t = [0:0.01:120];
size_t=max(size(t));
for i = 1:size_t;
    de(i,1) = 0;
    ih(i,1) = 0;
end
for i = 200:300;
    de(i) = -2/57.3;
end
for i = 2200:2300;
    de(i) = 2/57.3;
end
u = [de,ih];
y=lsim(sys,u,t);
az=y(:,1)*(1/32.2)+1;
alpha=y(:,2)*57.3;
U=y(:,3);
q=y(:,4)*57.3;
theta=y(:,5)*57.3;
ih=ih*57.3;
de=de*57.3;

figure(1);
plot(t,az,'b');
grid on;
xlabel ('Time (sec)');
ylabel ('Longitudinal Vertical Acceleration (g)');

figure(2);
plot(t,alpha,'b');
grid on;
xlabel ('Time (sec)');
ylabel ('Longitudinal Angle of Attack (deg)');

figure(3);
plot(t,U,'b');
grid on;
xlabel ('Time (sec)');
ylabel ('Linear Longitudinal Velocity (x-axis) (ft/sec)');

figure(4);
plot(t,q,'b');
grid on;
xlabel ('Time (sec)');
ylabel ('Pitch Angular Rate (y-axis) (deg/sec)');

figure(5);
plot(t,theta,'b');
grid on;
xlabel ('Time (sec)');
ylabel ('Euler Pitch Angle (deg)');

```

```

figure(6);
plot(t, (de), 'b');
grid on;
xlabel ('Time (sec)');
ylabel ('Elevator Deflection (deg)');
%% Primed Lateral Dimensional Stability Derivatives
I1 = Ixzb/Ixxb;
I2 = Ixzb/Izzb;
%% R-Dot Coefficients
n_beta_prime = (I2*Lbeta+Nbeta)/(1-I1*I2);
n_p_prime = (I2*Lp+Np)/(1-I1*I2);
n_r_prime = (I2*Lr+Nr)/(1-I1*I2);
n_da_prime = (I2*Lda+Nda)/(1-I1*I2);
n_dr_prime = (I2*Ldr+Ndr)/(1-I1*I2);
n_ds_prime = (I2*Lds+Nds)/(1-I1*I2);
n_phi_prime = 0;
%% P-Dot Coefficients
l_beta_prime = (Lbeta+(I1*Nbeta))/(1-I1*I2);
l_p_prime = (Lp+(I1*Np))/(1-I1*I2);
l_r_prime = (Lr+(I1*Nr))/(1-I1*I2);
l_da_prime = (Lda+(I1*Nda))/(1-I1*I2);
l_dr_prime = (Ldr+(I1*Ndr))/(1-I1*I2);
l_ds_prime = (Lds+(I1*Nds))/(1-I1*I2);
l_phi_prime = 0;
%% Beta-Dot Coefficients
y_beta_prime = (Ybeta/Vp1);
y_p_prime = (Yp/Vp1);
y_r_prime = (Yr-Vp1)/(Vp1);
y_phi_prime = (g*cos(BTheta))/Vp1;
y_da_prime = (Yda/Vp1);
y_dr_prime = (Ydr/Vp1);
y_ds_prime = (Yds/Vp1);
%% Double Primed Lateral Dimensional Stability Derivatives
%% a_y coefficients
y_beta_doubleprime = y_beta_prime*Vp1;
y_p_doubleprime = y_p_prime*Vp1;
y_r_doubleprime = Vp1*(y_r_prime+1);
y_phi_doubleprime = (y_phi_prime*Vp1)-g*cos(BTheta);
y_da_doubleprime = y_da_prime*Vp1;
y_dr_doubleprime = y_dr_prime*Vp1;
y_ds_doubleprime = y_ds_prime*Vp1;
%% Setting Up Matrices for State Variable Analysis
A_lat = [y_beta_prime y_p_prime y_r_prime y_phi_prime
         l_beta_prime l_p_prime l_r_prime 0
         n_beta_prime n_p_prime n_r_prime 0
         0 1 tan(BTheta) 0];
B_lat = [y_da_prime y_dr_prime y_ds_prime
         l_da_prime l_dr_prime l_ds_prime
         n_da_prime n_dr_prime n_ds_prime
         0 0 0];
C_lat = [y_beta_doubleprime y_p_doubleprime y_r_doubleprime y_phi_doubleprime
         1 0 0 0
         0 1 0 0
         0 0 1 0
         0 0 0 1];
D_lat = [y_da_doubleprime y_dr_doubleprime y_ds_doubleprime
         0 0 0

```

```

    0 0 0
    0 0 0
    0 0 0];

sys = ss(A_lat, B_lat, C_lat, D_lat);
t = [0:0.01:120];
size_t = max(size(t));
for i=1:size_t;
    dr(i,1)=0;
    da(i,1)=0;
    ds(i,1)=0;
end;
for i=200:300;
    dr(i,1) = 2/57.3;
    ds(i,1)= 10/57.3;
end;
for i = 2200:2300;
    dr(i,1)= -2/57.3;
    ds(i,1) =-10.7/57.3;
end;
u=[da,dr,ds];
y=lsim(sys,u,t);
ay = y(:,1)*(1/g);
beta = y(:,2)*57.3;
p = y(:,3)*57.3;
r =y(:,4)*57.3;
phi = y(:,5)*57.3;
ds = ds*57.3;
dr = dr*57.3;

figure(7);
plot(t, ay, 'b');
grid on;
xlabel ('Time (sec)');
ylabel ('Lateral Acceleration (g)');

figure(8);
plot(t, beta, 'b');
grid on;
xlabel ('Time (sec)');
ylabel ('Lateral Angle of Attack (deg)');

figure(9);
plot(t, p, 'b');
grid on;
xlabel ('Time (sec)');
ylabel ('Roll Angular Rate (x-axis) (deg/sec)');

figure(10);
plot(t, r, 'b');
grid on;
xlabel ('Time (sec)');
ylabel ('Yaw Angular Rate (y-axis) (deg/sec)');

figure(11);
plot(t, phi, 'b');

```

```
grid on;
xlabel ('Time (sec)');
ylabel ('Euler Roll Angle (deg)');

figure(12);
plot(t, ds, 'b');
grid on;
xlabel ('Time (sec)');
ylabel ('Deflection of Spoilers(deg)');

figure(13);
plot(t, dr, 'b');
grid on;
xlabel ('Time (sec)');
ylabel ('Deflection of Rudder(deg)');
```

Appendix D – Flight Test Snapshots



